POLITECNICO DI MILANO

Facoltà di Ingegneria dei Processi Industriali

Dipartimento di Energia

Application of the spatially resolved sampling technique to the analysis and optimal design of a CH_4-CPO reformer with honeycomb catalyst

Supervisors: **prof. Alessandra BERETTA**
prof. Gianpiero GROPPI

Co-examiners: **ing. Dario LIVIO**
ing. Alessandro DONAZZI
prof. Pio FORZATTI

Master ThesisTesi of:

Michela MARTINELLI

Matr. 740467

Academic year 2010-2011

LIST OF CONTENENTS

ABSTRACT

The catalytic partial oxidation (CPO) of CH_4 is one of the most attractive technologies for the production of syngas or hydrogen in small-medium scale applications. CPO can be carried out at millisecond contact times, under autothermal conditions to yield high selectivities to syngas. These features allow for the design of simple and compact reactors, with fast dynamic response and low heat capacity, which are ideal for mobile and stationary production of synthesis gas. Despite of these advantages, CPO reactors operate under extremely high gradients of temperature and of composition and with complex fluid and kinetic patterns, where mass and heat transfer are coupled with the surface process. The CPO process mainly occurs with as a sequence of exothermic and endothermic steps, wherein the hydrocarbon is both oxidized to CO_2 and H_2O, either partially or completely, and also converted to synthesis gas by endothermic steam reforming. Hot spot temperature establish at the entrance of the reactor. The high surface temperatures can cause a local loss of activity of the catalyst producing a dangerous autocatalytic increase of the temperature, ultimately leading to the instable performance of the whole reactor. The experience suggests that surface temperatures below 1000 °C are needed for preventing catalyst deactivation.

Because of the presence of these gradients, concentrated at the inlet of the reactor, the behaviour of the system could not be fully described by the unique analysis of the gas composition at the exit of the reactor. The spatially resolved sampling technique was herein applied to investigate the process. This technique allows to "look" directly inside the reactor through the measurement of axial temperature and composition profiles while the reactor is maintained under adiabatic conditions. For the measurements of temperature of the gas and solid phase, a thermocouple and an optical fiber connected to a pyrometer were used for gas and solid phase, respectively. For the composition profiles the gas was probed from the reactor by a capillary connected to a micro-pump and delivered to the micro-gas chromatograph through a pump. The experimental data obtained with the spatially resolved sampling technique were compared with the simulations obtained by using a monodimensional, dynamic and heterogeneous model.

In this thesis work the thermal behaviour of CH_4-CPO pilot scale reformer was studied in steady state conditions through the axial profiles of temperature and composition. CH_4-CPO experiments were carried out over a 2 wt% $Rh/\alpha\text{-}Al_2O_3$ catalyst coated over 400 CPSI cordierite honeycomb monoliths or 115 CPSI silicon carbide honeycomb monoliths. This geometric configuration was chosen because the honeycomb monoliths offer several advantages: availability in the open literature of methodologies for catalytic deposition in uniform, compact and thin layers, reliability of correlations of heat and mass transfer coefficient even at very low Reynolds numbers, low pressure drops and good heat transfer proprieties and low heat capacity. First, the behaviour of the system was investigated under

standard conditions was investigated and the following observation were made: the temperature profile on the catalyst surface has a high hot-spot in the inlet section, while downstream the profile is flat and this suggests that the thermodynamic equilibrium is closely approached; the oxygen is completely consumed within few millimeters; syngas is produced also in the zone where there is oxygen. Besides, the model showed that the consumption of oxygen is kinetically controlled by external-mass transfer and its concentration on the surface of the catalyst is zero. Instead, the concentration of methane at the surface also was noticeably lower than that in the bulk gas phase, the role of external mass transfer is less important in the case of fuel consumption. Instead it was found that the consumption of the methane is mainly controlled by surface chemistry.

After this first study of the thermal behaviour, since the elimination of the hot-spot is a prerequisite for durable and stable operation in CH_4-CPO reformers, different strategies were proposed to minimize the surface temperature in the inlet zone of the reactor; we focused our attention on the catalyst design (catalyst load and channel opening) and on the inner configuration of the reactor.

Concerning the catalyst design, it was observed that, at increasing the catalyst load the rate of methane consumption increased. This is due to the promotion of the endothermic reactions chemically controlled and which consumed the heat reducing the surface temperature. The oxygen concentration profile and thus the rate of consumption were not modified because the oxygen was controlled by external mass transfer. In principle, it is also possible to act on the rate of oxygen consumption, but in this case it is necessary to modify the channel opening. In fact enlarging the channel diameter the O_2 consumption length penetrated inside the monolith and so the balance between exothermic and endothermic reaction was more favourable the local rate of oxygen consumption in moderating the surface hot-spot.

Another strategy to minimize the hot-spot is based on the inner configuration of the reactor. Three different configurations were investigated; in particular we analyzed the effect of the location of the front heat shield, which is typically adopted in the literature to limit the axial heat losses of the catalyst due to radiation. Three reactor configurations were compared in CH_4-CPO experiments: a configuration with perfect continuity between the front heat shield and the catalytic module (which behaved close to an ideal adiabatic reactor), a configuration where the FHS was separated from the catalytic monolith and a configuration where the FHS was at large distance from the catalytic module. The results showed that, at the expense of a small loss of thermal efficiency, a very moderate loss of performance (in terms of conversion and selectivity) an important reduction of the surface inlet temperatures were achieved. Preliminary experiments with propane/air mixtures suggest that the adoption of a moderately dispersive reactor can represent a promising solution for the stable operation of catalytic units treating heavier fuels than methane.

ESTRATTO IN LINGUA ITALIANA

L'ossidazione parziale catalitica (catalytic partilal oxidation, CPO) di CH_4 è una delle tecnologie più attraenti per la produzione di syngas (miscela di CO e H_2) o dell'idrogeno per applicazioni di piccola e media scala. La reazione di CPO può essere condotta a tempi di contatto dell'ordine dei millisecondi e in condizioni autotermiche, ottenendo elevate selettività a syngas. Queste caratteristiche consentono un design del reattore semplice e compatto con rapide risposte dinamiche e bassa capacità termica. Queste condizioni sono ideali per la produzione di syngas in applicazioni mobili e stazionarie. Nonostante questi vantaggi, i reattori di CPO operano con forti gradienti di temperatura e composizione e con complesse interazioni cinetiche e fluidodinamiche, e con una complessa interazione fra la fluidodinamica, processi chimici e processi di trasferimento di calore e materia. Il processo di CPO avviene principalmente con una sequenza di step esotermici ed endotermici, in cui il combustibile è prima di tutto ossidato parzialmente o completamente, e successivamente convertito a syngas dalle reazioni endotermiche di steam reforming. Come conseguenza, all'interno del volume catalitico si stabiliscono notevoli gradienti di temperatura e composizione. Le elevate temperature della superficie causano perdite di attività del catalizzatore dando luogo ad un pericoloso incremento autocatalitico della temperatura e rendendo instabile il comportamento termico dell'intero reattore. Test sperimentali prcedentemente condotti indicano che temperature di superficie inferiori ai 1000°C sono necessarie per prevenire la disattivazione del catalizzatore.

A causa della presenza di questi gradienti il comportamento del sistema non può essere descritto solamente mediante l'analisi della composizione dei gas in uscita dal reattore. Per questa ragione, nel presente lavoro di tesi è stata applicata la tecnica di risoluzione spaziale. Questa tecnica consente di seguire direttamente all'interno del reattore l'evoluzione dei profili assiali di temperatura e di composizione, mantenendo il reattore adiabatico. Per le misure di temperatura una termocoppia e una fibra ottica vengono utilizzate per misurare rispettivamente la temperatura della fase gas e del solido. Per misurare i profili di composizione, il gas viene campionato attraverso un capillare e inviato in un micro-gas cromatografo attraverso una pompa. I dati sperimentali ottenuti attraverso la tecnica di risoluzione spaziale sono stati confrontati con le simulazioni ottenute dal modello mono-dimensionale, dinamico ed eterogeneo.

Dal punto di vista sperimentale è stato studiato il comportamento di un reformer di scala pilota per CPO di CH_4 è stato studiato in condizioni stazionarie. Gli esperimenti di CPO di CH_4 sono stati condotti con un catalizzatore 2 wt% $Rh/\alpha\text{-}Al_2O_3$ depositato su monoliti a nido d'ape di cordierite (400 CPSI) o su monoliti a nido d'ape di carburo di silicio (115 CPSI). Questa configurazione geometrica è stata scelta poiché offre molti vantaggi: disponibilità di ampia letteratura riguardante le metodologie per la deposizione del

catalizzatore, attendibilità delle corelazione per il trasferimento di materia e calore anche a bassi numeri di Reynolds, basse perdite di carico, buone proprietà di trasferimento di calore e bassi calori specifici. È stato studiato il comportamento del sistema è stato investigato in condizioni standard (miscela di CH4/aria, preriscaldamento dei reagenti, portata totale di 10 Nl min^{-1}). I risultati hanno suggerito le seguenti considerazioni: i profili di temperatura hanno alti hot-spot nella sezione d'ingresso, mentre a valle i profili sono piatti coerentemente al raggiungimento dell'equilibrio termodinamico; il consumo di ossigeno è consumato in pochi millimetri; il gas di sintesi è prodotto anche nella zona dove è presente l'ossigeno. Il modello mostra che l'ossigeno è controllato dal mass-transfer poiché la sua concentrazione sulla superficie del catalizzatore è nulla. Anche la concentrazione del metano sulla superficie è notevolmente inferiore a quella in fase gas, ma l'effetto è inferiore rispetto all'ossigeno. Questo suggerisce che il consumo del metano è cineticamente controllato dalla chimica di superficie.

Dopo questo studio preliminare del comportamento termico del reattore poiché l'eliminazione dell' hot-spot è un prerequisito per operazioni stabili e durature nei reformers di CPO di CH_4, sono state proposte differenti strategie per minimizzare le temperature superficiali nella zona d'ingresso del reattore. L'attenzione è stata focalizzata sul design del catalizzatore (in termini di variazione di carico di catalizzatore e della apertura del canale) e sulla configurazione interna del reattore.

Il design del catalizzatore è estremamente importante perché permette di modificare la velocità di consumo dei reagenti e quindi il bilancio tra il calore rilasciato dalle reazioni esotermiche e quello consumato dalle reazioni endotermiche di reforming. I parametri del catalizzatore considerati in questo lavoro sono: l'apertura del canale e il carico di catalizzatore. I risultati sperimentali mostrano che, incrementando il carico di catalizzatore, la velocità di consumo del metano aumenta. Questo è dovuto alla promozione della reazione endotermica di steam reforming che, consumando il calore, riducendo la temperatura del solido. Al contrario il profilo dell'ossigeno non è modificato poiché il suo consumo è controllato dal mass-transfer. L'effetto del carico diventa più importante ad alte portate: incrementando quattro volte il carico rispetto a quello di un catalizzatore con carico standard sono stati ottenuti profili di temperatura molto moderati con una riduzione di 200 °C dell' hot-spot. Agendo sull'apertura del canale è possibile modificare la velocità di consumo dell'ossigeno. Infatti allargando il diametro del canale, la zona di consumo di O_2 si allunga riducendo localmente la quantità di calore rilasciata: in questo modo il bilanciamento tra le reazioni esotermiche ed endotermiche è più favorito moderando l'hot-spot della superficie.

L'altra strategia analizzata per minimizzare l'hot-spot è basata sulla configurazione interna del reattore. Per studiare l'effetto della dispersione frontale, tre differenti configurazioni sono state adottate e in particolare, è stato studiato l'effetto della posizione dello scudo termico frontale, che in letteratura è tipicamente adottato per limitare le perdite assiali di calore del catalizzatore per irraggiamento. Tre configurazioni di disposizione dei moduli interni sono state confrontate negli esperimenti di CPO di CH_4: una configurazione con

perfetta continuità fra lo scudo termico frontale (FHS) che si comporta come un reattore adiabatico, una configurazione con FHS separato dal monolita e una configurazione dove lo scudo è posto a una grande distanza dal modulo catalitico. I risultati mostrano che, a spese di una piccola perdita dell'efficienza termica, si ottengono una moderata perdita della performance (in termini di selettività e conversione) e un' importante riduzione della temperatura d'ingresso. Esperimenti preliminari con miscele propano/aria suggeriscono che l'adozione di un reattore moderatamente dispersivo può rappresentare una promettente soluzione per operazioni stabili di unità catalitiche che trattando combustibili più pesanti del metano.

INTRODUCTION

The production of synthesis gas is of great importance in the chemical industry, because synthesis gas is the feedstock for methanol and Fischer-Tropsch synthesis. An important resource for synthesis gas production is natural gas, which consists mainly of methane. Unfortunately, natural gas occurs often in remote locations, and costly transportation motivates the research to transform it to synthesis gas and finally to transportable liquids. Conventional steam-reforming technology is not suited for decentralized synthesis gas production, because steam reformers are large, expensive plants that cannot be scaled down for small-scale operation in remote gas fields. An alternative to steam reforming is the catalytic partial oxidation, which has received a considerable attention. In fact, during the last 15 years it provides close to 100% methane conversion and syngas yields >90% in millisecond contact times by operating at high reaction temperatures, which in turn can be accomplished by running the process adiabatically. Since the catalytic partial oxidation is fast and exothermic, it is suitable to realize compact reformers, which have a rapid response to transient load demands. These aspects make this process suitable for remote gas field applications, and also for all stationary and mobile applications related to the recent development of a small-to medium scale technology for the production of syngas and H_2. The stationary applications include the production of H_2-rich steams for the fuelling of hydrogen-driven vehicles or residential cogeneration systems, but also for the enhancement of gas turbines performances through the development of H_2 stabilized combustors. On board applications deal with the used of solid fuels cells (SOFTs) for auxiliary power units (APUs) on heavy duty to supply power to auxiliary cab devices (condition systems, GPS) and trailers (cryogenic circuits). On-board generation of syngas may also be applied on conventional ICE vehicles to speed up the cold-start phase of catalytic converters and to serve as reducing gas for NO_x trap regeneration and for the SCR of NO_x.

The CPO process is characterized by a complex interplay between heat transfer, mass transfer and surface chemistry. reaction processes going on inside of these reactors. Such an interplay determinates the formation of pronounced hot spot at the very at the very inlet of the reactor, with surface peaks hundred of degree higher than the gas temperature. So far it has been show in literature that shape of the surface temperature is due to the rapid O_2 consumption and the heat release which occurs at the very reactor inlet, partially balanced by the reforming reactions which are spread along the monolith length and give rise to syngas formation. The experimental investigations clearly show that under severe operation conditions (extremely high flow rates and presence of preheating) the CPO reformers show a unstable thermal behaviour, since progressively increasing temperature are measured in the inlet reactor portion. This reactor heating can be explained by loss of activity, which little affects the conversion of O_2, while strongly influences the more chemically controlled reforming reactions.

In this respect the study of thermal behaviour of a short contact time CPO reformer has an extreme importance because it can provide the guidelines for optimal reactor design with minimum hot-spot temperature.

This work deals with an experimental and modelling investigation on the thermal behaviour of a short contact time CPO reformer, operating with 2 wt% $Rh/\alpha\text{-}Al_2O_3$ catalyst supported on monoliths. This geometry allows to have low pressure drop and high gas flow rate, conditions to minimize the volume of the reactor. Ceramic foam monoliths have been mostly studied in the literature so far, but honeycombs are the support of choice for several application such as the on-board H_2 production. The experiments were performed in adiabatic reformers whit pre-heated and autothermal conditions and with stoichiometric methane/air. The axial temperature and composition profiles were obtained using the spatially sampling technique which herein first demonstrated for the honeycomb geometry. Tests with diluted propane/air mixture were also performed.

A thermal behaviour study of the methane CPO was performed to propose an optimal reactor design where the hot-spot were minimized. Firstly the catalyst design was considered, and the effects of catalyst load (240, 720, 935 mg) and then of the channel opening were evaluating at different flow rates (10, 15, 20 Nl min^{-1}). Subsequently, the effect of the inner layout of the reactor was studied, in particular the effect of the relative position of the catalytic monolith and the upstream front heat shield was studied. The experimental results are compared with the respective simulations obtained by dynamic, monodimensional, heterogeneous, single channel model. Then, a optimal reactor configuration was tested for propane CPO. In this case the temperature are more elevated than in the methane CPO, and so it is more important the problem of the inlet catalyst heating is even more severe.

CHAPTER 1

STATE OF THE ART

1.1 INTRODUCTION

Beginning from the sixties of last century the technologies for the production of energy from fossil fuels had a transition to a new era where the reduction of pollutant was important. In fact the combustion of fossil fuels produces elevated quantities of carbon dioxide, but also many chemical species some of which are toxic for many living organisms. In this scenario gas natural has gained a position of great importance because of its abundance [1]. In fact according to the International Energy Agency (IEA) the world's energy demand from natural gas, which consists mainly of methane, is expected to increase by 30-40% in a 25 years perspective [2]. Even thought the world has large deposits of natural gas, most is located in remote areas and consequently it must be transported across vast areas distances to reach its market with high cost of storage and transportation. Therefore the conversion of methane to more useful and easily transportable chemicals (as liquid) has been given high priority by scientists. But the selective attack of the molecule to break one C-H bond and to substitute a hydrogen with another functional group (for example the group –OH) is difficult because of high CH_3-H(g) bond dissociation energy (439.3 kJ/mol). Different methods of methane activation have been investigated, but yields tend to be low to compete with oil because the products are more reactive than methane. For example in the direct oxidation of methane to methanol, or formaldehyde the maximum yields so far obtained were around 8% and 4% respectively [3]. At this time, the only economically available route for the conversion of methane into more valuable chemicals is via synthesis gas. Synthesis gas can then be converted to paraffin liquid fuels through Fischer-Tropsch reaction on Fe, Co, Ru and similar metals,

$$n\,CO + 2n\,H_2 \rightarrow \left(-CH_2-\right)_n + n\,H_2O \qquad (1.1)$$

or to methanol over Cu/ZnO and then to gasoline by MTG process over zeolite catalyst [4]. Synthesis gas is also used for the production of methanol, dimethyl ether, acetic acid and oxoalcohols. Moreover the synthesis gas is a energy carrier from which hydrogen is often produced. In the last years, hydrogen has been the centre of attention of public opinion as a possible 'pole star' of a new energy future because it is a clean vector (if burnt, produces only water)[4].

1.2 SYNTHESIS GAS PRODUCTION

Synthesis gas can be produced from various fossil sources, such as natural gas, naphtha, residual oils, coke from petroleum and coal. Natural gas, however is the raw material of greatest interest. Several synthesis gas are available, depending on the purpose of industrial application: steam reforming, partial oxidation, autothermal reforming.

- *Steam reforming*

$$CH_4 + H_2O \leftrightarrow CO + 3\,H_2 \tag{1.2}$$

The first description of a process for the conversion of hydrocarbons with steam was published in 1868 using CaO as a medium, resulting in the formation of $CaCO_3$ and hydrogen. In 1890 Mond and Langer improved the process by using a nickel catalyst, and it was subsequently used, in combination with Fisher-Tropsch technology, by Germany in World II and South Africa during the Apartheid era for the synthesis of chemical such as fuels and alcohols [2]. The reaction is strongly endothermic (ΔH^0_{298} = 206 kJ mol^{-1}) and leads to gas expansion. This means that it is favoured at low pressure and at high temperature. The steam reforming, in industrial practice, is carried out at 900°C at the pressure of 15-30 atm in a fired tube reformers (Figure 1.1), which are fired heater with catalyst (nickel supported on oxide carrier, typically Al_2O_3 or ZrO_2) filled tubes placed in the radiant part of the heater [6]. The superficial contact time is 0.5-1.5 s, which corresponds to residence times of several seconds. The methane conversion, in steam reactions, are typically in the order of 90-92%, with a synthesis gas composition similar to that determined by thermodynamic equilibrium [4]. The principal disadvantages of the steam reforming is that only the 35-50% of the total energy input, given by external combustion of the fuel gas, is absorbed by the reforming process. Therefore the heat of fuel gas is usually used in the convective part of the reformer by preheating the feedstock and generating steam, thus bringing the overall thermal efficiency over 85%. Another critical aspect of steam reforming is the formation of carbonaceous residues which can occur according to these reactions: $2\,CO \rightarrow C + CO_2$, $CH_4 \rightarrow C + 2\,H_2$, $CO + H_2 \rightarrow C + H_2O$ (Bouduard reaction). The carbon formation must be prevented for two reasons. Firstly, coke deposition on the active sites of the catalyst leads to deactivation. Secondly, carbon deposits can cause total blockage of the reformer tubes, resulting in the development of 'hot spots' [7]. One of the methods for limiting the formation of carbonaceous species is the use of a high steam/methane ratio in the feed mixture. As an increase in this ratio also involves a cost increase, it is preferable to use the lowest steam/methane ratio compatible with the necessity of controlling the formation of carbonaceous residue. Typical values of this ratio range from 2 to 5, depending on the synthesis gas and use.

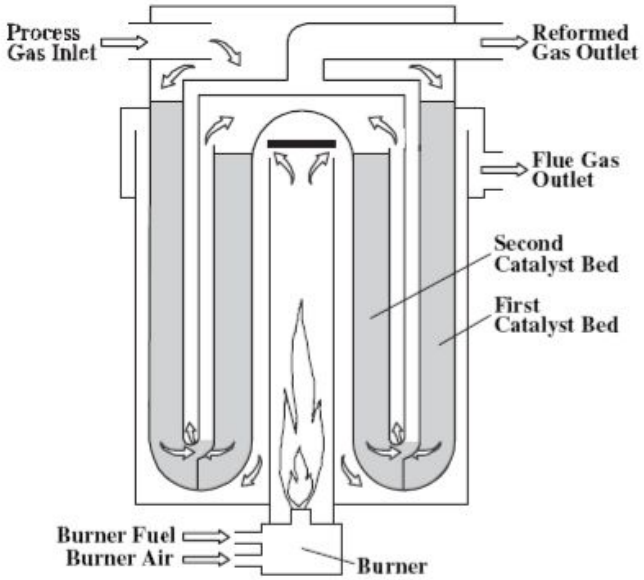

Figure 1.1: Heat exchange reformer.

- *Partial oxidation*

$$CH_4 + \frac{1}{2}O_2 \rightarrow CO + 2\,H_2 \tag{1.3}$$

The reaction is slightly exothermic (ΔH^0_{298}= -37 kJ mol^{-1}), therefore can be performed in burner without the catalyst. In the absence of the catalyst the temperature must be sufficiently high to reach the total conversion of methane, in fact the temperature of the gas at the outlet is about 1000-1100 °C. This process is not suited for small-scale production because it operates at 30-100 atm and with pure O_2 to prevent NO_x formation and nead high temperature [4].

- *Autothermal reforming (ATR)*

$$CH_4 + \frac{3}{2}O_2 \rightarrow CO + 2\,H_2O \tag{1.4}$$

$$CH_4 + H_2O \rightarrow CO + 3H_2 \tag{1.5}$$

$$CO + H_2O \rightarrow CO_2 + 2\,H_2 \tag{1.6}$$

This process was developed by the Danish company Haldor Tposoe at the end of 1950s. The process combines partial oxidation and steam reaction in a single reactor and in this case the heat for the reforming reaction is supplied by combustion of part of the reactants. The overall reaction is adiabatic, meaning that there is no exchange of heat with the surroundings (except a very limited heat loss). The ATR reactor (Figure 1.2) consists of a

burner, a combustion chamber and a catalyst bed, all of which are contained in a refractory lined pressure shell. A mixture of natural gas and steam is partially converted by pressurized combustion under fuel-rich conditions in the combustion chamber. The temperature in the combustion chamber is in the range of about 1100-1300°C near the catalytic bed and up to more 2500°C in the flame core depending upon the process conditions. In the combustion chamber also the steam reforming and the water gas shift take place in homogeneous phase due to the high temperature. In reality a very large number of chemical reactions take place in the combustion chamber involving radicals. The oxygen is quantitatively consumed by the combustion reactions. However, the methane conversion is not complete in the combustion chamber. In fact the final conversion of methane takes place in the catalytic bed. The synthesis gas leaving the ATR reactor at chemical equilibrium typically between 850 and 1100°C. ATR reactor is soot-free under normal circumstances. The fuel rich combustion takes place in a turbulent diffusion flame and intensive mixing is required to prevent soot formation. Soot formation is unwanted and would reduce the carbon efficiency of the process, beside soot particles should be removed from the synthesis gas [7].

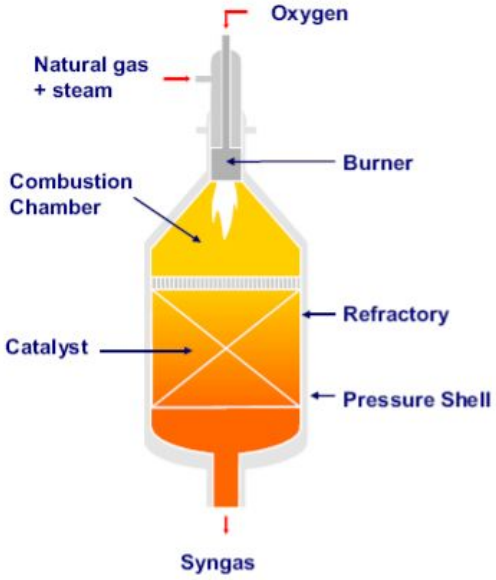

Figure 1.2: ATR reactor.

1.3 CATALYTIC PARTIAL OXIDATION

The technologies described in the previous section are in commercial use today for the production of synthesis gas. However, substantial efforts to develop new technologies are undertaken due the fact that the most intensive part of large-scale plat is the synthesis gas generation (SGU). The focus of many of this development is to reduce or to eliminated the used of oxygen and/or to reduce the size of the reactor in SGU [5]. Actually catalytic partial oxidation has received particular attention because it is one of the most attractive

technologies for the production of syngas and hydrogen in small to medium scale [8]. In fact CPO can be carried out in compact reactors with rapid dynamic response and with low heat capacity, which is ideal for mobile and stationary small scale production of syngas. Besides, the catalytic partial oxidation has thermodynamic advantages with respect to a reforming process [3].

1. The reaction is mildly exothermic (ΔH^{0}_{298}= -37 kJ mol^{-1}), while steam reforming is highly endothermic (ΔH^{0}_{298}= 206 kJ mol^{-1}). Thus, a partial oxidation reactor would be more economical to heat. In addition it can be combined with endothermic reactions, such as steam reforming or dry reforming with carbon dioxide to make this processes more energy efficient.

2. The stoichiometric H_2/CO ratio is around 2 and this ratio is ideal for the downstream process avoiding the need to remove valuable hydrogen, which is produced in excess in steam reforming.

3. The gas product can be extremely low continent of carbon dioxide content, which must often be removed before synthesis gas can be used downstream.

4. This technology avoids the need for large amounts of expensive superheated steam. However, an oxygen separation plant, which is also costly may be required in the cases where nitrogen is undesirable in high-pressure downstream processes. Air can however guarantee the autothermal operation and is desirable in small scale applications.

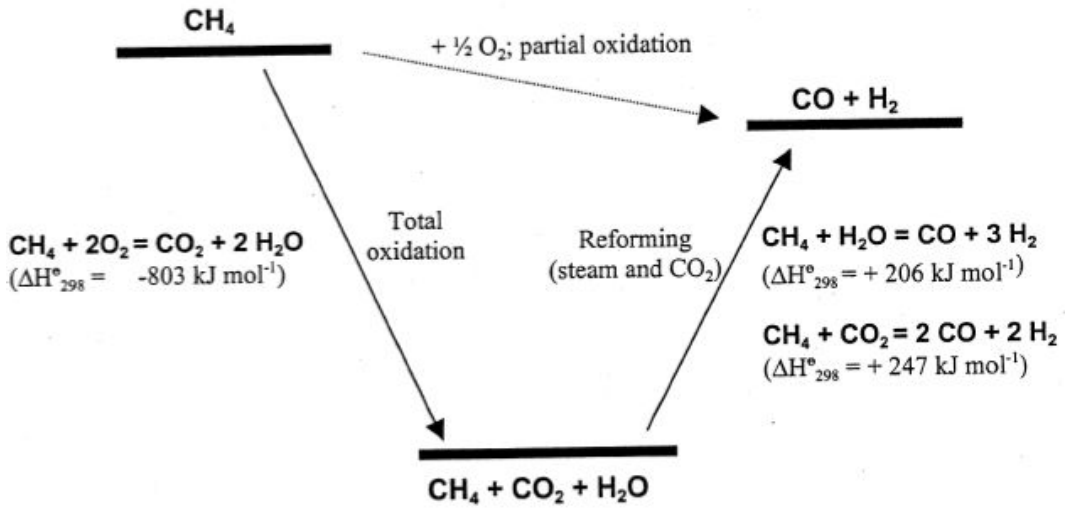

Figure 1.3: Thermodynamic representation of the partial oxidation of methane.

Even though the advantages, previously described, the catalytic partial oxidation has hot spot in the inlet section, which can deactivate the catalyst [9].

1.3.1 CATALYST DEVELOPMENT

The first papers detailing with the catalytic partial oxidation of methane to synthesis gas were published in 1929 by Liander [10], in 1933 by Padovani and Franchetti [11] and by Prettre [12]. However, high yields of synthesis gas were only obtained at temperatures in excess of 850°C. The latter studies showed that below this temperature non-equilibrium product distributions were observed. In addition, carbon formation over the supported nickel catalysts used was not studied in any detail. Because of this factor, as well as the success of the steam reforming process, partial oxidation was left aside for decades. In 1970 Huszar et al [13] examined the importance of diffusion effects during methane partial oxidation by studying the reaction of 25% CH_4: air mixture over a single grain of Ni/mullite catalyst in the temperature range 760-900°C. They saw ignition and extinction characteristic of the catalytic system. They observed also that Ni catalyst would deactivate in an oxidizing environment because of $NiAl_2O_4$ formation, but the activity could be partially recovered by hydrogen treatment. They concluded that the formation of H_2/CO required the presence of reduced metallic Ni, achieved by using O_2 deficients condition, and that the kinetics of the overall process were limited by the rate of diffusion of O_2 at the catalytic surface was essentially zero, allowing the Ni to be maintained in the zero valent state. In the late 1980s Green and co-workers [3] began a renaissance in the study of methane partial oxidation. While investigating trends in the behaviour of the lanthanides for oxidative coupling using pyrochlores containing noble metals and rare earth metals, they observed high yield of synthesis gas. Studies revealed reduction of the noble metal ruthenium catalyst which had excellent activity for methane partial oxidation. This time no carbon could be seen on the post reaction samples, and confirmation of this was obtained by high resolution electron microscopy. This observation prompted a detailed investigation of stoichiometric methane partial oxidation over noble metals, and other catalysts, by a very substantial number of research group. Compared to the early success of methane steam reforming, catalytic partial oxidation remained almost unexplored until 1990. As a consequence, the publications appearing in the 1990s were for the most part concerned with catalyst screening, although the effect of the principal system proprieties such as operating temperature and pressure were also studied. By the ends of 1993-1994 the focus began to shift towards improving the catalyst stability and performance. A more important results was reported by Hickmann and Schmidt [14,15] who studied the reaction using an adiabatic reformer atmospheric pressure in a short-contact time with catalyst based on noble metal and they obtained conversions near to the thermodynamic equilibrium. In conclusion, the experimental studies up 1993-1994 revealed several important aspects in catalytic partial oxidation of methane as the effect of nitrogen dilution and total pressure, an apparent thermodynamic limitation, mass transfer limitations and the importance of accurate temperature measurement [16]. The first simulation of methane partial oxidation over Pt and Rh surfaces were given by Hickmann et al. [17]. The model consisted of 19 elementary steps including adsorption, desorption and surface reactions.

Actually, the research for the process of catalytic partial oxidation regards:

- the optimization of the catalyst and the support;

- the reaction mechanism;
- the optimal reactor design.

Beside, the catalytic partial oxidation of logistic fuel such as gasoline and diesel has gained particular attention due to its potential to provide the fuel for on-board and on-site fuel cells. Reliable long-term applicability of CPO of logistic fuels call for a better understanding of the complex interaction between gas phase and surface precursor reactions, homogeneous gas-phase reactions as well as mass and heat transfer. The major experimental challenge is the complexity and variability of the fuel composition, which demands for rapid screening of CPO of many fuel components and mixture, that means a rapid analysis of the product composition is needed to study many components and mixtures at varying parameters. Besides, although physical proprieties of logistic fuels are regulated by several specifications, the chemical composition is varying within broad ranges, affected by the feed stock of the refinery or geographic/seasonal customization of the fuel. Consequently, the studies of the catalytic partial oxidation of logistic fuels is commonly restricted either on the detailed investigation of simple reference fuels, which can be a single-component, such as i-octane or on the parameterization of empirical models to describe reactor performance [18]

Also the propane is drawing attention in hydrogen production studies because it is a constituent of LPG. LPG is a commercial gas that is easily transported and stored on site. Moreover, due to its composition (short aliphatic C3-C4 chains and absence of sulphur or other electronegative atoms), LPG is reported to present some significant advantages compared to heavier feedstocks, especially in terms of catalytic resistance to deactivation led by limited carbon deposition. The catalytic partial oxidation of propane is more exothermic than that of methane and autothermal applications can realized easily, but it is necessary to identify the working condition. In fact modelling studies [19] showed that underlined concentrated propane/air mixtures caused temperature peaks of the surface near 2000°C, which are expect to irreversibly deactivate the catalysts.

1.3.2 REACTION MECHANISM

The mechanism for the catalytic partial oxidation of methane to synthesis gas has been the subject of a debate which to date is still not completely settled. Two distinct mechanisms have been proposed for explaining the formation of syngas [3].

- *Direct oxidation mechanism*

This mechanism, also called pyrolisis-oxidation, assumes that H_2 and CO are primary reaction products formed in the oxidation zone at the catalyst entrance. This mechanism assumes that a dissociative adsorption of CH_4 with the formation of carbon species and H adatoms occurs at the entrance. Then surface carbon reacts with surface oxygen to CO and hydrogen atoms combine to H_2. So the basic reactions are:

$$CH_4 \rightarrow C_S + 4H_S \quad (1.8)$$

$$C_S + O_S \rightarrow CO \quad (1.9)$$

$$H_S + H_S \rightarrow H_2 \quad (1.10)$$

The by-products CO_2 and H_2O are formed by their combustion between oxygen and H_2 and CO, but also for the reaction of methanation:

$$H_2 + \frac{1}{2}O_2 \rightarrow H_2O \quad (1.11)$$

$$CO + \frac{1}{2}O_2 \rightarrow CO_2 \quad (1.12)$$

The main evidence in favour of the direct path is the observation of syngas at extremely short time, in presence of unreacted O_2 [20]. H_2O and CO are in this case interpreted as non-selective oxidation products.

- *Indirect oxidation mechanism*

This mechanism, also called combustion-reforming, postulates two-zone model with strongly exothermic CH_4 combustion at the catalyst entrance, followed by strongly endothermic steam and CO_2 reforming downstream. In this reaction mechanism the synthesis gas is the secondary product. Therefore the reactions are:

$$CH_4 + 2O_2 \rightarrow CO_2 + 2H_2O \quad (1.13)$$

$$CH_4 + H_2O \rightarrow CO + 3H_2 \quad (1.14)$$

$$CH_4 + CO_2 \rightarrow 2CO + 2H_2 \quad (1.15)$$

One major proof of the existence of such an exothermic-endothermic sequence has been the observation of sharp hot-spot temperature at the entrance or on reduced syngas yields and increasing total oxidation products with decreasing time contact time [21].

Published mechanism studies follow essentially two approaches. One approach is due to the study methane CPO under realistic conditions (high catalyst temperatures and atmospheric or elevated temperature). Typically, in this studies the reaction mechanism is inferred from the outlet concentration. Such an approach is claimed to be not rigorous for the kinetics analysis, since frequently both direct and indirect scheme can equally justify the data. Another approach uses well-defined isothermal lower-pressure or diluted conditions different from the technical application. An example is the TAP experiment with isothermal condition, either under vacuum or diluted atmosphere. Depending on the

experimental conditions, different product development is inferred and different mechanistic conclusions are drawn. Recently, a new capillary sampling technique combined with a quadrupole mass spectrometry has been developed and applied in autothermal reactors over Rh and Pt foams [22-25]. Spatial and temporal resolved data have been collected inside the catalyst bed under both transient and steady-state conditions. The results have shown that the reactor can be divided into a short, initial oxidation zone, where H_2 and CO are produced by direct oxidation in the presence of gas phase O_2, followed by a reforming zone where the syngas are formed by steam reforming.

Tavazzi and at. [26] had carried out a kinetic study of CH_4-CPO over Rh catalyst at low Rh load using an isothermal annular reactor, wherein heat and mass transfer artifacts are minimized and high space velocities allow to skip the thermodynamic control. Strong pieces of evidence were obtained in favour of an indirect kinetic scheme because of:

- shape of the temperature profiles where a maximum was always present at the beginning of the catalyst, followed by a progressive decrease of the temperature along the layer, consistent with the occurrence of an exothermic-endothermic reaction sequence;
- the selectivity to H_2 decreased markedly at increasing GHSV (Gas hourly space velocity).

The data could be described by a scheme consisting of methane oxidation, reforming reactions, the reversible WGS reaction, and the consecutive oxidations of H_2 and CO.

1.3.3 CATALYSTS

The production of synthesis gas by oxidation reactions can be performed in the short contact time regime. Short contact times reactors hold the promise of greatly reducing the reactor volume. Short contact times can be reached by using structured catalytic system where the catalytically active materials are deposited on the structured ceramic or metallic substrates. This group of structured catalyst includes monolithic catalysts with honeycomb structure, ceramic foams, corrugates-plate catalyst with cross-flow or parallel channels as well as metallic gauzes. The honeycomb monoliths result in much shorter start up because of their better heat transfer proprieties and lower heat capacity. Also, at flow rates of practical interest, honeycombs performer better than packed beds in terms of conversion, selectivity and pressure drops. The effort to minimize the pressure drop over the catalytic system led to the development of corrugates monolithic reactor based on FecrAlloy (Figure 1.4), an alloy containing aluminium (0.5-12%), chromium (20%), yttrium (1-3%), iron and kanthal (an alloy containing aluminium, chromium, cobalt and iron). Additionally, honeycomb monoliths offer several advantages for experimental investigations and its quantitative analysis; among them representativeness of the laboratory-scala data; avaibility in the open literature of well-established methodologies for catalytic deposition in uniform compact and thin layer and the ability to monitor the axial temperature profiles along the channel by means of multiple thermocouple and the reliability of correlation for

heat and mass transfer coefficient even at very low Reynolds number. Most of these aspects make honeycombs preferable to foams for the kinetic investigation.

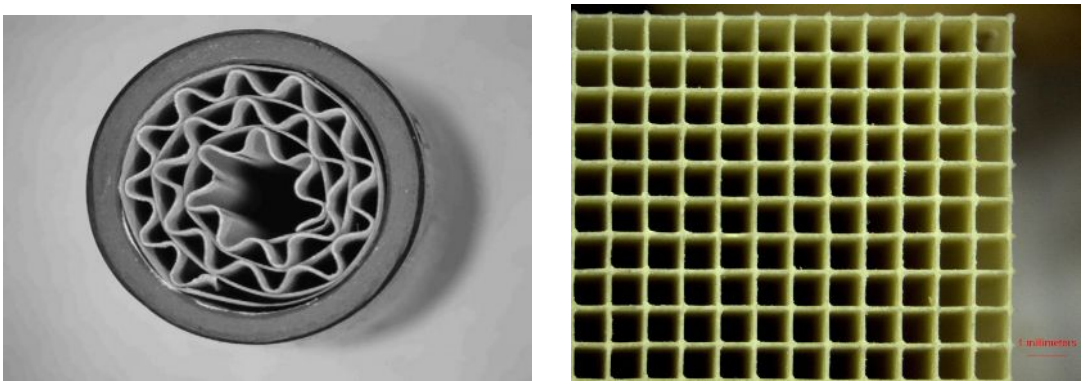

Figure 1.4: Corrugate monolith (left) and cordierite honeycomb monolith 600 CPSI (right).

A large number of different catalyst have been suggested for the catalytic partial oxidation of methane. Noble metals, nickel, and to a lesser extended cobalt are active in the CPO process. However, not all these catalyst are stable on a long term basis and the choice of a particular metal is often a balance between several critical parameters. These parameters comprise the catalytic activity and the long-term stability, the selectivity towards synthesis gas production, a lower propension towards unwanted side-reactions (especially carbon formation), the sensitivity towards sulphur poisoning and the price of the active element. Nickel catalyst show the highest activity, and they are attractive due to their low price. However, nickel catalyst are particularly sensitive to sulphur poisoning and to thermal sintering. Noble metal are generally recognized as superior in terms of activity and stability in CPO of methane as compared to metal based transition catalyst, but there are marked difference between the individual noble metals. Palladium is prone to rapid carbon formation at low O_2/HC stoichiometries leading to a build-up of pressure drop over the catalyst, but also catalyst based on platinum has revealed a propensity toward carbon formation [27]. A stable catalytic performance with low (<400°C) light-off temperatures in the CPO process can be obtained using rhodium, but often the rhodium price is prohibitive for large-scale facilities. Palladium, ruthenium and iridium catalyst are considerably less active than rhodium catalyst, but exhibit sufficient activity for many practical applications [28]. It was proved that the best noble metal is rhodium because of high selectivity to H_2, low volatility and resistance to coke formation [15].

Many of the critical parameters for the choice of the active phase metal also depend on the choice of the support as specific metal-support interactions can influence the reducibility of a metal oxide or stabilise the particle dispersion of the metal. Widely investigation support phase are ZrO_2, TiO_2, CeO_2 and Al_2O_3. The optimal support would maintain the dispersion of the active phase and ensure thermal stability also in severe working condition. It was proved that Rh/α-Al_2O_3 is a catalytic system adapted for the partial oxidation of methane to synthesis gas [29].

Other aspect of catalyst proprieties such as selectivity may also come into play when choosing a catalyst for industrial applications. The selectivity to higher hydrocarbons is important as they are prone to polymerize and form carbon in downstream equipment. The phenomenon is most pronounced when pure oxygen is applied as oxidiser, while negligible amounts are formed with air as the oxidant and using platinum or rhodium [28]. Besides, the effect of temperature on the homogeneous reactions is important.

In Table 1.1 are reported the principal geometry and catalyst proposed in literature.

Catalyst	contact time	reference
Sponge		
Rh	100	[30]
Pt	100	[30]
Sinlge gauze		
Pt	0.21	[31]
Pt/10% Rh	0.21	[14]
Foam		
11.6% wt% Pt	0.5	[15]
4 wt% Pt	1	[33]
4 wt% Rh	1	[33]
9.8 wt% Rh	<10	[15]
0.56 wt% Rh	<10	[15]
9.9/9.9 wt% Rh/Pt	<10	[15]
0.1 wt% Pt	40	[32]
0.1 wt% Rh	40	[32]
0.1 wt% Rh	75	[34]
Honeycomb monoliths		
1.5 wt% Pt	10	[15]
1.5 wt% Rh	140	[15]
5 wt% Ni	70	[35]
5 wt% Pd	70	[36]
Anular reactor		
0.5 wt - % Rh/α-Al_2O_3 (400 CPSI)	32	[26]

Table 1.1: Catalyst and geometry used in the experimental studies of CPO of methane.

The hydrogen production from catalytic partial oxidation of propane was studied by Venvik and at [36] in alumina foams and microchannel metallic monolith (Frecralloy). Temperature profiles obtained along the catalyst/reactor axis under comparable condition show that the gradient are smaller in the Rh/Al_2O_3/Fecroalloy microchannel reactor than in the Rh/Al_2O_3 foams. Besides, the Rh/Al_2O_3 foams show significant deactivation upon a few temperature cycles under reactant exposure, while no deactivation is observed for the Rh/Al_2O_3/Fecroalloy microchannel reactor.

1.4 CPO TECNOLOGICAL APPLICATION

The catalytic partial oxidation, as previously mentioned, is suitable for stationary and mobile application related to the development of a medium to small scale technology for the production of syngas and H_2.

1.4.1 FUEL CELLS

The CPO can be used in fuel cell, in particular in molten carbonate fuel cells (MCFC) and in solid oxide fuel cell (SOFC) because these types run on a mixture of hydrogen and carbon monoxide and they have resistance to poisoning by impurities in the fuel. Therefore it is possible to operate the cell directly on hydrocarbon fuel without the need of a system to remove all the trace of CO. The SOFCs are more used because of the freedom in the carrying out of forms and volumes.

The solid oxide fuel cell is characterized by having a solid ceramic electrolyte, which is a metal oxide. The basic component of the SOFT are the cathode, at which oxygen is reduced to oxide ions, which then pass through the solid electrolyte under electrical load, to anode, where they react with the fuel, hydrogen and carbon monoxide, producing water and CO_2, as well as electricity and heat (Figure 1.5). The theoretical maximum efficiency is very high, in excess of 80%. The SOFC operates at elevated temperature, conventionally between 800-1000°C. In small-scale devices being developed for stand-alone or remote applications, oxygen or air is used as oxidant rather than steam to convert the fuel in syngas. In fact the cost and the complexity associated with using large quantities of stem, which makes its use less favourable in small-scale applications. In fact the use of the oxygen, or air, is much simple and cheaper in terms of configuration and manufacture. However, it does lead to an inherent efficiency due to the large energy loss in oxidising the hydrocarbon. Besides, if an excess of oxygen is used then will be the a tendency for full oxidation to CO_2 and H_2O, which cannot be electrochemically oxidised and so there is a further loss of efficiency compared to the using steam as oxidant. Although for most SOFCs under normal operation steam will be used to internally reformer the natural gas, self-sustained internal reforming is precluded during the start-up from cold and the operation at low power levels because of the strongly endothermic nature of steam reforming. While the partial oxidation of hydrocarbons, being exothermic, offers the potential for the start-up and self-sustaining operation of internally reforming SOFTs running on natural gas or other hydrocarbons at lower power [37].

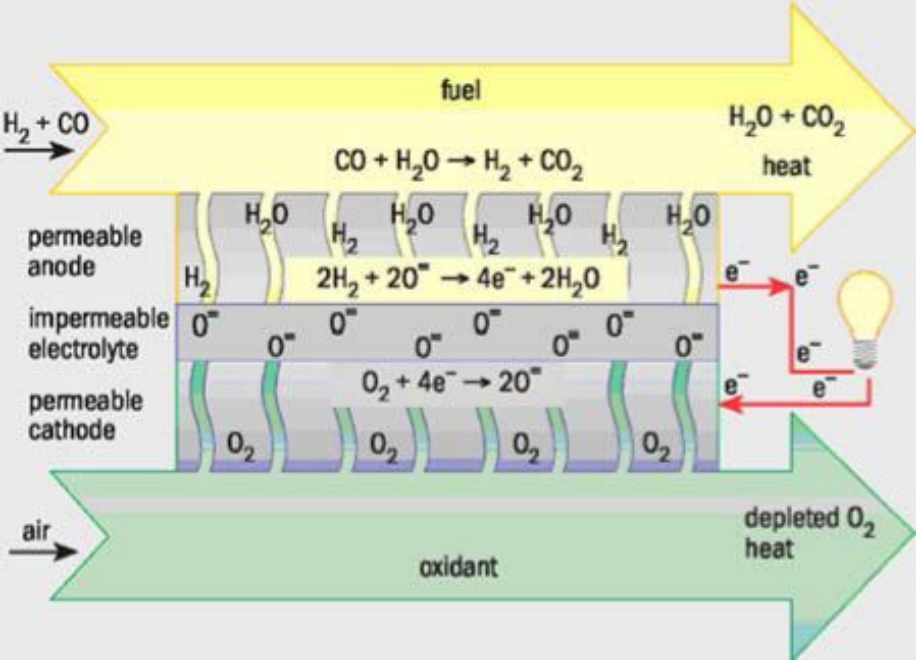

Figure 1.5: Operating principle of a solid oxide fuel cell.

Delphi automotive system has developed a gasoline fuelled APU (auxiliary power unit) on base of a solid oxide fuel cell stack (SOFC) [38]. In passenger vehicles, it is intended to supply energy to the vehicle electrical system and to power an air conditioning unit. At the current stage of the development the system has an output of around 2kW. The overall system is comparably compact, featuring a power density upper 33 Wl^{-1}. Also APU concepts have been presented, that combine a PEM fuel cell (polymer electrolyte membrane) with a fuel processor, enabling the use of a variety of hydrocarbons instead hydrogen. Contrary to the SOFC the PEM requires a carbon monoxide free anode gas supply. Hence, the fuel processor are rather complex, because aside from the reformer a carbon monoxide cleaning unit has to be integrated. In comparison to APU applications these system have a much higher power output ranging above 50 kW and reach much higher power density. The fuel cell-based auxiliary power unity (APU) can be designed for much higher power outputs with a much efficiency compared to the conventional electrical power generation in today's internal combustion engines via engine and generator. APU allows to be independent from engine operation and electrical energy is available any time, even when engine is turn of.

1.4.2 CATALYTIC COMBUSTION

The CPO is also studied for power application. In fact it can be used within gas turbine combustor. This system is composed by a compressor, a combustion chamber and a turbine (Figure 1.6).

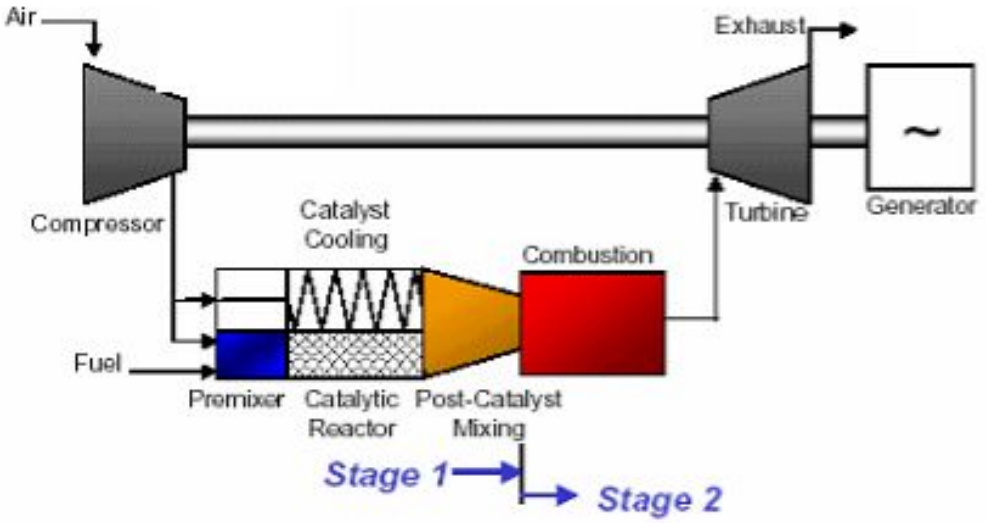

Figure 1.6: Flow diagram of gas turbine combustor.

The combustion chamber with rich catalytic learn burn (RCL) is based on two step (Figure 1.7) [39]:

- Catalytic partial oxidation in rich condition, where only a portion of the inlet air (15%) is mixed with the fuels. While the remaining air is mixed with the stream coming from the catalyst exit cooling the catalyst. During this phase there is not NO_x emission.
- Homogeneous combustion operating in very weak conditions. Due to high dilution combustion, with H2 high percentage, is done at low temperature, thus reducing NO_x emission.

The RCL process allows to work outside the inflammability limit, to prevent the pre-light off or flame flashback, to reduce the deactivation of the catalyst because the excess of fuel reduce the area surface oxidation and the metal volatility. Finally the operation in rich region are more tolerant of variations in both air and fuel flow.

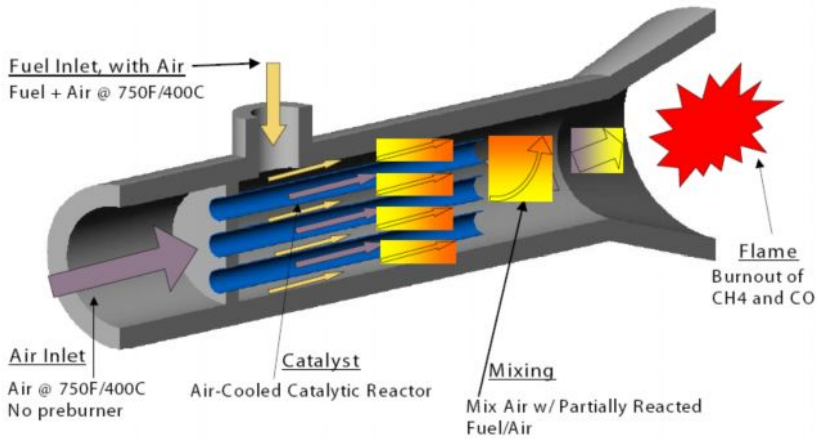

Figure 1.7: RCL combustion system.

CHAPTER 2

PILOT-SCALE REFORMER AND EXPERIMENTAL PROCEDURES

2.1 INTRODUCTION

In this work the CPO experiments were performed in a pilot-scale reformer, placed under fume hood, at high flow rates: the rig is capable of feeding mixtures of methane (or propane)/air up to 45 Nl min^{-1}. In the first part of the chapter the pilot-scale reformer (Figure 2.1) and the instruments for the data acquisitions will be described. Afterwards, the start-up and shut-down procedures and the operating conditions will be explained. Finally, the last two paragraphs will present the preparation and the characterization of Rh-based catalysts.

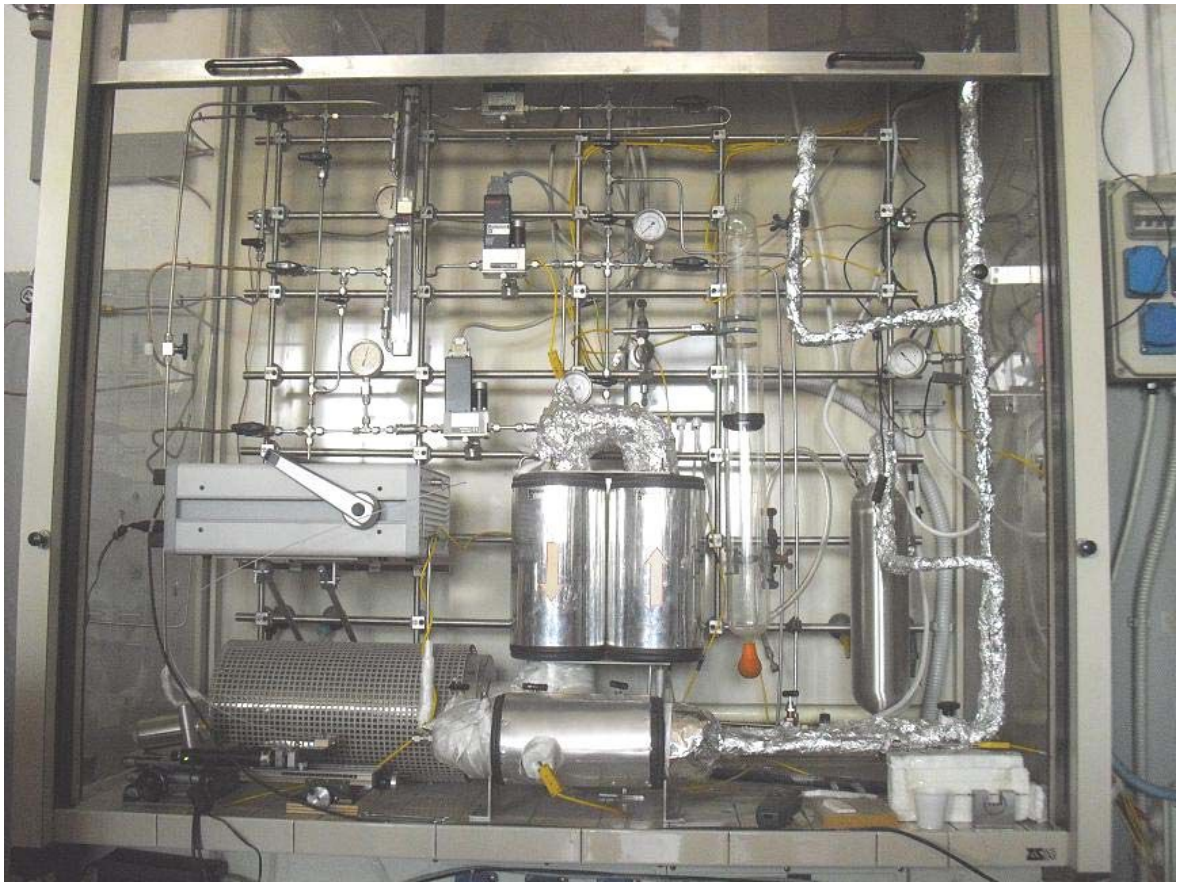

Figure 2.1: Pilot-scale reformer.

The experimental rig, reported in Figure 2.2, can be divided in three different sections: feed, reaction and gas analysis. These sections are connected through stainless steel lines of ¼ inch nominal diameter.

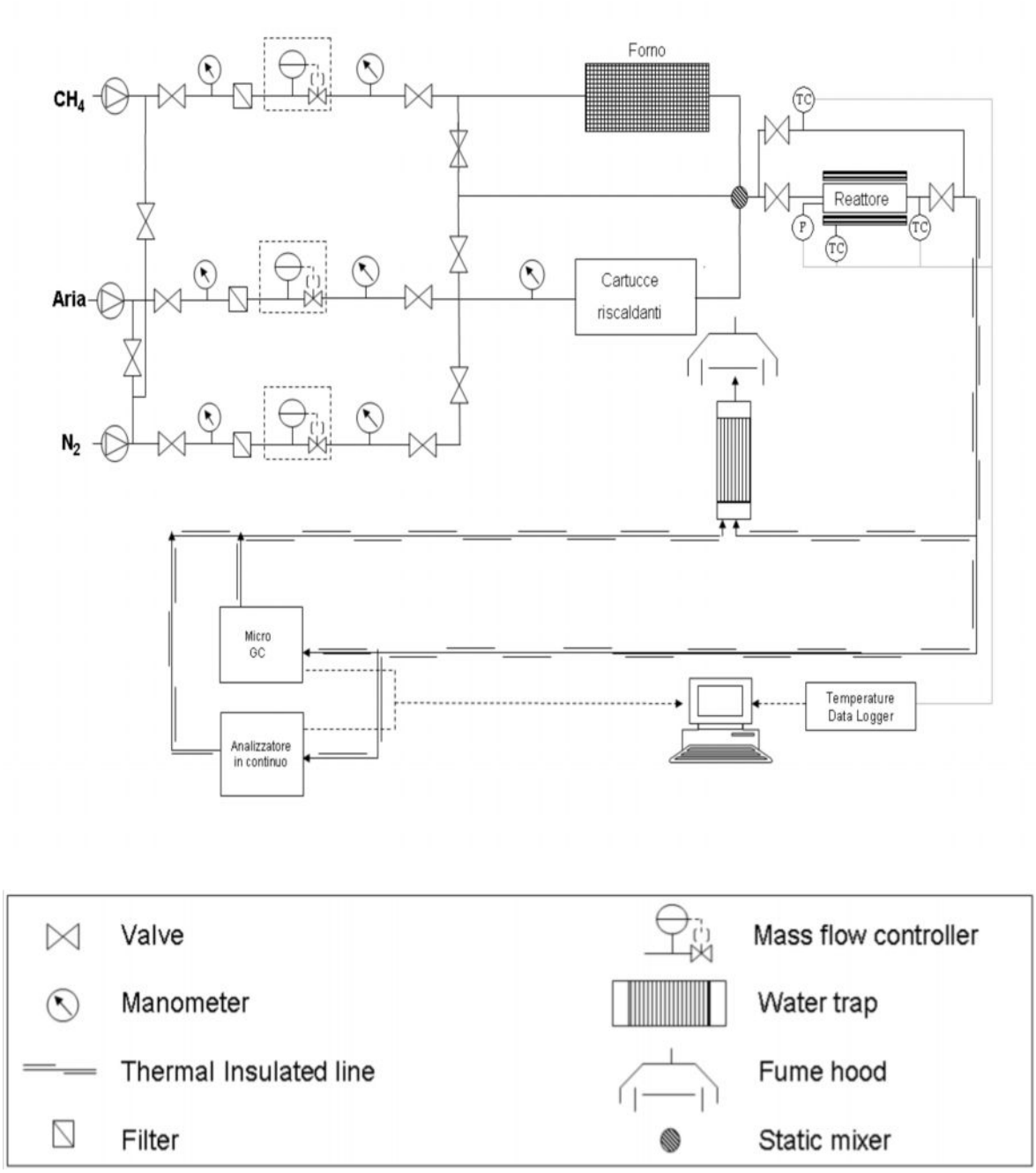

Figure 2.2: Experimental rig.

2.2 FEED SECTION

In the feed section three different lines allows feeding the gas stream to reaction section:

- the first line is used to feed methane or propane, stored in gas cylinders outside the laboratory;
- the second line is used to feed air, stored in gas cylinders outside the laboratory;
- the third line is used to feed nitrogen coming from a liquid nitrogen tank outside the building.

The third line is connected with the reactants ones in order to feed nitrogen through the reactants lines to ensure high flow of N_2 during the preheating and the shut-down procedure.

The gas cylinders are equipped with pressure reducers, which allow to decompress the gas from the storage pressure (200 bar) to the operating pressure (3 bar). Each feed line consists of:

- intercept valve (placed at the beginning of the feed line) on the low pressure line coming from the gas cylinder;
- Bourdon pressure gauge (with a full scale of 6 bar);
- rotameter (only for CH_4/C_3H_8 and air lines) which allows to have an immediate evaluation of the flow in every line;
- metallic mesh filter to protect instrumentation from gas impurities;
- Digital mass flow controllers (DMFC);
- Bourdon pressure gauge;
- intercept valve.

The digital mass flow controllers are of 5850S type of Brooks Instruments with maximum flow equal to:

- 15 $Nlmin^{-1}$ calibrated on methane and propane;
- 30 $Nlmin^{-1}$ calibrated on air;
- 15 $Nlmin^{-1}$ calibrated on nitrogen.

The mass flow controllers of fuel and air are connected to PC and controlled via Brook Smart Control software. For every mass flow control a calibrated line has been obtained measuring the volumetric flow of the gas, through bubble flowmeter, at increasing the set pioint of DMFC opening. The slope and the intercept of the calibrated line are obtained by linear regression of experimental data. An example of calibrated line is reported in Figure 2.3.

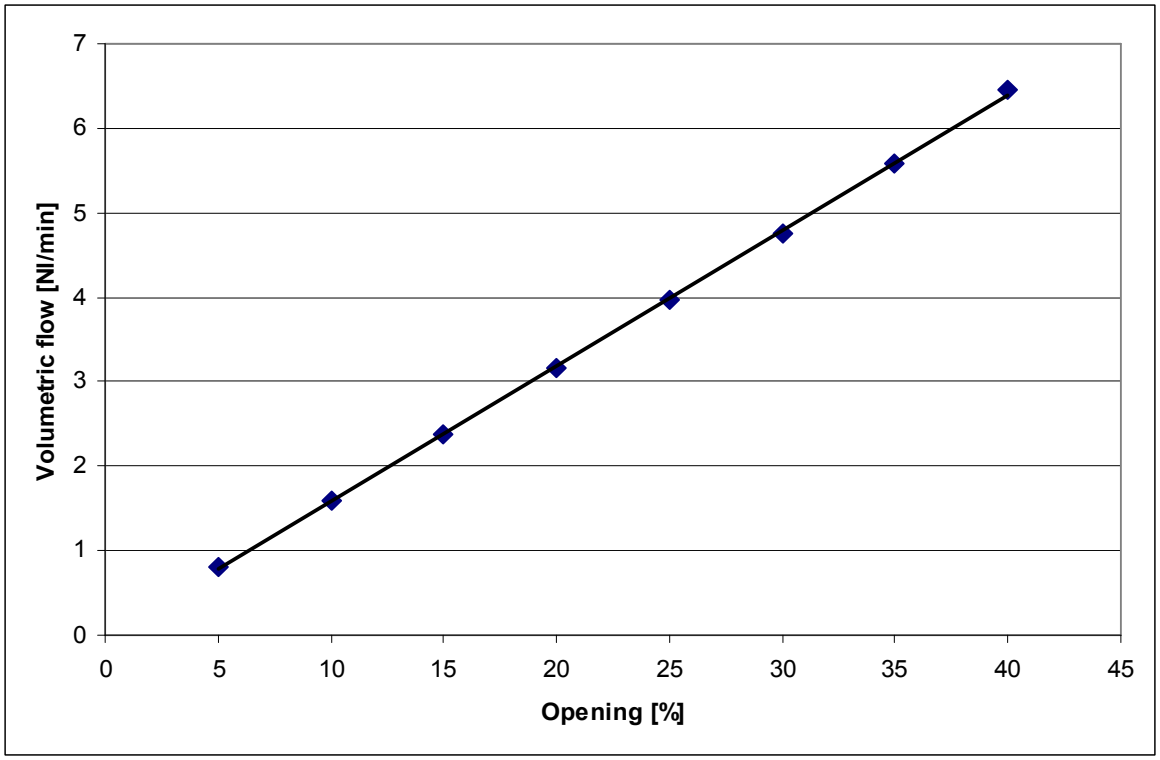

Figure 2.3: Calibrated line for DMFC of methane.

The feeding section is also equipped with a separated preheating system of the reactants flows for safety reasons. Air is preheated in two Watlow® Starflow cartridge heaters, which have the maximum temperature of electrical resistance of 650°C and 800°C respectively. In the diluted test also nitrogen is preheated by the two cartridge heaters because air and nitrogen lines are connected before the preheating system. The fuel (methane or propane) is preheated in an electrical oven divided in three zones, with three independent temperature controllers connected to thermocouples. In order to limit heat dispersion every line is thermally insulated with a thick layer of quartz wool and then with a tape based on glass wool. After the preheating system, the reactants are mixed in a Sulzer® static mixer, placed just upstream the reactor.

2.3 REACTOR

The reaction section is composed by the pilot-scale adiabatic reformer which can process higher flows than those fed in a normal lab-scale rig. The reactor is a quartz tube in order to prevent coke formation and it can be isolated through a by-pass line and two intercept valves. The quartz tube has a length of 11.3 cm, an inner diameter of 2.5 cm and an outer diameter of 2.9 cm. It is inserted in a stainless steel cylinder which allows the connection with the feed lines and thermal insulation is obtained by wrapping the reactor with a very thick layer of quartz wool taping.

Inside the quartz tube there is the catalytic bed which is Rh/α-Al_2O_3 supported on 400 CPSI cordierite honeycomb monolith. Cordierite is a ceramic material ($2MgO{\cdot}2Al_2O_3{\cdot}5SiO_2$), which is considered a good support because it does not interact with the washcoat layer, it has low coefficient of thermal expansion and high thermal stability due to high melting point (1450 °C). The active phase was also supported on 115 CPSI silicon carbide honeycomb monolith. Silicon carbide (SiC) is considered a good support because it is chemically inert as it has a good resistance to oxidation and a high melting point (2730 °C). Moreover, high thermal conductivity coupled with low thermal expansion and high strength gives this material exceptional thermal shock resistant qualities.

The internal layout adopted in the CPO tests, afterwards called standard configuration (Figure 2.4), was obtained by a previous optimization study [40] and consists of:

- 3 Fecralloy® foams (total length of about 3.7 cm), acting as flow mixers and front heat shield minimizing axial heat dispersions;
- void space (about 1.5 cm long), it allows to have a good mixing of gas and it prevents the partial occlusion of the channels of the catalytic monolith;
- catalytic monolith (about 1.9 cm long);
- void space (about 1.5 cm long) with the same function of the void before of catalytic bed;
- inert cordierite monolith (about 2 cm long), which has the function of back heat shield.

The quartz tube and all the part inside are wrapt in Dalfratex® tape to prevent by-pass. This material is composed of quartz continuous filaments and it combines the flexibility of the fibrous structure with the refractory propriety of quartz. In fact, this material can resist up to 1000°C continuously and up to 1600°C for limited time periods.

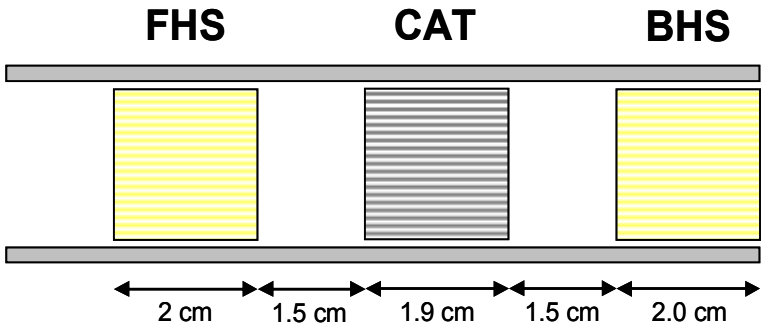

Figure 2.4: Standard configuration.

In this work other configurations were also studied to lower the hot spot temperature in the inlet section. These configurations differ from the standard one for the position of the front heat shield with respect to the catalytic monolith.

The second configuration studied in the same operating conditions, afterwards called continuous FHS (front heat shield) configuration, is composed by (Figure 2.5):

- 3 Fecralloy® foams with total length of about 3.7 cm;
- void space of about 1 cm;
- catalytic monolith (about 3.5 cm long) with a inert zone of about 1 cm, which has the function of front heat shield and is continuous to the catalytic zone, in this way heat dispersion is minimized;
- void space of about 1.5 cm;
- inert cordierite monolith (about 2 cm long).

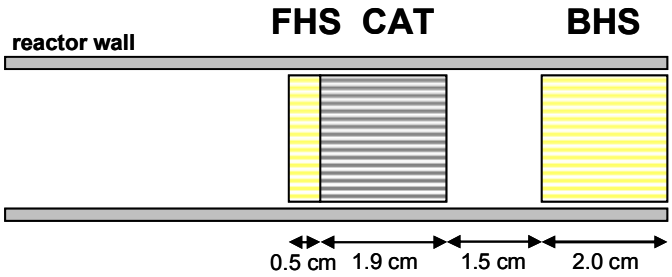

Figure 2.5: Continuous FHS configuration.

The last configuration, afterwards called without FHS configuration, is composed by (Figure 2.6):

- 1 Fecralloy® foam (about 0.9 cm long);
- void of about 4 cm, in this way heat dispersion is maximised because there is not a front heat shield;
- catalytic monolith (about 1.9 cm long);
- void of about 1.5 cm;
- inert cordierite monolith (about 2 cm long).

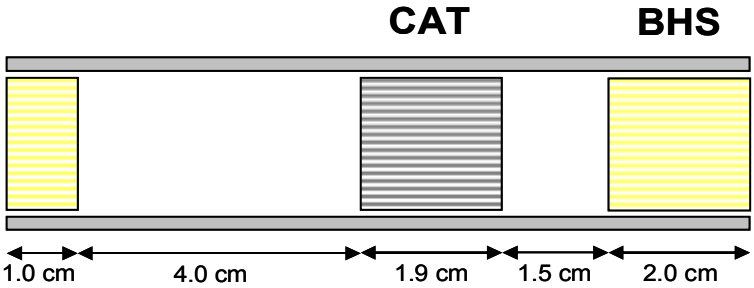

Figure 2.6: Without FHS configuration.

Temperature measurements are acquired by telescopic or capillary thermocouple and their values are automatically recorded by a temperature data recorder of Pico® technology.

Furthermore, for the acquisition of the solid temperature a pyrometer with optical fiber was used. The pyrometer is IGA5-LO model of Impact Mikron Infrared.

The reactor is equipped with several K – type thermocouples as shown in Figure 2.7. The thermocouples are sheathed in Inconel®. Even if Inconel® is composed of about 70% nickel (a very good steam reforming catalyst) the surface area of the thermocouple is so low with respect to the total gas flow that any catalytic interaction between the reactant gases and the thermocouple sheath can be ignored. One of these thermocouples is placed in a steel sheath and it measures the radial inlet gas temperature at about 7 cm from the inlet section of reactor. The telescopic thermocouple is placed downstream of the reactor (Back TC) and can slide in a central channel of the monolith measuring the axial temperature profile. Other thermocouples are placed in the cartridge heaters and in the by-pass line.

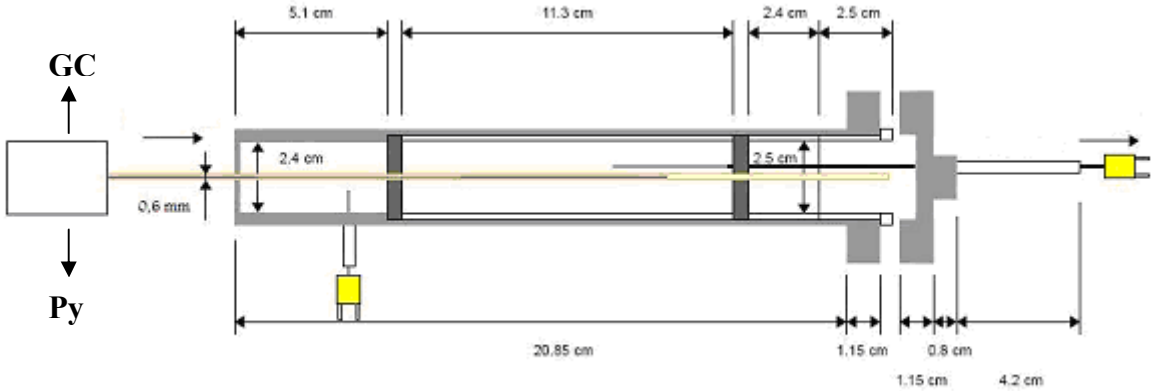

Figure 2.7: Reactor diagram.

At the inlet the reactor has a spatial sampling device for the species and temperature measurements. This spatial sampling device consisted of fused silica capillary having a polyimide coating on the outside that made the capillary flexible for handling but burned off quickly during the first use. The fused silica capillary serves as duct to sample species into gas chromatograph or as an access point for thermocouple or fiber optic to measure the temperature. Silica fused capillary has similar thermal proprieties as alumina which serves to minimize axial conduction which may result from non-similar thermal proprieties. The capillary can also withstand temperatures in excess of 1200 making it a robust probe in this high temperature reactor. Furthermore fused silica is essentially transparent to radiation and its low surface area and poor catalytic proprieties minimize the capillary's impact in the reactor system. The fused silica capillary is insert in the axial hole of the foams (Figure 2.8) and in the central channel of the catalytic monolith.

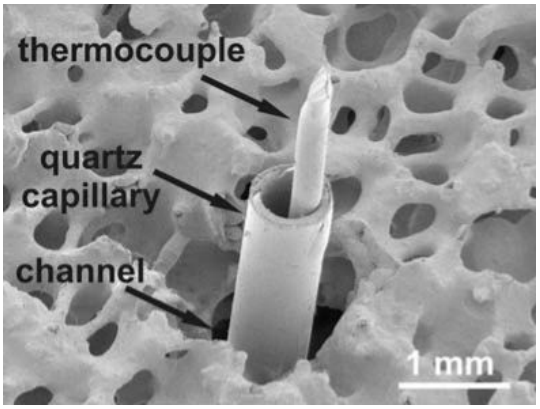

Figure 2.8: SEM micrograph showing sampling capillary and thermocouple in a 80 ppi foam.

The sampling capillary exits the reactor by passing through a capillary port, a small stainless steel tube, which enters the head of the reactor through a septum. The lower end of the capillary is connected to a ported micro-volume tee (1/16, 75 mm bore, ss). The opposite port can be used to insert the thermocouple or the fiber optic into the capillary if in the test the temperature profiles are measured. Otherwise in the tests of measurement of the composition profiles the opposite port is connected to a stainless steal capillary (with 1/16 nominal diameter) that discharges the gas into the micro-gas chromatogram. A pump generates a vacuum at the end of the stainless steel capillary, forcing the gases from the sampling orifice into the micro-gas chromatogram. The tee is mounted on a liner actuator Zaber TLA-16, controlled from PC. In this way the capillary can be moved up and down with a sub-mm resolution. The capillary is used as an inert sleeve thin capillary thermocouple or an optical fiber connected with the pyrometer. Otherwise the same capillary is connected to the micro-gas chromatograph in order to measure the concentration of reactants and products. This system is used to collect spatially resolved temperature and concentration profile along the axis of the reactor and the temperature probe and composition will be described in details in Chapter 4.

In figure 2.9 a typical scheme of axial sampling system, reported in literature, shows the interface with the reactor and vacuum system to collect spatially-resolved temperature and species data.

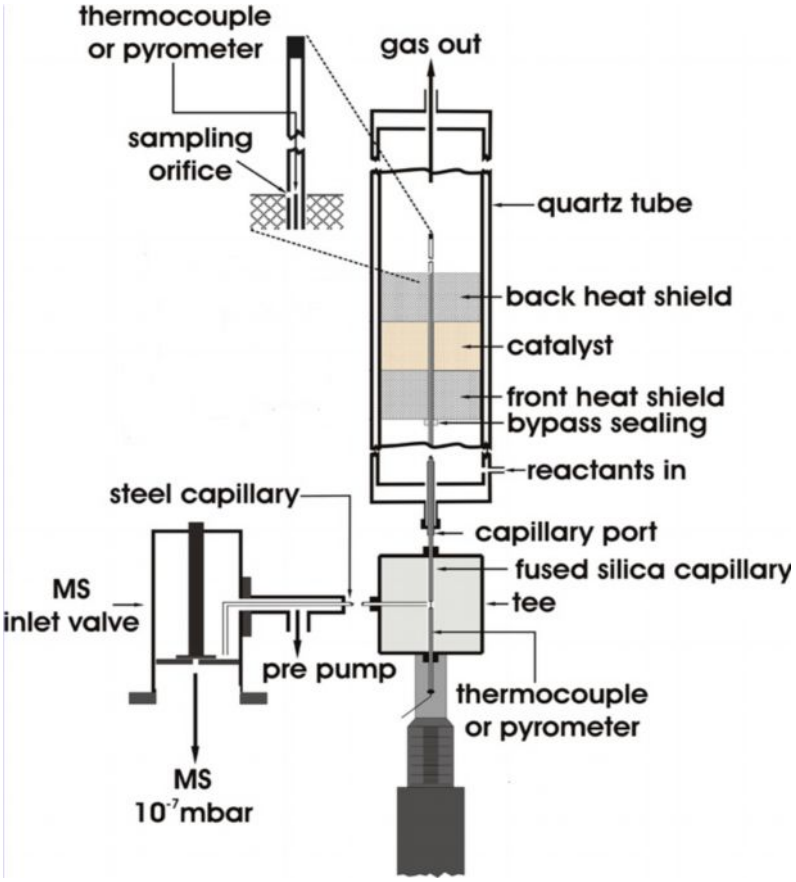

Figure 2.9: Reactor setup and capillary sampling system.

In order to verify how close to the adiabatic condition the reactor operated, the thermal efficiency was defined as the ratio between the experimental temperature rise and the adiabatic temperature rise of the gas phase, according to the following equation:

$$\alpha = \frac{T_{EXP}^{OUT} - T_{EXP}^{IN}}{T_{ADIABATIC}^{OUT} - T_{EXP}^{IN}} \tag{2.1}$$

Where T_{EXP}^{IN} is the inlet gas temperature, T_{EXP}^{OUT} is the outlet gas temperature and $T_{ADIABATIC}^{OUT}$ is the adiabatic temperature, calculated at the composition of the outlet gas mixture.

In this work CPO tests were also carried out in a quartz reactor connecting the feed lines directly to the reactor without the use of stainless steel cylinder. The quartz tube has been thermally insulated by a thick layer of glass wool. These experiments were perfomed in order to verify how much the thermal behaviour of the reactor is influenced by the presence of the stainless steel cylinder, which is a conductive material. In this case, because of the configuration, the back thermocouple was not used and only the capillary is inserted from the inlet section of the reactor and used for measuring the composition and temperature profiles.

2.4 GAS ANALYSIS SECTION

The analysis of the composition of reactants and products mixture can be performed in two different devices depending on the type of analysis. The ABB® AO2000 series instrument is used for continuous analysis and it allows to quantify CH_4, CO, CO_2, O_2 and H_2. A micro-gas chromatograph Agilent 3000 of Agilent Technologies is used for steady-state analysis. In the next paragraphs the micro-gas chromatograph and the continuous gas analyzer will be described in detail.

2.4.1 MICRO-GAS CHROMATHOGRAPH

A micro-gas chromatograph is characterized by lower volume and time of analysis than those of a traditional gas chromatograph. The instrument used in this work has two columns both using argon as carrier gas:

- molecular sieves (5Å) to separate H_2, O_2, N_2, CH_4, CO;
- Plot Q to separate CH_4, CO_2, C_2H_4, C_2H_6, H_2O, C_3H_6, C_3H_8.

The carrier gas, stored in gas cylinders outside laboratory, are used at 5.5 bar as imposed by constructor to ensure correct working of pneumatic parts, which used carrier gas as instrumental gas. Besides the carrier gas must not have impurities so that analysis is not modified and at the same time high purity gases results in better sensitivity and longer column life. For these reasons, the line of carrier gas has set up a filter (2µm) to absorb dust and an O_2 trap because concentration of oxygen should be below 1-2 ppm.

The characteristics and the working conditions of the two columns are reported in Table 2.1

	Molecular sieves (5Å)	Plot Q
Type of column	capillary	capillary
Length [m]	10	8
Diameter [mm]	0.32	0.32
Temperature [°C]	90	70
Injector temperature [°C]	100	100
Pressure [psi]	30	22
Injection time [ms]	400	40
Analysis time [s]	180/360	180/360

Table 2.1: Characteristic and working conditions of Micro-GC column.

The analysis time is 180 s in methane/air experiments, while 360 s for propane/air tests. This difference is due to different retention times of gas species.

The components of the mixture are separated by the columns of micro-gas chromatograph and analyzed with a thermal conductivity detector (TCD). The TCD is used to measure the thermal conductivity which depends upon the composition of the gas mixture. The TCD consists of four tungsten-rhenium filaments in a Wheatstone bridge as shown in Figure 2.10.

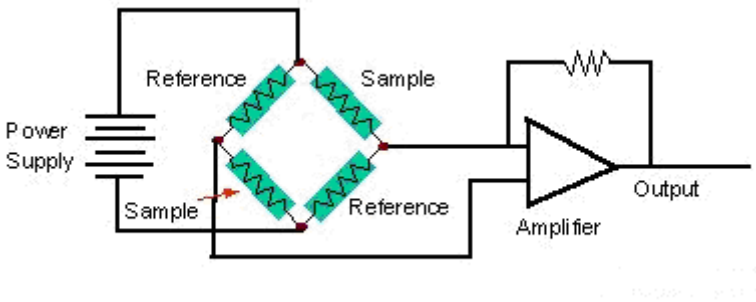

Figure 2.10: Wheatstone bridge for TCD detection.

Electric current flows through the four filament causing them to heat up. Carrier gas flows across the filament removing the heat at a constant rate. When a sample molecule (with different thermal conductivity) exits from the column and flows across the two sample filaments, the temperature of the filaments increase unbalancing the Wheatstone bridge and generating a peak as the sample molecules transit through the detector. The voltage signal produced is proportional to the difference in the thermal conductivity between the column effluent flow (sample components in carrier gas) and the reference flow of the carrier gas alone. The voltage signal produced is proportional to the number of molecules passing through the detector at any given time. If the voltage signal (μV) produced by the detector TCD is plotted as function of the time, a chromatogram will be obtained. In the chromatogram each peak corresponds to a separate component which is characterized by a retention time. So for well-separated peaks, the total number of molecules of each component is proportional to the area under the peak. To convert the peak area to the concentration of the species, the peaks must be calibrated. In fact only in this way it is possible to quantify the chromatographic data. There are different types of quantification methods. In this work the internal standard method was used introducing the response factor of reference species. According to this method, the inlet and outlet flow rate of the reference species must be known, so in this case nitrogen was chosen because it is an inert.

The response factor of a generic species is defined as:

$$\alpha_i = \frac{Q_i / Q_{N_2}}{A_i / A_{N_2}} \tag{2.2}$$

where:

- Q_i, Q_{N2} are the volumetric flow rate of i-species and N_2;
- A_i, A_{N2} are the peak area of i- species and N_2.

The response factor of nitrogen is defined equal to the unity.

The Plot Q column does not separate N_2, in fact in the chromatogram there is a unique peak for N_2, O_2, CO and H_2. On the opposite, the molecular sieves column can separate these four species and so it is possible to calculate the relative ratio between the four species and to identify the fraction of the peak area corresponding to nitrogen in Plot Q column. The response factors of the species separated by Plot Q column are related to this pseudo N_2 peak.

The response factors of each species are experimentally obtained through analysis of a calibrated mixture. Table 2.2 reports retention time and response factor of each species.

Species	Column	Retention time [min]	α_i
H_2	molecular sieves	0.500	0.08686
O_2	molecular sieves	0.618	0.82978
N_2	molecular sieves	0.754	1.00000
CH_4	molecular sieves	1.048	0.41256
CO	molecular sieves	1.387	1.06252
Air+CO+H_2	Plot Q	0.885	-
CH_4	Plot Q	0.950	0.41256
CO_2	Plot Q	1.101	2.14396
C_2H_4	Plot Q	1.250	0.92600
C_2H_6	Plot Q	1.321	0.87300
H_2O	Plot Q	2.253	0.35785
C_3H_6	Plot Q	4.157	0.79200
C_3H_8	Plot Q	4.851	0.92946

Table 2.2: Micro-GC calibration with retention time and response factor of the different species.

2.4.1.1 DATA ELEBORATION

The results of gas chromatograph analysis are two chromatograms obtained by molecular sieves and Plot Q column respectively. An example of chromatograms is shown in Figure 2.11.

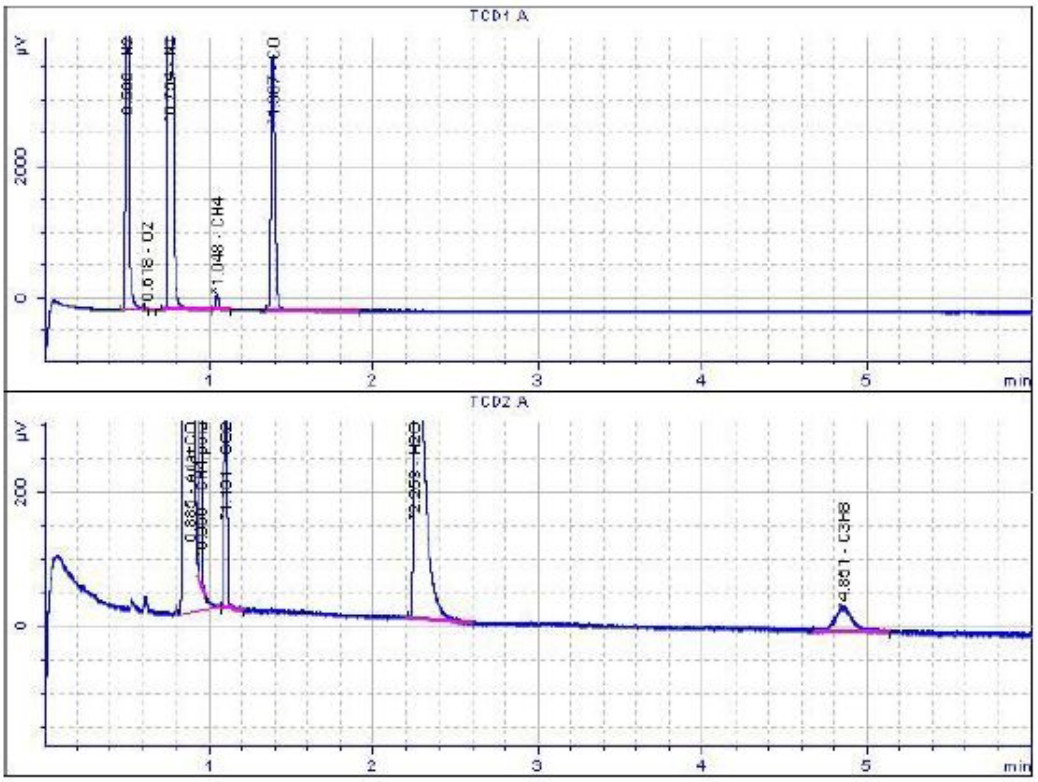

Figure 2.11: Example of gas chromatogram.

Thanks to the micro-GC software it is possible to integrate the area of each peak. Once the area of each peak is calculated, it is possible to obtain the volumetric flow of each component through the response factors and the volumetric flow of nitrogen, as follows (2.3):

$$Q_i = \alpha_i \cdot Q_{N2} \cdot \frac{A_i}{A_{N_2}} \tag{2.3}$$

The molar flows for every species are calculated according to the following correlation (2.4):

$$F_i = \frac{Q_i}{0.022414} \tag{2.4}$$

Then, the molar fractions of every species are calculated (2.5):

$$y_i = \frac{F_i}{\sum_i F_i} \tag{2.5}$$

Once molar fraction of each species is determined, it is possible to calculate the reactants conversions and the selectivity to hydrogen and carbon:

$$\chi = 1 - \frac{F_{C3H8}^{OUT}}{F_{C3H8}^{IN}} \tag{2.6}$$

$$\chi = 1 - \frac{F_{O2}^{OUT}}{F_{O2}^{IN}} \tag{2.7}$$

$$Sel_C = \frac{F_i^{OUT} \cdot nC_i \cdot 100}{FC_{converted}} \tag{2.8}$$

$$Sel_H = \frac{F_i^{OUT} \cdot nH_i \cdot 100}{FH_{converted}} \tag{2.9}$$

In order to check the accuracy of the analyses the atomic balance of carbon, hydrogen and oxygen are defined as follows:

$$BC = \frac{\sum_i F_i \cdot nC_i}{FC_{converted}} \tag{2.10}$$

$$BH = \frac{\sum_i F_i \cdot nH_i}{FH_{converted}} \tag{2.11}$$

$$BO = \frac{\sum_i F_i \cdot nO_i}{FO_{converted}} \tag{2.12}$$

Where:

- nC_i is the number of carbon atoms of the i-species;
- nH_i is the number of hydrogen atoms of the i-species;
- nO_i is the number of oxygen atoms of the i-species;
- $FC_{converted}$ is the molar flow of converted carbon atoms;
- $FH_{converted}$ is the molar flow of converted hydrogen atoms;
- $FC_{converted}$ is the molar flow of converted oxygen atoms.

Every balance is defined as ratio between the carbon, hydrogen, oxygen atoms present in the outlet mixture and the converted carbon, hydrogen, oxygen atoms. The balance must be equal to 1 because a balance over the unity indicates an overestimation of the products, on the other hand a balance under the unity indicates an overestimation of the conversion.

In the experiments the error was less than 5%, except in the tests of sampling of the axial composition profile where the hydrogen balance closed to < 8%. In same tests water was calculated by closing the oxygen mass balance to 1.

2.4.2 CONTINUOUS GAS ANALYZER ABB

The mixture is sucked by a membrane pump with a flow rate of about 60 l $h^{-1}$and an overpressure of 0.05 bar, which are necessary conditions for the optimal working of the analysis modules. Upstream the analyzer, the mixture is dehumidified by a condenser and dried through specific filter because water damages the instrument. Then the mixture is sent to the gas analyzer (Figure 2.12). The output signal is the volumetric concentration of the anhydrous mixture.

Figure 2.12: Continuous gas analyzer.

At the beginning of every week the instrument was manually calibrated using three different span gases coming from high pressure cylinder:

- Span 1: mixture of H_2 in N_2 at 20.34%;
- Span 2: mixture of CO_2, CO, CH_4 in N_2 respectively at 16.09%, 23.97% and 24.01%;
- Span 3: mixture of O_2 in N_2 at 20.96%;
- Zero gas: nitrogen of line.

The continuous gas analyzer is composed by three different modules connected in series:

- *Uras 14* (Infrared Photometer) for the analysis of CH_4, CO and CO_2 ;
- *Magnos 106* (Magneto-mechanical) for the analysis of O_2;
- *Caldos 17* (Thermal conductivity-Silicon sensor) for the analysis of H_2.

- **<u>Module Uras 14</u>**

Uras 14 is a NDIR (non-dispersive infrared) process photometer that measures up to four components simultaneously and continuously. The measurement principle is based on the capacity of the molecules to absorb specifically the radiation in the medium infrared

between 2 μm and 12 μm. In fact, each molecule absorbs infrared light at wavelengths representative of the types of present bonds. The amount of absorbed IR light is proportional to concentration of the molecules, in accordance with the Lambert-Beer law:

$$A = \varepsilon \cdot \ell \cdot c \tag{2.13}$$

$$I = I_o \cdot 10^{-A} \tag{2.14}$$

where I_o is the initial light intensity emitted from the infrared lamp (measured in pure air), I is the intensity of light reaching the end the detector (with sample gas present), A is the absorbance in units of length^{-1}, l is the path length, ε is the molar extinction coefficient in concentration $^{-1}$and length^{-1} and c is the concentration.
The energy absorbed by molecules is converted in kinetic energy, causing the molecules to speed up and thus heat the gas.

The Uras 14 module is composed by (Figure 2.13):

- infrared lamp;
- chopper wheel;
- sample cell;
- calibration cell;
- opto-pneumatic detector.

During the measurement the heating coil generates an infrared radiation which passes through a chopper wheel, so that background signal can be off set from the desired signal, and then in a filter. Then the infrared beam is directed alternately through the two parallel optical cells, sample cell and calibration cell. The calibration cell continuously contains a reference gas, in this case nitrogen, so that a reference signal is supplied. Before the detector there is another filter to eliminate all light except the wavelength that the selected gas molecules can absorb. In this way the other gas molecules, do not adsorb light at this wavelength, do not affect the amount of light reaching the detector. In the opto-pneumatic detector, containing the sample gas, the radiant energy absorbed by the fill gas causes a change in temperature and thereby a change in the pressure in the detector. This change in pressure evokes an electrical signal via membrane capacitor.

In this work the module Uras 14 is used for measuring of CO, CH_4 and CO_2 and their concentration is determined connecting the detectors in series.

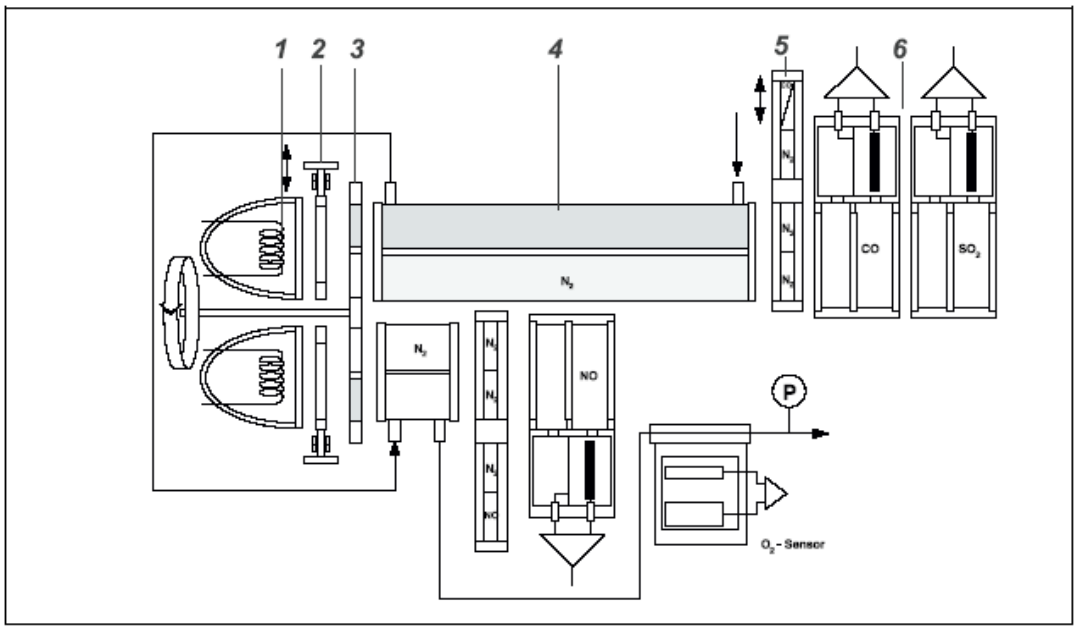

1 Emitter
2 Aperture
3 Chopper wheel
4 Sample cell
5 Adjusting unit / Calibration cell
6 Receiver

Figure 2.13: Schematic representation of module Uras 14.

- **Module Caldos 17**

In the Caldos 17 module the principle of measurement is based on the different thermal conductivity between gases. The module is composed by (Figure 2.14):

- thermostatic chamber;
- support with flange and sample chamber with electronic sensor to measure the temperature;
- thermal conductivity sensor;
- heater;
- thermal connections;
- plug connections.

The thermal conductivity sensor is a micromechanical-made silicon chip with thin-film resistors and a membrane which separated hydrogen from the analyzer flow. In this way the flow does not influence the measurement. The sensor is located in a thermostatically-controlled stainless steel enclosure with a temperature of 60°C in order to prevent any influence of ambient temperature alterations. Besides, the sensor is not place in the main flow to prevent the influences by sample gas changes.

Silicon based sensor are used because this material allows a rapid measurement and extremely small measuring ranges.

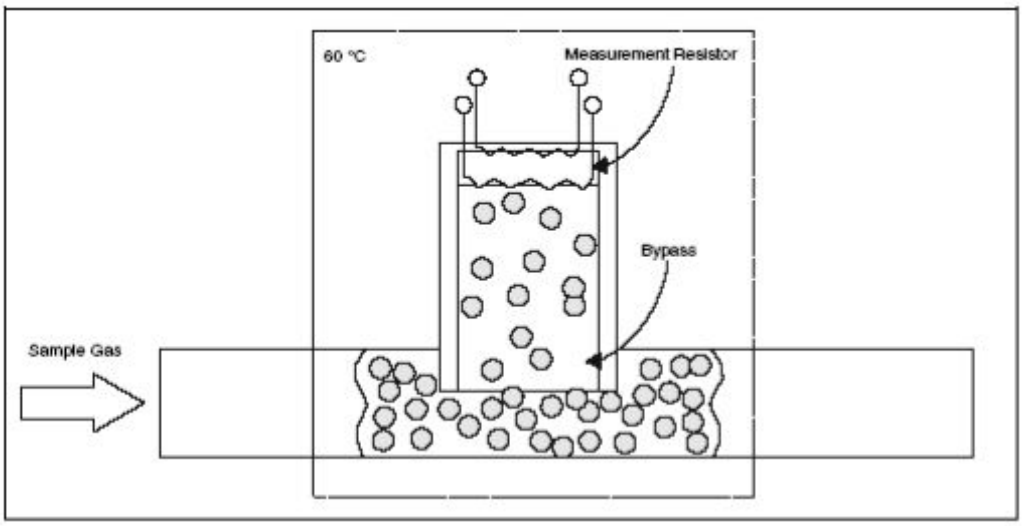

Figure 2.14: Schematic representation of module Caldos 17.

- **Module Magnos 106**

The measuring principle of the Magnos 106 is based on the paramagnetic propriety of oxygen. In fact oxygen has a relatively high magnetic susceptibility as compared to other gases such as nitrogen, helium, argon, etc. and exhibits a paramagnetic behaviour.

The Magnos 106 module (Figure 2.15) is composed by:

- thermostatic chamber;
- thermal connections;
- permanent magnet;
- flow control;
- temperature indicator and control;
- plug connection.

The paramagnetic sensor consists of a cylindrical shaped container inside of which is placed a small glass dumbbell. The dumbbell is filled with inert nitrogen and suspended on a taut platinum wire within a non-uniform magnetic field generated by a strong permanent magnet mounted outside the camber. The dumbbell is design to move freely as it is suspended from the wire. When a sample gas containing oxygen is processed through the sensor, the oxygen molecules are attracted to the stronger of the two magnetic fields. This causes a displacement of the dumbbell which results in the dumbbell rotating. Then a precision optical system measures the degree of rotation of the dumbbell. In this system a light source photodiode generates a beam which a mirror, placed on the dumbbell, deflects onto the photodector, resulting in the generation of an electronic signal. The signal current is amplified and fed back to a conducting coil at the dumbbell. In this way an opposite current is applied to restore the dumbbell to its normal position. The current required to maintain the dumbbell in its normal state is directly proportional to the partial pressure of

oxygen. The measurement module is placed in a thermostatic chamber in order to prevent the influences of ambient temperature changes. This paramagnetic sensor offers excellent accuracy over a range of 1% to 100% oxygen.

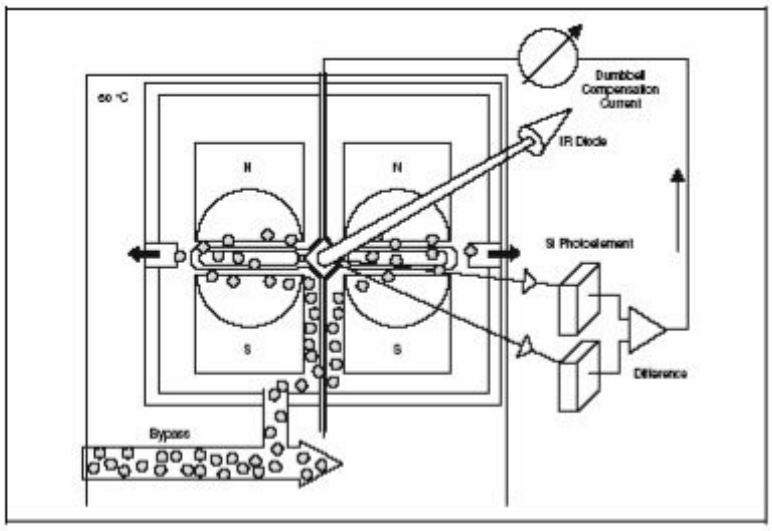

Figure 2.15: Schematic representation of module Magnos 106.

2.5 EXPERIMENTAL PROCEDURES

2.5.1 START-UP PROCEDURE AND CPO TESTS

The first operation is the switching on of the fume hood to remove the exhaust gases. Then the gas cylinders of carrier and reactants are opened. The pressure of the reactant and carrier gases is adjusted to 3 bar and 5.5 bar respectively.
Subsequently, the mass flow controllers are activated via PC and the percentage opening is adjusted to the desired set-point. Then the micro-gas chromatograph is turned on and set to analysis method conditions.

At this point, the preheating procedure starts. The three zones of the electrical oven are set to 400°C, the two cartridge heaters, whose maximum working temperatures are 650 °C and 800 °C, are set to 440°C and 560 °C, respectively. Such set points are able to reach a sufficiently high inlet gas temperature for the light-off at standard flow rate. In the case of propane experiments the three zones of the oven are set to 300°C to prevent cracking of propane inside the heating coil. Moreover, to prevent the water condensation, through heating socks, the lines downstream of the reactor are heated at 110°C.
The start-up procedure is different depending on total flow rate of the reactants. In the first method, called cold-start, the reactants (previously preheated) are fed at zero time to the reactor which is at room temperature. During the preheating, the valve are arranged to feed fuel and air in the preheating section, while the valve downstream the reactor is closed and the valve of by-pass is opened. In this way the reactor is kept at room temperature.

When the temperature on the by-pass line reaches its stationary value, the preheated reactant mixture is fed to the cold reactor by closing the by-pass line and opening the reactor line. However, this procedure can be used only when the flow rate of reactants is sufficiently high to reach an inlet temperature for the light-off of the reaction (about 350°C). It was experimentally observed that with the set-points above described, only a total flow rate higher than 15 Nl min^{-1} guarantees such condition. In the case of lower reactants flow rate, a start-up procedure with preheated catalytic bed is needed. In this method the valves are arranged so that a high flow of nitrogen (usually 21 Nl min^{-1}) can be fed to the reactor which is preheated. When the temperature of the catalytic bed reaches about 350°C, the reactants lines are opened and the light-off immediately occurs.

After reaching stationary conditions (about 90 minutes after the light-off), temperature and concentration profiles along the axis of the catalytic monolith are collected through a spatially resolved sampling technique, which will be described in detail in Chapter 4.

Once the light-off has occurred it is also possible to study the performances of the reformer in autothermal conditions, without external heat input. In this case the valves are arranged to by-pass the electrical oven and the two cartridge heaters and the reactants are fed to the reactor at room temperature. After steady state conditions are reached, temperature or composition axial profiles are sampled as explained in the preheated experiments.

At the end of each test, the reactant mixture is analysed with the micro-GC closing the valve downstream the reactor and opening the valve of by-pass line.

2.5.2 SHUT-DOWN PROCEDURE

At the end of each experiments, the reaction is turn off with a cold flow of nitrogen, then it is continuously fed to the reactor to cool it down.

At the end of every day the lines and the cells of the countinuous gas analyzer are purged with a nitrogen flow and the shut-down method for the micro-GC is activated from the PC. Once the columns temperature is below 50°C, the micro-GC can be turned-off. Finally, the intercept valves and gas cylinder are closed.

2.5.3 OPERATING CONDITIONS

In this work CH_4 CPO tests were first performed in the following operating conditions:

- total flow rate from 10 to 20 $Nlmin^{-1}$;
- CH_4/Air feeding mixture corresponding to 27.3 % CH_4, 15.3 % O_2, 57.4% N_2;
- atmospheric pressure.

Subsequently propane/air mixtures were investigated in this operating conditions:

- total flow rate from 5 to 10 $Nlmin^{-1}$;
- C_3H_8 concentration from 3.33% to 11%;

- atmospheric pressure.

Both CH_4 and C_3H_8 experiments were carried out in preheating and autothermal conditions, at a slightly overstoichiometric O_2/C ratio, equal to 0.56 to prevent carbon formation.

2.6 CATALYST PREPARATION

The preparation of catalytic honeycomb monoliths (Figure 2.16) is characterized by different subsequent steps: preparation of α-Al_2O_3 and of the catalytic powder, preparation of the catalytic slurry and finally the coating onto the primary support.

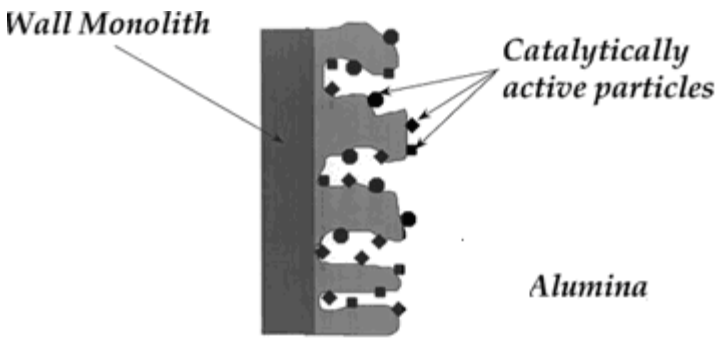

Figure 2.16: Catalytic monolith.

The preparation of catalytic honeycomb monoliths is characterized by different subsequent steps: preparation of α-Al_2O_3 and of the catalytic powder, preparation of the catalytic slurry and finally the coating onto the primary support.

2.6.1 CATALYTIC POWDERS

α-Al_2O_3 (5-10 m^2/g) was used as thermally stable support. It was obtained by calcination in stagnant air at 1100 °C for 10 hours of commercial alumina (Sasol®, PURALOX Sba-200) which is mainly composed by γ-Al_2O_3 (96.9%). The calcination temperature was reached through a temperature ramp with a rate of 1°C/min. At the end of the hold time the sample was cooled down to room temperature with a rate of 2 °C/min. In fact at 1100°C the transition of the alumina phase from γ to θ and then to α was complete.

The catalytic powders were prepared by incipient wetness impregnation of the α-Al_2O_3 support with a precursor of the active phase. This precursor is $Rh(NO_3)_3$ in aqueous solution at 14.68% w/w (Chempur®) and with a density of 1.62 g/ml. The technique consists in impregnating the α-Al_2O_3 powder with a solution (stock solution) of a

thermolabile precursor of rhodium ($Rh(NO_3)_3$) and a sufficiently volatile solvent (water). According to this technique, the impregnating volume (V_t) must be equal to the total volume of the pores of the support (V_p) so that the porous volume is completely filled. The volume of stock solution to fill the volume of pores is calculated from the mass of catalytic powders:

$$V_t = V_p \cdot g_{dust} \tag{2.15}$$

To prepare a solution containing the required load of rhodium, it is necessary to calculate the ml of precursor solution:

$$grammes_{Rh} = \frac{load_{Rh} \cdot g_{dust}}{1 - load_{Rh}} \tag{2.16}$$

$$ml_{solutionRh(NO_3)_3} = \frac{grammes_{Rh}}{density_{solutionRh(NO_3)_3} \cdot \omega_{Rh}} \tag{2.17}$$

where ω_{Rh} is the massive fraction of $Rh(NO_3)_3$.

The quantity of precursor has to be diluted up to the volume of solution needed to fill the pores completely (V_t). Since volumetric flask are available in fixed sizes, the solution is diluted in a volumetric flask of 5 ml. The dilution ratio is defined as the ratio between the volume of solution necessary to fill completely the pores and the volume of precursor containing the required mass of rhodium:

$$R = \frac{V_t}{ml_{solutionRh(NO_3)_3}} \tag{2.18}$$

In order to prepare 5 ml of solution containing the correct mass of rhodium it is necessary to take a quantity of precursor given by the ratio between 5 ml of solution and the value of R. In this way 5 ml of stock solution are obtained.
From the stock solution, a required volume to fill the pores of support is sampled and this quantity is dripped onto the alumina powder through a buret until incipient impregnation. The small Rh quantity to deposit allows to impregnate just once. The catalytic powders are then dried at 110 °C for 3 hours. During this p the precursor is deposited inside the pores because of evaporation of the solvent.

2.6.2 SLURRY PREPARATION

The catalytic powder is mixed with water and nitric acid on the basis of a standard recipe studied in a previous work [41]. The recipe is defined as follows:

- 1.4 moles of HNO_3 per g of catalytic powder
- 1.7 ml of water per g of catalytic powder
- a number of ZrO_2 spheres so that their total weight is eight time the weight of catalytic powder.

The suspension of catalytic powder, water and nitric acid is ball milled at 51 RPM for 24 hours. The ball milling equipment (Figure 2.17) consists in a PET container (containing the slurry and ZrO_2 spheres) placed inside a ceramic jar at an inclination between 30° and 45° as compared to the horizontal axis. This position is obtained by filling the void space of ceramic jar with voluminous material. Then the jar is positioned on rotary rollers for 24 hours. During this treatment the catalytic powders are reduced in smaller particle through the chemical action of the acid. In this way the formation of agglomerates, which can precipitate, is prevented. Besides, there is also a mechanical action of the spheres of ZrO_2, which mill the catalytic particles.

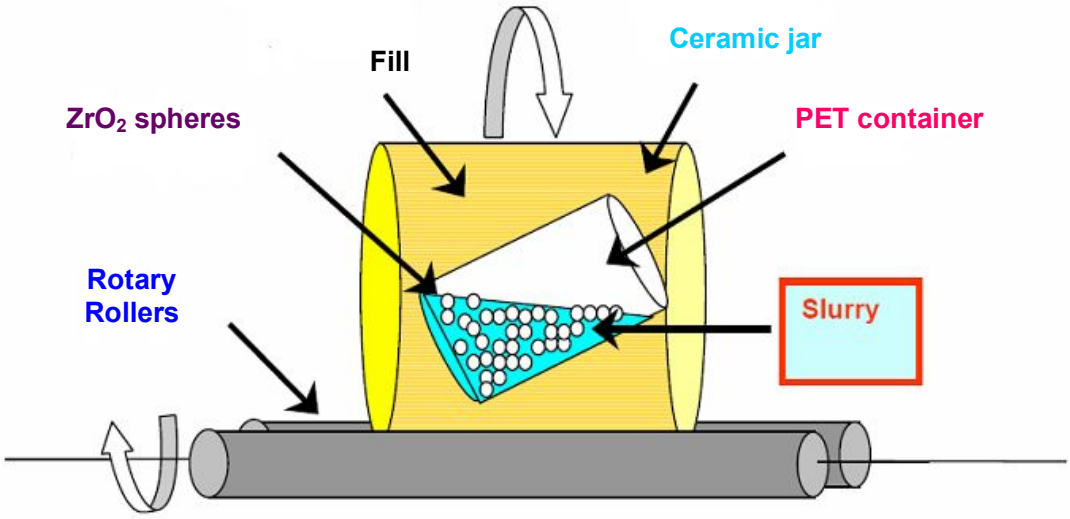

Figure 2.17: Ball milling technique.

2.6.3 MONOLITH COATING

Once the slurry is obtained, it must be deposited on honeycomb monoliths which have a cylinder shape with a length of 2-3 cm and a diameter of 2.4 cm. Before starting the coating procedure the primary supports are washed with acetone to remove the superficial impurities due to handling. Then the lateral surface of the monoliths is covered by Teflon. Then a bohemite primer is deposited. The bohemite primer is prepared by dispersing 10% (w/w) of a commercial aluminium hydroxide powder (Disperal®, Condea Chemie) in a 0.4%(w/w) HNO_3 aqueous solution. After mixing for 10 min, a stable dispersion of bohemite was obtained. For the primer deposition, the supports were dipped in the bohemite dispersion and dried at room temperature for 30 min. This results in the

formation of a well adherent layer on the surface of supports, which improves the adherence of the washcoat layer [42]. The weight of the primer is obtained by the difference between the weight of the monolith before and after the pre-coating with the primer. After the pre-coating with the bohemite primer, the supports were dipped in the catalytic slurry. The level of the catalytic slurry is equal half length of the monolith. So during this phase the channels of the monolith are filled with the slurry because of capillarity. As indicated in Figure 2.18, the excess of the slurry is blown out of the monolith channels with air flow at 8 bar resulting in a homogeneous catalytic layer.

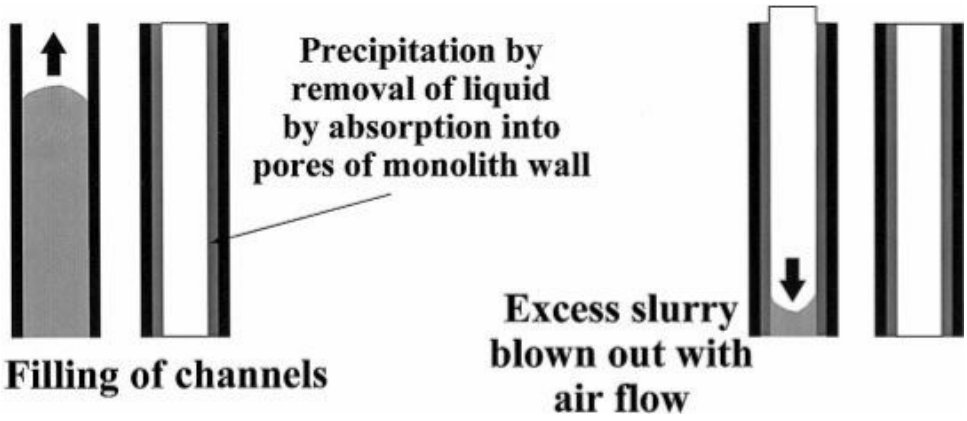

Figure 2.18: Application of suspension of secondary support onto walls on monolith channels.

The coated samples were "flash" dried at 280°C for 5-10 minutes in a ventilated oven so the catalytic layer is fixed to the support. After the flash drying, the weight of the catalytic layer is evaluated by the difference with weight of the monolith with the primer. In Table 2.3 the main characteristics of the catalysts used in this work are reported.

	Sample 1	Sample 2	Sample 3	Sample 4	Sample 5
Primary support	cordierite	cordierite	cordierite	cordierite	SiC
CPSI	400	400	400	400	115
Length [cm]	2.25	1.5	1.5	1.9	2
Diameter [cm]	2.45	2.4	2.4	2.4	2.3
Catalyst density [g cm^{-3}]	1.38	1.38	1.38	1.38	1.38
Load [mg]	242	720	935	257	1485
Thickness [μm]	6.14	29	43	8	101
Void grade	0.72	0.66	0.63	0.72	0.51

Table 2.3: Propriety of the catalytic monoliths tested.

In this work catalytic honeycomb monolith with a continuous inert part were also prepared (Figure 2.19). To obtain an inert zone of about 0.5 cm, the monoliths were dipped in the catalytic slurry at a level of about 1 cm and we waited until the desired height was reached.

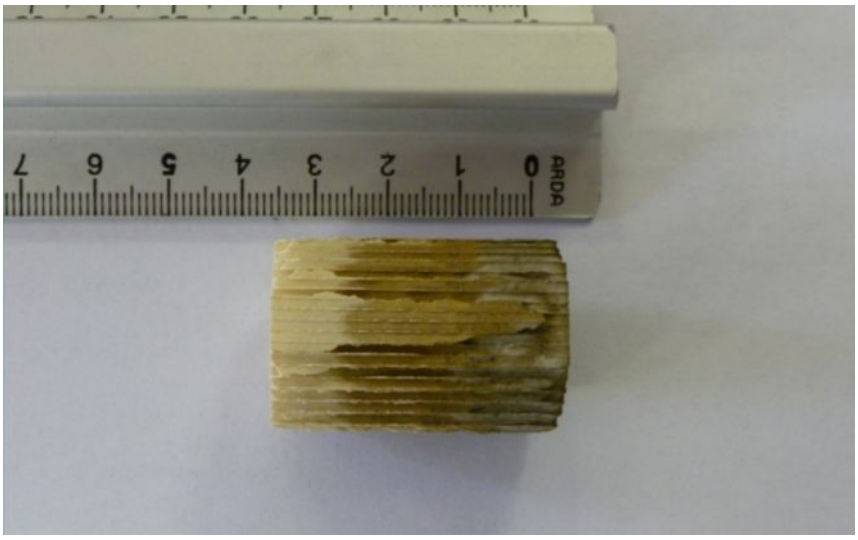

Figure 2.19: Honeycomb monolith with inert zone.

The proprieties of the monoliths with inert zone are reported in Table 2.4.

	Sample 6
Primary support	cordierite
CPSI	400
Length [cm]	3
Length inert zone [cm]	0.5
Diameter [cm]	2.4
Catalyst density [g cm^{-3}]	1.38
Load [mg]	480
Thickness [μm]	12
Void grade	0.7

Table 2.3: Propriety of the catalytic monoliths with inert zone tested.

2.7 CATALYST CHARACTERIZATION

The catalytic samples were characterized with different techniques:

- X-rays diffraction;
- measurement of specific area (BET analysis);
- measurement of porous volume with mercury porosimetry.

2.7.1 X-RAY DIFFRACTION

The composition of the phase of Al_2O_3 sample was determined by a diffractometer for powder samples with vertical goniometer (Philips PW1710). The measurements were performed in these operating conditions:

- radiation: CuKα (λ=1.5Å) filtrated with a Ni filter;
- scanning interval: 2θ = 10-90°;
- scanning rate: 0.05° 2θ/s;
- count time: 12.5s.

The identification of the phase is made comparing the with the spectrum library (JCPDS) with an automatic research. The middle dimensions of the crystal were calculated with Scherrer equation (2.19):

$$\tau = \frac{(0.9 \cdot \lambda)}{(\pi / 180 \cdot \cos\theta \cdot \Delta 2\theta)} \tag{2.19}$$

where τ is the middle dimension of the crystal, $\Delta 2\theta$ is the middle high and the breadth of the peak (evaluated through the Rietveld anaysis of spettrum), λ is the wavelength of incident radiation and θ is the angle corresponding to the maximum peak of diffraction. In this work the X-ray diffraction was used to verify the composition of Al_2O_3. A X-Ray diaffractogram is reported in Figure 2.20 and it is possible to note that all the peaks are associated to α-Al_2O_3 underlining the finishing of the phase transition to α -phase.

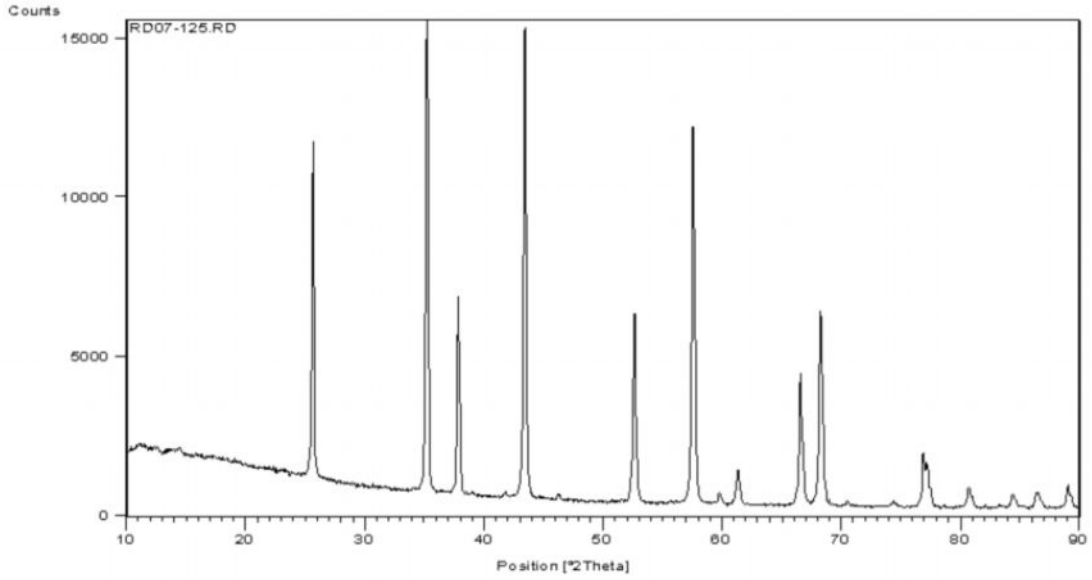

Figure 2.20: X-Ray diaffratogram.

2.7.2 BET ANALYSIS

The measurement of the specific surface area is performed with the Tristan instrument of Micromeritics, using the BET methods (Brunauer, Emmett and Teller, 1938). This technique used liquid N_2 at temperature of 77 K. The number of absorbed nitrogen moles increase with the pressure and the bond between these two quantities is given by the absorption isotherm.

BET isotherm considers a multilayer absorption and it is based on these assumptions:

- the molecules absorb on a flat uniform surface of the solid with a uniform heat of absorption due to van der Waals forces;
- there is no lateral interaction between the gas and the solid;
- after the surface has becomes partially covered by absorbed molecules, other molecules can absorbed either on the remaining surface or on top of adsorbed layer, and the heat of absorption of the subsequent layer is equal to the heat of liquefaction of the gas.

At low pressure (P<0.35 P°) the experimental data (pressure-absorbed quantity) are described by BET isotherm:

$$\frac{n}{n_m} = \frac{C \cdot \frac{P}{P^\circ}}{\left(1 - \frac{P}{P^\circ}\right) \cdot \left[1 + (C-1) \cdot \frac{P}{P^\circ}\right]} \tag{2.20}$$

where:

- P° is the vapour pressure of N_2 at saturation;
- n is the number of absorbed gas moles per gram of catalyst at the pressure P;
- n_m is the number of absorbed gas moles per gram of catalyst corresponding to the fraction of the monolayer;
- C is the difference between the released heat for the absorption of one molecule on the surface and the released heat for the absorption of one molecule on subsequent layers of molecules already absorbed.

For the calculation of the specific surface area it is necessary to know the number of moles of nitrogen absorbed on the monolayer per gram of catalyst, calculated by Equation 2.20, and the area occupied by a nitrogen molecule:

$$Area = n_m \cdot Area_{N2} \cdot N_{av} \tag{2.21}$$

where *Area* is the specific surface area expressed in [$m^2 g_{cat}^{-1}$], $Area_{N2}$ is the area occupied by one molecule of N_2 and N_{av} is the Avogadro number.
The specific surface area calculated through BET method is 7 $m^2 g^{-1}$. This measurement is in according with the result of the X-rays diffraction, which show that there is only the α phase.

2.7.3 MEASURAMENT OF THE POROUS VOLUME (MERCURY INTRUSION)

For the dry impregnation it is necessary to know with precision the porous volume of the support powder. So in this work the porous volume of α-Al_2O_3 was determined through

mercury porosimetry. The measurement was performed with the AutoPore IV 9500 VI.05 porosimeter of Micromeritics.

Since mercury does not spontaneously penetrate pores by capillary force because of its non-wetting propriety, it must be forced to go into the pores by applying an external pressure (Figure 2.21). So after a pre-treatment at void grade up to 5 psi and a hold of 5 minutes, there are two different pressurizations:

- low pressure analysis (50-900 μmHg): during this phase mercury penetrates intraparticle spaces and breaks the aggregates
- high pressure analysis (2-3300 μmHg): during this phase mercury penetrates the pores.

The required pressure to penetrate pores is inversely proportional to the size of the pores:

$$r_P = \frac{6300}{P} \tag{2.22}$$

where r_P is the radius of the pore expressed in [Å] and P is the pressure expressed in [atm].

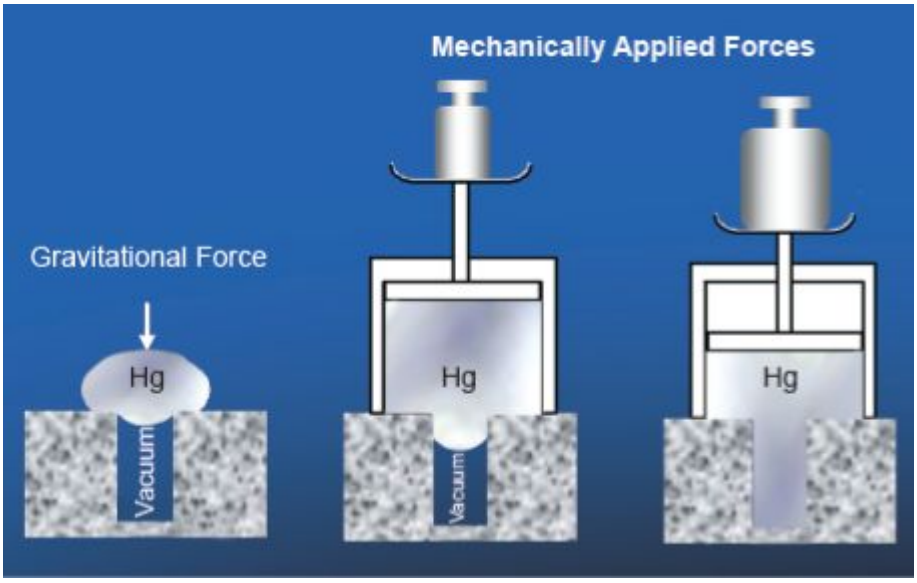

Figure 2.21: Mercury intrusion in the pore.

The porous volume of the Al_2O_3 sample is 0.2-0.3 cm^3g^{-1} with a mean diameter of the pores equal to 678 Å. The latter value is in line with the value of the specific surface area obtained by BET analysis.

CHAPTER 3

MONODIMENSIONAL MATHEMATICAL MODEL

3.1 ASSUMPTIONS AND GOVERNIG EQUATIONS

The experimental data were compared with the simulations of a mathematical model of the lab-scale reactor, developed in previous works [43]. The model of the fixed bed adiabatic catalytic reactor is dynamic, heterogeneous and monodimensional and it can simulate the behaviour of the reactor or with molecular, pseudo-steady-state kinetics or with single site C_1 microkinetic scheme. The model includes:

- the specie mass balances for the gas phase and solid phase;
- the energy balances for the gas and solid phase;
- the momentum balance.

Accumulation terms are considered in all equations, except in the mass balance for the solid phase because of the smaller volume of fluid in catalyst pores compared to fluid volume in the bulk. So steady-state conditions are considered for all the species of the solid phase. Besides, preliminary simulations show that the relevance of the dynamics of the gas phase is negligible; nevertheless the inclusion of the accumulation term in the equations improves the stability of the numerical solution. Model equations are listed in Table 3.1

In the case that the model incorporates the molecular scheme the effective reaction rates are considered in the solid-phase mass balance equations. The priori solution of the diffusion and reaction problem at a fixed reactor axial position (z) within the catalytic washcoat point out that the intraporous diffusional resistances for oxygen are greater by several orders of magnitude than for other species. Thus, intraporous diffusional resistances are accounted for by isothermal effectiveness factor only for combustion reactions, using the generalized Thiele modus method [44].

The effectiveness factor is defined as:

$$\eta = \frac{tanh(\phi)}{\phi} \tag{3.1}$$

where ϕ is the generalized Thiele modus, which is defined as:

$$\phi = \frac{1}{\eta^{\infty}} \tag{3.2}$$

The value of η^{∞} for a generic kinetic is calculated with this formula:

$$\eta^{\infty} = \frac{\sqrt{2}}{\rho_l \cdot r_v \cdot C_{O_2}^w} \cdot \left(\int_{C_X^w}^{C_{O_2}^w} D_{eff,O_2} \cdot r_v(c) \cdot dc \right)^{1/2} \tag{3.3}$$

where:

- ρ_l is the thickness of the catalytic layer;
- $C_{O_2}^w$ is the superficial concentration of oxygen;
- D_{eff,O_2} is the effective molecular diffusion of oxygen;
- c_X^w is the asymptotic concentration of O_2 inside the catalyst, it is the limit of integration and it is zero for oxygen which is the limited reactants and is characterized by extremely rate of consumption;
- $r_v(C_{O_2}^w)$ is the rate of consumption for oxygen.

Differently, if the model incorporates the microkinetic scheme the effectiveness factor is neglected.

The deviation of the experimental system from the ideal adiabatic condition is accounted for by introducing a global heat transfer coefficient between the reactor and the external environment in the energetic balance of gas phase. In fact through the global heat transfer coefficient (h_{ext}) it is possible to consider the radial dispersion of heat along the reactor and so the behaviour of the reactor can be simulated even if the value of the thermal efficiency α (§ par. 2.3) is less than the unity. The heat losses are defined by the integral:

$$\dot{Q}_{lost} = \int_{Zin}^{Zout} h_{ext} \cdot \left(T_{gas}(x) - T_{\infty}\right) \cdot \pi \cdot D \cdot dx \tag{3.4}$$

Due to the high Peclet number, axial diffusion is neglected in the gas phase [45].

Gas-phase reactions are accounted for using the detailed scheme of Frassoldati et al.[46]. In line with the reference [47], in CH_4-CPO no contribution from homogeneous chemistry was found under our operating conditions. Instead, in C_3H_8-CPO the reactions in homogeneous phases become important.

Gas phase

Species mass balance equations:

$$\frac{\partial \omega}{\partial t} = -\frac{G}{\rho_g \varepsilon}\frac{\partial \omega_i}{\partial z} - \frac{a_v}{\varepsilon} K_{mat,i}\left(\omega_i - \omega_{i,wall}\right) + \left(\sum_{j=1}^{NRhom} \nu_{i,j}\ r_j^{hom}\right)\frac{MW_i}{\rho_{gas}}$$

Energy balance equation:

$$\frac{\partial T_g}{\partial t} = -\frac{G}{\rho_g \varepsilon}\frac{\partial T_g}{\partial z} - \frac{a_v}{\rho_g \varepsilon \hat{c}_{p,g}} h\left(T_g - T_s\right) - \frac{4}{d_{ret}\rho_g \varepsilon \hat{c}_{p,g}} h_{ext}\left(T_g - T_{amb}\right) + \left(\sum_{j=1}^{NRhom} \nu_{i,j}\ r_j^{hom}\left(-\Delta H_{R,j}\right)\right)\frac{MW_i}{\rho_{gas}}$$

Momentum balance equation:

$$\left(-\frac{1}{\rho_g} + \frac{G^2}{\rho_g^2 p}\right)\frac{dp}{dz} - \frac{G^2}{\rho_g^2 T_g}\frac{dT_g}{dz} = \frac{1}{2}\frac{G^2}{\rho_g^2} a_v f$$

Solid phase

Species mass balance equations:

$$0 = a_v\, \rho_s\, K_{mat,i}\left(\omega_i - \omega_{i,wall}\right) + \left(\sum_{j=1}^{NR} \nu_{i,j}\, r_j^{eff}\right) MW_i\, \rho_s\, \xi$$

Energy balance equation:

$$\frac{\partial T_s}{\partial t} = -\frac{a_v}{\rho_s(1-\varepsilon)\hat{c}_{p,s}} h\left(T_g - T_s\right) + \frac{k_{ax}^{eff}}{\rho_s\, \hat{c}_{p,s}}\frac{\partial^2 T_s}{\partial z^2} + \left(\sum_{j=1}^{NR}\left(-\Delta H_{Rj}\right) r_j^{eff}\right)\frac{\xi}{\hat{c}_{p,s}(1-\varepsilon)}$$

Site balance:

$$\frac{d\theta_i}{dt} = \frac{s_i}{\Gamma_{Rh}}$$

Table 3.1: Model equations.

Boundary and initial conditions are listed in Table 3.2. The pressure and the temperature for the gas phase are fixed data. The radiative axial dispersion at the reactor boundaries is considered for the solid phase. Besides, the simulation accounted for the presence of an inert portion of support prior the catalytic bed.

Boundary conditions

Reactor inlet:

$$\omega_{i,z=z_1} = \omega_{i,\text{feed}} \qquad T_{g,z=z_1} = T_{\text{feed}} \qquad P_{z=z_1} = P_{\text{feed}}$$

$$-k_{\text{ax}}^{\text{eff}} \left.\frac{\partial T_s}{\partial z}\right|_{z_1} = \sigma\varepsilon_s \left(T_g^4 - \left. T_s^4 \right|_{z_1} \right)$$

Reactor outlet:

$$-k_{\text{ax}}^{\text{eff}} \left.\frac{\partial T_s}{\partial z}\right|_{z_2} = -\sigma\varepsilon_s \left(T_g^4 - \left. T_s^4 \right|_{z_2} \right)$$

Initial condition

$$\omega_i(z,0) = 0 \qquad T_g(z,0) = T_{g,\text{feed}} \qquad T_s(z,0) = T_{\text{room}}$$

Table 3.2: Boundary and initial conditions.

The nomenclature of the previous equations is:

a_v	specific area per unit volume [m^{-1}]
A	reactor cross sections [m^2]
$\hat{c}_p$	specific heat [J/kg/K]
d_{cell}	pore dimension [m]
f	friction factor
G	superficial mass flow rate [kg/m2/s]
h	heat transfer coefficient [$W/m^2/K$]
h_{ext}	heat transfer coefficient with the external environment [$W/m^2/K$]
$\Delta H_{R,j}$	heat of reaction [J/mol]
$K_{max,i}$	mass transfer coefficient [m/s]
L_{rct}	reactor length [m]
k_{eff}^{ax}	effective solid thermal conductivity [W/m/K]
P	pressure [Pa]
r_j	j-reaction rate [$mol/kg_{cat}/s$]
s_i	production rate for i specie [$mol/cm^2/s$]
θ_i	coverage site fraction [mol/cm^2]
Γ_{rh}	site density [mol/cm^2]
T	temperature [K]
z	reactor axial coordinate [m]
ε	bed void fraction
ε	emissivity
ξ	volumetric catalytic fraction

ρ density [kg/m^3]
σ Stefan-Boltzmann constant
ω weight fraction

Subscripts and superscripts

g gas phase
s solid phase
eff effective

Physico-chemical and transport proprieties are estimated according to the CHEMKIN correlations [48]. In particular, for the evaluation of the transport proprieties, the multi-average model of CHEMKIN package has been used.

3.2 NUMERICAL METHOD

The model consists of NC (number of species) partial differential equations (PDEs) and was solved numerically by the method of lines. The axial reactor length was split into a suitable number of grid points in each point the spatial derivates was approximated by the Euler Backward differential method. Thus, from a NC PDEs problem, a NC x $n_{grid\ points}$ DAE system was obtained. The DAE system was solved by the initial value C_{++} Class BzzDae for stiff problems [49] of the BzzMath 5.0 library [50]. This integrator can exploit the tridiagonal block structure of the Jacobian and resulted very efficient and robust. The convergence of the solution in time was checked using the internal criteria of the integrator. A adaptive mesh refinement scheme was employed in the axial coordinate, by reducing the local error below a threshold as follows. The initial steady state solution was obtained on a coarse equi-spaced grid. During an iteration, if the local error ε_i at the ith point is greater than $\varepsilon_{max,I,}$ a point is added between the ith and i+1th points. The procedure ended when at each axial point $\varepsilon_i < \varepsilon_{max,I}$. In the adaptive mesh refinement approach, the problem dimension increased progressively and the points were segregated where they were really needed.

3.3 KINETIC SCHEME

A steady-state molecular indirect-consecutive kinetic scheme of CH_4 partial oxidation over Rh catalyst was incorporated in the reactor model. The kinetic scheme was developed on the basis of a wide experimental campaign in annular reactor at high space velocity [51]. Herein, CH_4 partial oxidation tests, as well as CH_4 steam reforming and CO and H_2 rich combustion tests were performed at varying the temperature, flow rate, and feed composition far from the thermodynamic equilibrium, under quasi-isothermal conditions and reduced impact of mass transfer limitations. All kinetic tests were run under diluted conditions.

The heterogeneous reactions and the corresponding kinetics expressions are listed in Table 3.3 where:

- η is the ratio of experimental reaction quotient and the thermodynamic equilibrium constant

$$\eta_{SR} = \frac{K_{P,SR}}{K_{eq,SR}} \qquad with \quad K_{P,SR} = \frac{P_{CO} \cdot P_{H_2}^3}{\left(P_{CH_4} \cdot P_{H_2O}\right)} \tag{3.5}$$

$$\eta_{WGS} = \frac{K_{P,WGS}}{K_{eq,WGS}} \qquad with \quad K_{P,WGS} = \frac{P_{CO_2} \cdot P_{H_2}}{\left(P_{CO} \cdot P_{H_2O}\right)} \tag{3.6}$$

$$\eta_{RWGS} = \frac{1}{\eta_{WGS}} \tag{3.7}$$

- σ is a "limiting" factor which multiplies the reaction rate incorporated within the mass balance in order to account for the limiting concentration of O_2, H_2O and CO_2 and it is defined as

$$\sigma = \frac{P_i}{10^{-5} + P_i} \tag{3.8}$$

where P_i is the partial pressure of O_2 for combustion reaction and CO_2 and H_2O for reforming reactions.

- $k_j(T)$ is kinetic rate constant calculated according to the Arrhenius form:

$$k_j(T) = k(T_{rif}) \cdot e^{\left[-\frac{Eatt}{R}\left(\frac{1}{T}-\frac{1}{Trif}\right)\right]} \tag{3.9}$$

Rate equation (mol $g_{cat}^{-1} s^{-1}$)	k_i^{873K} (mol/(atm g_{cat} s)$^{-1}$)	E_{act} (kJ/mol)
CH_4 total oxidation: $CH_4 + 2O_2 \rightarrow CO_2 + H_2O$		
$r_{tot_{ox}} = \frac{k_{tot_{ox}} P_{CH_4}}{1 + k_{ads_{H_2O}} P_{H_2O}} \sigma_{O_2}$	1.030 x 10^{-1}	92
CH_4 steam reforming: $CH_4 + H_2O \leftrightarrow 3H_2 + CO$		
$r_{SR} = \frac{k_{SR} P_{CH_4} (1 - \eta_{SR})}{1 + k_{ads_{CO}} P_{CO} + k_{ads_{O_2}} P_{O_2}} \sigma_{H_2O}$	1.027 x 10^{-1}	92
Direct water gas shift: $CO + H_2O \rightarrow CO_2 + H_2$		
$r_{WGS} = \frac{k_{WGS} P_{H_2O} (1 - \eta_{WGS})}{1 + k_{ads_{H_2O}} P_{H_2O}} \sigma_{CO}$ $\eta_{WGS} < 1$	6.239 x 10^{-2}	25
Reverse water gas shift: $H_2O + CO \rightarrow CO_2 + H_2$		
$r_{RWGS} = k_{RWGS} P_{CO_2} (1 - \eta_{RWGS}) \sigma_{H_2}$ $\eta_{RWGS} < 1$	1 .276 x 10^{-2}	62
H_2 oxidation: $H_2 + 0.5O_2 \rightarrow H_2O$		
$r_{H_2ox} = k_{H_2ox} P_{H_2} \sigma_{O_2}$	2.638 x 10^{3}	62
CO oxidation: $CO + 0.5O_2 \rightarrow CO_2$		
$r_{COox} = k_{COox} P_{CO} \sigma_{O_2}$	1.938 x 10^{1}	76

Surface adsorption	$k_{ads,i}^{873K}$ (atm^{-1})	ΔH_{ads} (kJ/mol)
O_2	5.461	-73
H_2O	3.901 x 10^2	-16
CO	2.114 x 10^2	-37

Table 3.3: Kinetic scheme and parameter estimates.

Herein the reactions involved in the kinetic scheme will be described in detail:

- *CH_4 total oxidation*

$$r_{tot_{ox}} = \frac{k_{tot_{ox}} P_{CH_4}}{1 + k_{ads_{H_2O}} P_{H_2O}} \sigma_{O_2} \tag{3.10}$$

The expression shows that the total oxidation has a first-order dependence on CH_4 concentration and a zero-order dependence on the co-reactant concentration. The absence of any independence on the O_2 content in the reaction rate is coherent with the picture of a catalyst surface almost completely covered by O* adatoms, with a few sites for CH_4 adsorption, as pointed out in literature by experimental results over Rh and by numerical simulations with detailed kinetic models. Besides, the CH_4 combustion is moderately inhibited by water absorption, but this effect is little influenced by varying amount of water and this suggests that the available sites for H_2O adsorption are closed to the saturation.

- *CH_4 steam reforming*

$$r_{SR} = \frac{k_{SR} P_{CH_4} (1 - \eta_{SR})}{1 + k_{ads_{CO}} P_{CO} + k_{ads_{O_2}} P_{O_2}} \sigma_{H_2O} \tag{3.11}$$

The expression adopted for steam reforming has a first order dependence on CH_4 and it is independent from water. The steam reforming is delayed in the presence of O_2 and is influenced by the competitive absorption of the reacting species. The nature of inhibition is uncertain and is presently under investigation though the means of theoretical analysis; besides there is an inhibition of CO (or syngas) because the experimental data can be well described by assuming that the surface is saturated by the absorption of CO.

- *Water gas shift*

$$r_{WGS} = \frac{k_{WGS} P_{H_2O} (1 - \eta_{WGS})}{1 + k_{ads_{H_2O}} P_{H_2O}} \sigma_{CO} \tag{3.12}$$
$$\eta_{WGS} < 1$$

The equation has a zero-dependence on CO and first-order dependence on H_2O and is valid only when the term η_{WGS} is lower than the unity. Besides, it contains an inhibition term due to H_2O adsorption. This term was introduced on the basis of CPO tests under concentrated conditions. In fact, while in highly diluted experiments (with CH_4 concentration lower than 4%) WGS was equilibrated, at increasing concentration of reactants the reaction progressively deviated from the equilibrium and became kinetically controlled. So the inhibition term due to water was explicitly added in order to describe the progressive divergence of WGS from the equilibrium.

- *Reverse water gas shift*

$$r_{RWGS} = k_{RWGS} P_{CO_2} (1 - \eta_{RWGS}) \sigma_{H_2} \tag{3.13}$$
$$\eta_{RWGS} < 1$$

Equation reports that RWGS is first order dependent on CO_2 and independent of H_2. The contribution of reverse water gas shift is negligible in the CPO runs, but numerical and experimental CPO and steam reforming data point out that it is not possible to use one equation comprising both the direct and reverse WGS steps. The direct and the reverse step must be treated as two distinct reactions with different kinetic dependences and a coherent approach to equilibrium. For this reason when RWGS is active (when η_{RWGS} is lower than the unity) the WGS is forced to be nil and vice versa, when WGS is active the RWGS rate is set equal to zero.

- *H_2 and CO oxidation*

$$r_{H_2ox} = k_{H_2ox} P_{H_2} \sigma_{O_2} \tag{3.14}$$

$$r_{COox} = k_{COox} P_{CO} \sigma_{O_2} \tag{3.15}$$

First-order rate were adopted in according with the kinetics of CH_4 combustion. The kinetic role of post-combustion reaction is negligible with diluted feed streams, while in the case of concentrate mixtures, the consecutive oxidation contrast the equilibration of the WGS reaction and exert a control on H_2/CO ratio.

Besides, Donazzi at al. [52] had specifically addressed the kinetic role of CO_2 reforming, which was found to be negligible within the kinetic scheme of CH_4 catalytic partial oxidation over rhodium.

The kinetic constants obtained were referred to load and dispersion of rhodium in the 4% Rh/α-Al_2O_3 catalysts and then they were rescaled to the load and dispersion for the catalyst performed in the adiabatic reactor.

The model can also incorporated a single site C_1 microkinetic scheme, consisting of 82 surface reactions and 13 adspecies. It has been derived used a hierarchical multiscale methodology involving both semi-empirical methods (UBI-QEP) and first principle techniques [53,54]. The scheme was validated over a wide set of CH_4-CPO experimental data within an annular microreactor under quasi-isothermal conditions [51]. The resulting scheme was able to described several reacting system, namely CH_4 pyrolysis and oxidation, steam reforming, H_2- and CO-rich oxidations, WGS and reverse WGS.

3.3.1 KINETIC EXPRESSION FOR PROPANE CPO

The reaction mechanism for the catalytic partial oxidation of propane has developed in strict analogy with the methane scheme. The model accounts the formation of syngas through a consecutive scheme, consisting of deep oxidation and steam reforming of propane and methane, water gas shift, H_2 and CO post-combustion, and methanation. The kinetic expressions for the heterogeneous reactions were developed on the basis of a wide experimental campaign in annular reactor [51,55] and are listed in Table 3.4.

Rate equation (mol $g_{cat}^{-1}s^{-1}$)	k_i^{873K} (mol/(atm g_{cat} s)$^{-1}$	E_{act} (kJ/mol)
CH_4 total oxidation: $CH_4 + 2O_2 \rightarrow CO_2 + H_2O$		
$r_{tot_{ox}} = \frac{k_{tot_{ox}} P_{CH_4}}{1 + k_{ads_{H_2O}} P_{H_2O}} \sigma_{O_2}$	1.030 x 10^{-1}	92
CH_4 steam reforming: $CH_4 + H_2O \leftrightarrow 3H_2 + CO$		
$r_{SR} = \frac{k_{SR} P_{CH_4} (1 - \eta_{SR})}{1 + k_{ads_{CO}} P_{CO} + k_{ads_{O_2}} P_{O_2}} \sigma_{H_2O}$	1.027 x 10^{-1}	92
Water gas shift: $CO + H_2O \rightarrow CO_2 + H_2$		
$r_{WGS} = k_{WGS} \cdot P_{H_2O} \cdot (1 - \eta_{WGS}) \cdot \sigma_{CO}$ $\eta_{WGS} < 1$	6.831x 10^{-3}	75
Reverse water gas shift: $H_2O + CO \rightarrow CO_2 + H_2$		
$r_{RWGS} = k_{RWGS} P_{CO_2} (1 - \eta_{RWGS}) \sigma_{H_2}$ $\eta_{RWGS} < 1$	1.276 x 10^{-2}	62
H_2 oxidation: $H_2 + 0.5O_2 \rightarrow H_2O$		
$r_{H_2ox} = k_{H_2ox} P_{H_2} \sigma_{O_2}$	2.666 x 10^{3}	62
CO oxidation: $CO + 0.5O_2 \rightarrow CO_2$		
$r_{COox} = k_{COox} P_{CO} \sigma_{O_2}$	1.937 x 10^{1}	76
C_3H_8 total oxidation: $C_3H_8 + 5O_2 \rightarrow 3CO + 7\ H_2$		
$r_{Ox\_C_3H_8} = \frac{k_{Ox\_C_3H_8} \cdot P_{C_3H_8}}{1 + K_{ads\_H_2O} \cdot P_{H_2O}} \cdot \sigma_{O_2}$	3.036 x 10^{-1}	87
C_3H_8 steam reforming: $C_3H_8 + 3H_2O \leftrightarrow 3CO + 7H_2$		
$r_{SR\_C_3H_8} = \frac{k_{SR\_C_3H_8} \cdot P_{C_3H_8} \cdot (1 - \eta_{SR\_C_3H_8})}{1 + K_{ads\_CO} \cdot P_{CO} + K_{ads\_O_2} \cdot P_{O_2}} \cdot \sigma_{H_2O}$	2.486 x 10^{-1}	85
CO methanation: $CO + 3H_2 \rightarrow CH_4 + H_2O$		
$r_{Met} = k_{Met} \cdot P_{H_2} \cdot (1 - \eta_{Met}) \cdot \sigma_{CO}$	1.2 x 10^{-3}	88

Surface adsorption	$k_{ads,i}^{873K}$ (atm^{-1})	ΔH_{ads} (kJ/mol)
O_2	5.461	-73
H_2O	3.901×10^2	-37
CO	2.114×10^2	-57

Table 3.4: Kinetic scheme and parameter estimates for propane CPO.

Subsequently the expression kinetic for propane-CPO will be described in detail.

- *C_3H_8 total oxidation*

$$r_{Ox\_C_3H_8} = \frac{k_{Ox\_C_3H_8} \cdot P_{C_3H_8}}{1+K_{ads\_H_2O} \cdot P_{H_2O}} \cdot \sigma_{O_2} \tag{3.16}$$

The expression shows that the total oxidation has a first-order dependence on C_3H_8 concentration and a zero-order dependence on the co-reactant concentration, as in the case of CH_4 total oxidation. The activity of the propane is higher than that of the methane because the propane has lower activation energy and a the value of the pre-exponential coefficient is three times that of the methane. In a recent work [55] was verified that the propane total combustion was inhibited by water, as in the case of methane.

- *C_3H_8 steam reforming*

$$r_{SR\_C_3H_8} = \frac{k_{SR\_C_3H_8} \cdot P_{C_3H_8} \cdot (1 - \eta_{SR\_C_3H_8})}{1 + K_{ads\_CO} \cdot P_{CO} + K_{ads\_O_2} \cdot P_{O_2}} \cdot \sigma_{H_2O} \tag{3.17}$$

The expression adopted has a first order dependence on C_3H_8. The steam reforming is delayed in the presence of O_2 and for this reason a terms of inhibition of O_2 is considered. Besides there is another term of inhibition due to the CO absorption. In the formulation of this expression was assumed an independence from water to be coherent with the kinetic of methane steam reforming and because there are experimental uncertainty for the entity and the direction of the effect of water concentration.

- *CO methanation*

$$r_{Met} = k_{Met} \cdot P_{H_2} \cdot (1 - \eta_{Met}) \cdot \sigma_{CO} \tag{3.18}$$

The expression adopted has a first-order dependence on H_2. The reaction of methanation becomes important after syngas formation, therefore after 400°C and it influences the reaction of WGS and so the CO_2 production.

The other kinetic expressions are identical to that for the kinetic scheme of methane, previously described.

3.4 CATALYTIC BED PROPRIETIES

In this work the tests of CPO were performed on 400 CPSI cordierite monoliths or on 115 CPSI silicon carbide monoliths. The propriety of the cordierite and silicon carbide are reported in Table 3.5. The same proprieties of cordierite was also considered for the silicon carbide because it is a porous support.

	Cordierite	Silicon carbide
ρ [kg m^{-3}]	2300	2300
$\hat{c}_p$ [J kg^{-1}K]	925	925
k_S [W m^{-1}K^{-1}]	2.5	2.5

Table 3.5 Propriety of cordierite and silicon carbide.

The bed transport proprieties were accounted for by specific heat and mass transfer correlations. In the case of laminar flow in channel with square section the correlations of Shah and London were used:

$$Nu = 2.977 + \left(8.827 \cdot \left(10^3 \cdot Z^*\right)^{0.545}\right) \cdot exp\left(-48.2 \cdot Z^*\right) \tag{3.19}$$

$$Sh = 2.977 + \left(8.827 \cdot \left(10^3 \cdot Z^*\right)^{0.545}\right) \cdot exp\left(-48.2 \cdot Z^*\right) \tag{3.20}$$

where :

- $Z^* = \dfrac{z \cdot L_{ert}}{d_{cell} \cdot Re \cdot Sc}$ *for Sh*
- $Z^* = \dfrac{z \cdot L_{ert}}{d_{cell} \cdot Re \cdot Pr}$ *for Nu*
- $f = \dfrac{14}{Re}$
- $Re = \dfrac{d_{cell} \cdot G}{\mu \cdot \varepsilon}$

The effective thermal conduction of the solid was accounted for the correlation proposed by Lee and Aris [56] (3.21):

$$k_{ax}^{eff} = (1-\varepsilon)\cdot k_s + \frac{16}{3}\cdot\sigma\cdot 1.12\cdot\frac{d_{cell}}{2}\cdot T_s^3 \qquad (3.21)$$

CHAPTER 4

SPATIAL SAMPLING TECHNIQUE

4.1 INTRODUCTION

The catalytic partial oxidation operates under extremely high gradients of temperature and of composition and with complex fluid and kinetic patterns, where mass and heat transfer are coupled with the surface process. Because of the presence of these gradients, concentrated at the inlet of the reactor, the behaviour of the system could not be fully described by the unique analysis of the gas composition at the exit of the reactor. The spatially resolved sampling technique was herein applied to investigate the process. This technique allows to "look" directly inside the reactor through the measurement of axial temperature and composition profiles while the reactor is maintained under adiabatic conditions. This technique was presented for the first time by Horn at al. [22] in order to measure the species and temperature profiles for the catalytic partial oxidation of methane on autothermally operated Rh-coated α-Al_2O_3 foams in steady-state and transient mode. In this wok the spatial sampling technique was applied for the thermal behaviour of the honeycomb catalytic monoliths.

In this chapter will be described the temperature probes and species probe in the spatial sampling technique, which allow to measure the axial temperature and composition profiles.

4.2 SET UP OF TEMPERATURE PROBES

The correct measurement of the temperature for the gas phase and for the catalytic surface is crucial to interpret correctly the overall behaviour of the reactor. In fact surface temperatures are obviously very important for the heterogeneous chemistry which is taking place on the supported metal catalyst present in the monolith, while the gas temperature are equally important for the homogeneous chemistry taking place in the empty volumes of the catalyst. A thermocouple or a fiber optic are the detectors which have been employed to measure temperature profiles inside CPO catalysts.

.

Temperature probe consists of a empty fused silica capillary (670 μm outer diameter and 530 μm inner diameter). Inside the capillary there is a K-type thermocouple (inner diameter of 500 μm) or a fiber optic (Figure 4.1) which directly views the surface of the monolith because the fused silica capillary is transparent to the radiation. .

Figure 4.1: Fused silica capillary containing thermocouple (left) and optical fiber (right).

Either in the case of thermocouple and optical fiber, the empty fused silica capillary is sealed at one end (Figure 4.2) to avoid any gas leakage. The sealing was obtained by heating with oxyacetylene torch until the capillary collapsed on itself. The oxyacetylene torch was a type 55H200 of Kemper group because it can achieve high temperatures needed for softening fused silica.

Figure 4.3: Sealed capillary.

4.3 OPTICAL FIBER PYROMETRY

The application of the optical fiber pyrometers in honeycomb monoliths for heterogeneous catalysis have been previously explored in the literature [57]. However, the technique was exclusively applied to NO_x abatement experiments, wherein the condition were almost isothermal. In recent works, optical fibers have also been applied to CPO due to the strong temperature gradients. [58]

4.3.1 THEORICAL BASIS FOR THE RADIATION MEASURAMENT

All bodies radiate energy to their surroundings. The power radiated per unit area is called emittance, which for a blackbody (a body which absorbs all the radiation it receives and radiates in all wavelength interval) depends only on the temperature, according with the Stefan-Boltzmann law:

$$Q_b(T) = \sigma \cdot T^4 \tag{4.1}$$

where σ is Boltzmann constant, which values $5.67 \cdot 10^{-8}$ W/(m^2·K^4).

Since the emittance is distributed over the entire spectrum, the monochrome emittence ($I_{\lambda,b}$) is introduced. The monochromatic emittance is the power emitted at a given wavelength so that:

$$Q_b(T) = \int_{\lambda_1}^{\lambda_2} I_{\lambda,b}(\lambda, T) \cdot d\lambda \tag{4.2}$$

The monochromatic emittance is defined by Planck law:

$$I_{\lambda,b}(T, \lambda) = \frac{C_1}{\lambda^5 \cdot \left(e^{C_2/(T \cdot \lambda)} - 1 \right)} \tag{4.3}$$

In the equation:

- C_1 is the first radiation constant =3.7415 x 10^{16} watts/m^2
- C_2 is rhe second radiation constant = 1.43879 x 10^{-2} m.

This function is plotted for several temperature in Figure 4.3.

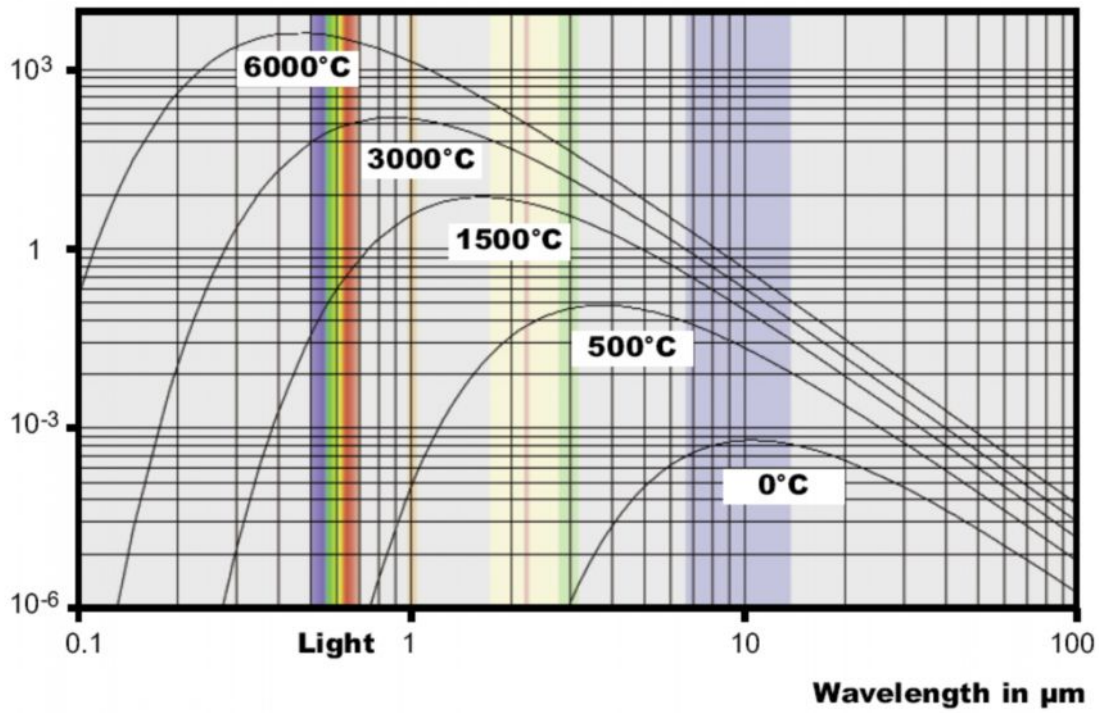

Figure 4.3:Radiation intensity as function of wavelength and temperature according to the Plank law.

The emission coefficient or emissivity ε is the ratio of the thermal radiation emitted by any object to the thermal radiation emitted by a black body radiation source at the same temperature.

$$\varepsilon(\lambda,T)=\frac{I_{\lambda}(\lambda,T)}{I_{\lambda,b}(\lambda,T)} \tag{4.4}$$

The emissivity depends on the material of the object and changes with wavelength, temperature or other physical proprieties [59].

4.3.2 PYROMETER

A narrow-band infrared pyrometer (Impac Infrared, IGA 5-LO) was used for the measurement of the solid phase. The pyrometer consisted of a measuring transducer connected to an optical fiber. The measuring transducer included the lens system, the IR detector and the signal process. The infrared radiation emitted by the object of the measurement is collected by the lens. The aperture blocks unwanted peripheral rays. The filter lets only the selected spectral range pass through. The portion passing the filter falls on the detector which transforms the infrared radiation into an electrical signal (Figure 4.4) [60].

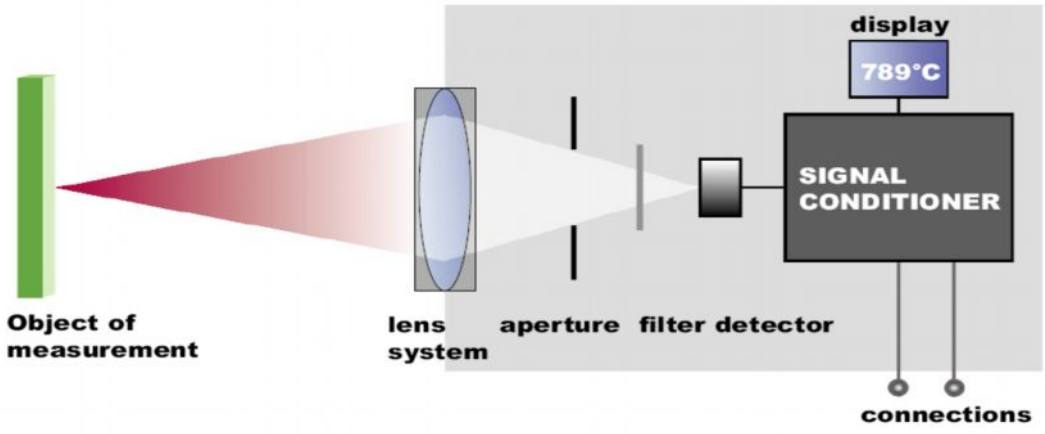

Figure 4.4:Components of pyrometer.

The photon detector converts the UV-IR radiation in potential difference. The detector acts as an electron counter where the potential difference is proportional to the number of photons which fall on the surface.

4.3.3 OPTICAL FIBER

The optical fiber is used as a probe for transmitting the radiation from the inlet part of the reactor to the measuring transducer. The structure of an optical fiber (Figure 4.5) consists of a central part called core, of refractive index n_F, surrounded by a material called the cladding of lower refractive index n_C. In fact to provide the guideline of the light the core of the fiber is doped with a small percentage of a substance that increases the refractive index. In this way the electromagnetic waves can be confined in the core region and then transmitted by total internal reflection at the core/cladding boundary. In the present work, the core diameter of the optical fiber is 300 µm, while the diameter of the clad is about 330 µm. The fiber is coated with a polymeric jacket whose outer diameter is 370 µm. As the refraction index n_F in the core, which is uniform, is higher than that n_C of the cladding, a step-index waveguide is formed. Therefore the principle of total reflection of a light ray can be applied. Considering a ray in air, which strikes the core of the fiber at an angle θ_I to the fiber axis, due to the refraction at the air/glass surface, the angle of the ray to the axis change to θ as it enters the core in according with this formula (4.5):

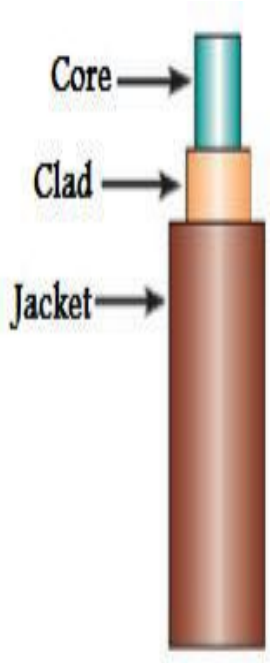

Figure 4.5:Section of optical fiber.

$$\frac{\sin\theta_I}{\sin\theta} = n_F \tag{4.5}$$

If the ray strikes the core with an angle less or equal to the critical angle of acceptance, the ray propagates along the core because there are multiple reflections at the interface between the central core and the external cladding without loss of energy. Instead, if the ray strikes the core with a angle greater than the critical angle, partial reflections take place and some energy is lost by refraction into the cladding. After several successive reflections, very little energy is left in the core (Figure 4.6) [59].

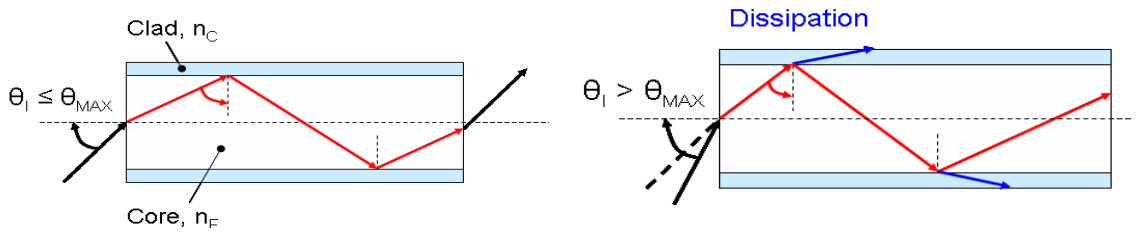

Figure 4.6: Reflection of ray in a optical fiber.

The critical angle of acceptance can be calculated knowing the refraction index of core, clad and the media, where the fiber is insert, through this formula (4.6):

$$\sin\theta_{MAX} = \frac{1}{n_{MEDIA}} \cdot \sqrt{\left(n_F^2 - n_C^2\right)} \tag{4.6}$$

The numerical aperture (N.A.) is an intrinsic characteristic of the fiber which depends on the refractive indices of the core and the cladding material and it is defined as (4.7):

$$N.A. = \sin\theta_{MAX} \cdot n_{MEDIA} = \sqrt{\left(n_F^2 - n_C^2\right)} \tag{4.7}$$

Considering that the core and the cladding is basically bulk fused silica, a weak influence can be expected in relative variation of the refraction indices with the temperature. The numerical aperture for the optical fiber adopted in the present work is 0.22 and it can be reasonably defined as a constant. The n_{MEDIA} also depends on the temperature and composition of the transmitting media: however for the gas mixture considered in the present work derivation from unity are negligible. As a consequence, it can be reasonably assumed that the angle is 12.7° under all the investigated conditions.

The cone of light rays that a fiber collects and transmits is termed acceptance cone and it depends on the tip of the fiber. A flat and a 45° tip have been considered (Figure 4.7).

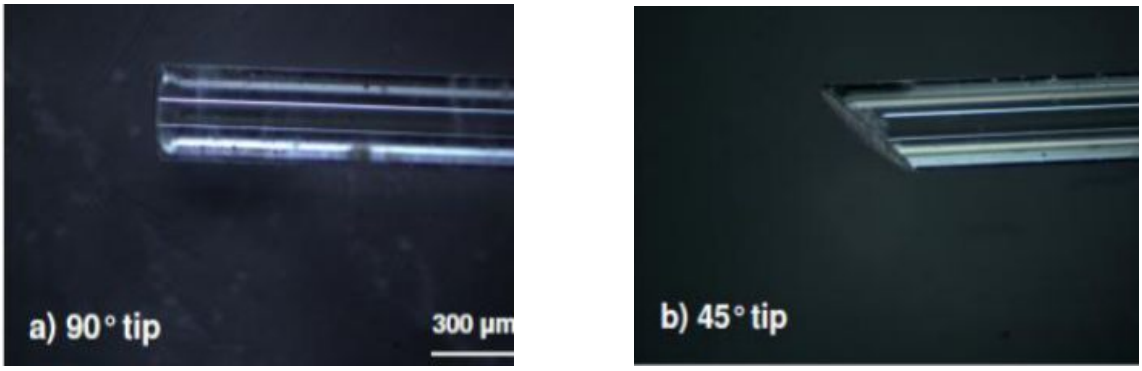

4.7: Optical fiber with flat tip (a) and with 45° tip (b).

Experimentally, the acceptance cone can be visualized by directing a red laser beam inside the fiber, the opposite way the incoming thermal radiation travels during the measurements. The laser beam crosses the tip, tracing the acceptance cones. The angle of the tip governs the orientation of the acceptance cone of the optical fiber. Flat tips exclusively transmit the radiation coming from the front of the fiber; in fact flat tips are front-looking probes (Figure 4.8). A no null gap is present between the actual position of the tip and the beginning of the radiating surface (segment AB in Figure 4.8). 45° polished tips predominantly accept radiation from the lateral direction, perpendicular to the fiber axis and opposite to the beveled surface. Due to total internal reflection, the beveled surface behaves like a turning prism, which directs the lateral radiation inside the fiber.

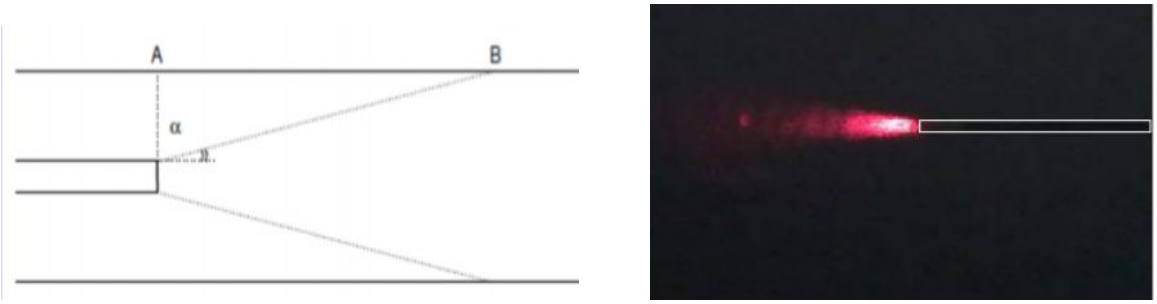

Figure 4.8:Acceptance cone of a optical fiber with flat tip.

In the case of 45° cut fibers, a fraction of the incoming radiation is also collected from another direction, which was experimentally found at an angle of about 20° off the axis (Figure 4.9). The secondary acceptance cone is due to the radiation that enters the fiber by refraction through the beveled surface. The importance of the secondary contribution depends on the fiber materials, but in generally minor, less 10% of the relative intensity of the primary acceptance cone. Because of the secondary acceptance cones, when sliding in the channel, the 45° tip collects the radiation coming from the walls (segments AB and CD in Figure 4.9).

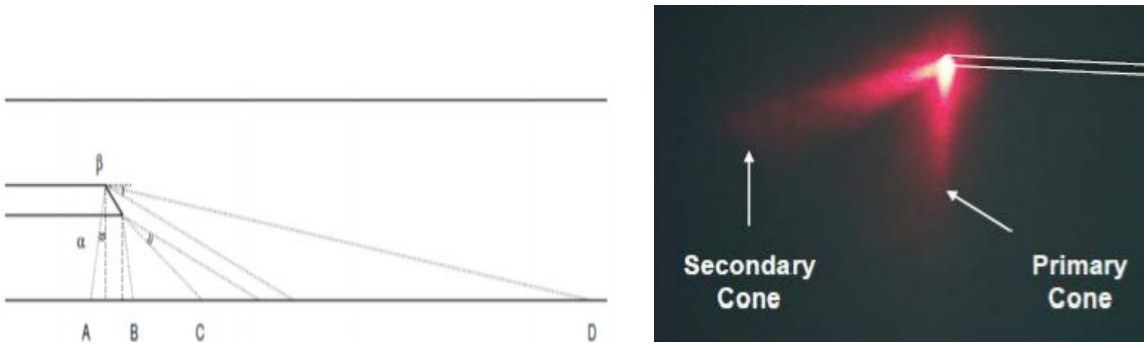

Figure 4.9: Acceptance cone of a optical fiber with 45° tip.

As reported in Donazzi et al. [58] the analysis of temperature profiles and of the goniometric characteristics of the optical fiber clearly indicates that 45° angled fibers are preferred for spatially resolved measurements, owing to the capability of looking at a precise spot on the surface of the catalyst support. In contrast, the use of 90° angled fibers leads to an average measurement, which underestimated the hot spot (Figure 4.10). For these reasons in this work optical fibers with 45° tip were used to sampled the axial temperature profiles.

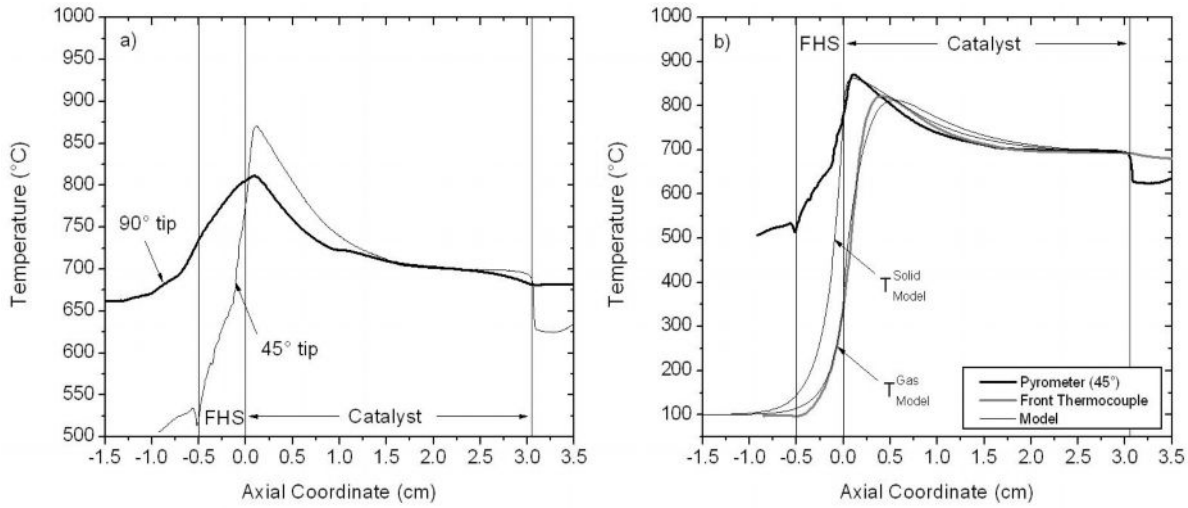

Figure 4.10: Effect of the angle of the optical fiber tip. Feed composition: CH_4 = 27.3%, O_2/CH_4 = 0.56. Flow rate = 20 Nl min^{-1}, T_{IN} = 100°C. Panel a: comparison between temperature profiles collected with a 90° fiber (thick lines) and a 45° fiber (thin lines). Panel b: comparison between experimental (thick lines) and model (thin lines) results.

4.3.4 CALIBRATION

The voltage output from a narrow band optical measuring in the wavelength range λ_{max}-λ_{min} is a function of the emissivity of the target surface ε_S, of the transmissivity of optical fiber and of the intervening media τ, of the gain of the detector R and of the radiance L.

$$V(T) = \int_{\lambda\,\min}^{\lambda\,\max} \varepsilon_S(\lambda) \cdot \tau(\lambda) \cdot R(\lambda) \cdot L(\lambda, T) \cdot d\lambda \qquad (4.8)$$

In general, the surface emissivity and the transmissivity of the optical fiber are not known and a calibration is required wherever a new material or a new fiber is tested. The surface emissivity ε_S is an intrinsic characteristics of the target material (in this case the catalyst) which depends on his roughness. As well, also the geometry of the catalyst support can lead to local variations of the surface emissivity. Different from the trasmissivity, which is fixed and calibrated by the manufacturer, the emissivity is an input parameter that as to be set before taking the measurement with the pyrometer. As received, the pyrometer was already calibrated against an artificial blackbody source (ε_S = 1) by using a 45° angled fiber. The standard procedure suggests to measure the temperature of the target surface and compare it with that of a reference blackbody source maintained at the same temperature. If a lower temperature than that of the reference is found, the emissivity of the target surface is less than 1 and the emissivity parameter of the pyrometer is adjusted so that the two measurement match.

The pyrometer output was calibrated by comparison with thermocouple measurements. The measurements were performed between 400 and 900 °C, in stagnant air. A blank 400 CPSI cordierite honeycomb and two heat shields were placed in a quartz reactor, externally

heated by a tubular furnace. The same standard internal layout adopted in the adiabatic reactor (in terms of relative distance between the honeycomb and the heat shield) was maintained. First, in order to obtain a surface emissivity close to the unity, the honeycomb was coated with a dull black-paint (Aremco High Emissivity Coating 840 C). The temperature profiles were collected both with the optical pyrometer and with the thermocouple, by sliding the quartz capillary in a central channel of the honeycomb. The capillary was moved exclusively within the channel and strictly isothermal temperature profiles were obtained. The profiles measured by the thermocouple matched the set point of the oven. The calibration revealed that the pyrometer measurements always overestimated the thermocouple measurements. Indeed, when setting the input emissivity parameter of the pyrometer at 1, the following linear correlation was derived through a linear regression of the experimental data (Figure 4.11):

$$T_{calibrated} = 0.936 \cdot T_{measured} + 22.9 \tag{4.9}$$

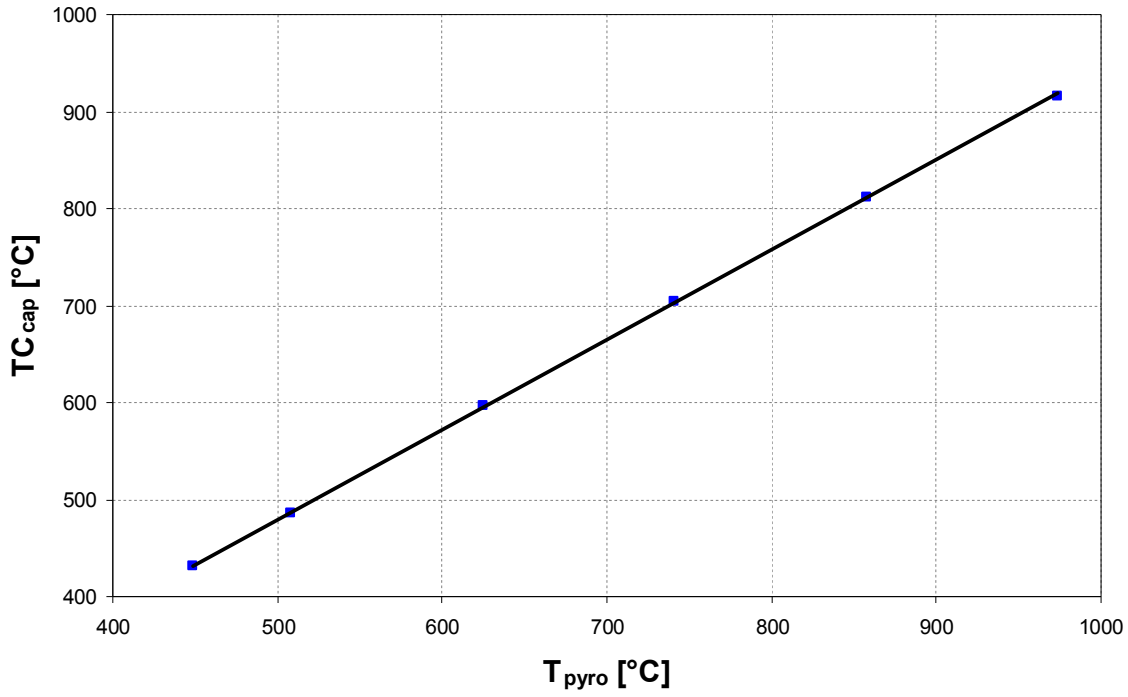

Figure 4.11: Calibrated line for the pyrometer.

Identical results were obtained also when a 90 ° angled fiber was used. The calibration was repeated with a catalyst coated sample: no difference was observed by comparison with black painted sample. This results allowed to estimated a blackbody emissivity for the catalyst layer. The calibration was repeated with uncoated cordierite honeycomb ($\varepsilon_S = 0.6$ for cordierite) to understand if the blackbody emissivity was due to the roughness of the layer or to the geometry of the channel. Also in this case no difference was observed compared with the previous results. This indicates that the geometry of the catalyst support plays a dominant role in the pyrometer measurement.

These results are in line with the emissivity enhancement effect that is present in cavities as a consequence of multi-reflection. A blackbody radiation can be achieved within an isothermal enclosure also in the case of a non blackbody emitter ($\varepsilon_S < 1$) if proper geometrical conditions are realized: a local apparent surface emisivity ε_A, which is a function of ε_S, of the diameter D of the enclosure and of the distance x of a target from the end section. For cylindrical holes with a surface emissivity larger than 0.6, the apparent emissivity approaches 1 when the ratio between x and D is larger than 6. In practise, unless ε_S is very small, a cavity more than only a few diameter deep emits the same amount of radiation of a infinitely deep cavity and can be approximated as a blackbody. The channels of the honeycomb (30 mm long and 1.2 mm size) guaranteed that a blackbody emissivity could be obtained sufficiently far off the exit section.

4.4 SPECIES PROBE

The species probe consists of empty fused silica capillary through which the gases, from any axial position along the reactor, can be sampled and analyzed in micro-gas chromatograph. The design of the species probe is important to ensure that the suction of the species has a minimal impact on the overall system with respect to how much volume is sampled and how the species are removed. So the volumetric flow through the capillary has been measured and its value was on the order of 5 Nml min^{-1}, while the flow rate in each channel of the monolith was about 36 Nml min^{-1}, so there was a disturbance of 15% on the flow rate in the channel during the suction. Subsequently, the analysis of species sampling system has been performed considering different diameters, then it was also evaluated the influence of the position of sampling. In fact because of the configuration of the system it was possible to sample from inlet or end of the reactor. Finally, the axial composition profiles were compared with the results of the simulations. The axial profiles are characterized by a resolution of 1 mm in the zone where there are the gradients, while a resolution of 5 mm in the zone of plateau.

4.4.1 EFFECT OF THE CAPILLARY DIAMETER

The axial composition profiles (Figure 4.12) were measured from the inlet of the reactor with two different capillary characterized by the following geometric data:

- outer diameter of 670 μm and inner diameter of 530 μm, after called capillary 1.
- outer diameter of 340 μm and inner diameter of 200 μm, after called capillary 2.

The capillary with a outer diameter of 340 μm was chosen the basis of empiric considerations; in fact reducing the outer diameter the overall dimension of the capillary was minimized and fluid dynamics was less disturbed, even if the presence of the capillary affects the flow field, changing it from the characteristic laminar parabolic profile to an

annular profile. Capillary with lower diameter than 340 μm could not be use because the pump of micro-GC was not able to suck.

Figure 4.12 reports the axial profile of the reactants with the two capillary. Figure 4.12 reports also the model predictions (solid lines). In fact, in order to evaluate the effect of the presence of the capillary in the channel, the experimental data obtained with the two capillary were compared with the model predictions. The oxygen profile was considered because the consumption of this specie was controlled by external mass-transfer [61] and so it was only influenced by the fluid dynamics. The model reproduced the experimental data. A minimal effect occurred on the fluid dynamic for the capillary with a outer diameters of 340 μm.

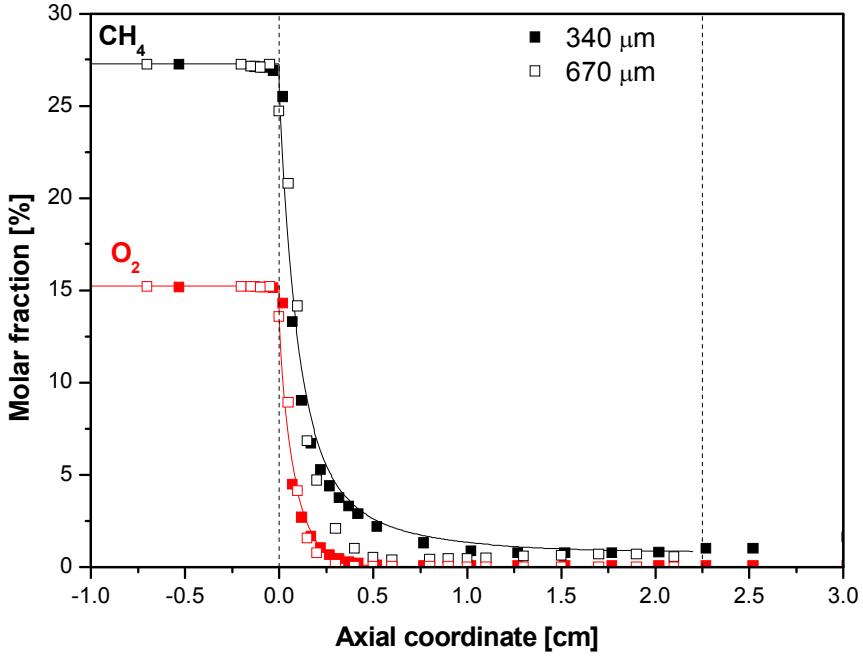

Figure 4.12: Spatially resolved profiles of composition for reactants using capillaries having different outer diameters from the cold side of the reactor (600, 340 μm) for Sample 1. Operating conditions: preheating, CH_4/Air mixture, 0.56 O_2/CH_4 ratio, 10 Nl min^{-1} flow rate ,atmospheric pressure. Symbols: experimental data. Solid lines: model predictions.

4.4.2 SAMPLING POSITION

For the two capillary the effect of the position of sampling probe was evaluated. In fact, because of the reactor configuration, it was possible to insert the capillary from inlet section where the reactants were fed, cold side, or from the outlet section of the reactor, hot side, (Figure 4.13). In Figure 4.14 the composition profiles collected with the two configurations (hot and cold side) are before shown for the capillary with an outer diameter of 340 μm.

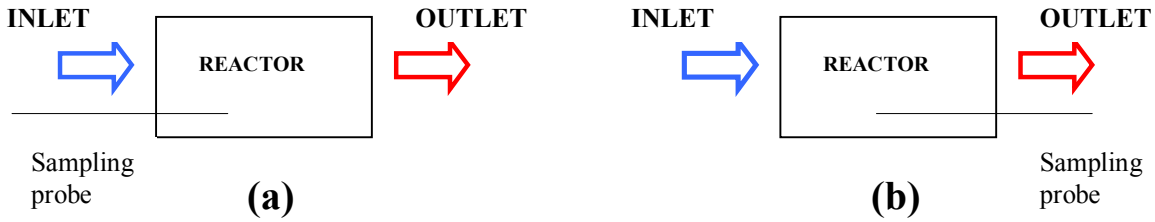

Figure 4.13: Sampling from the cold side of the reactor (a) and sampling from the hot side of the reactor (b).

In this case it was observed that the best configuration was that with the sampling from the cold side. In fact in this way the possibility of secondary homogeneous reactions inside the capillary were minimized because the gas was quenched after a very short time by the incoming cold reactants as the residence time in the hot zone was shorter than any ignition delay time for homogeneous reaction. Besides, the fluid dynamic could be less perturbed when the capillary was co-current (cold side) to the flow respect to the case when it was counter-current.

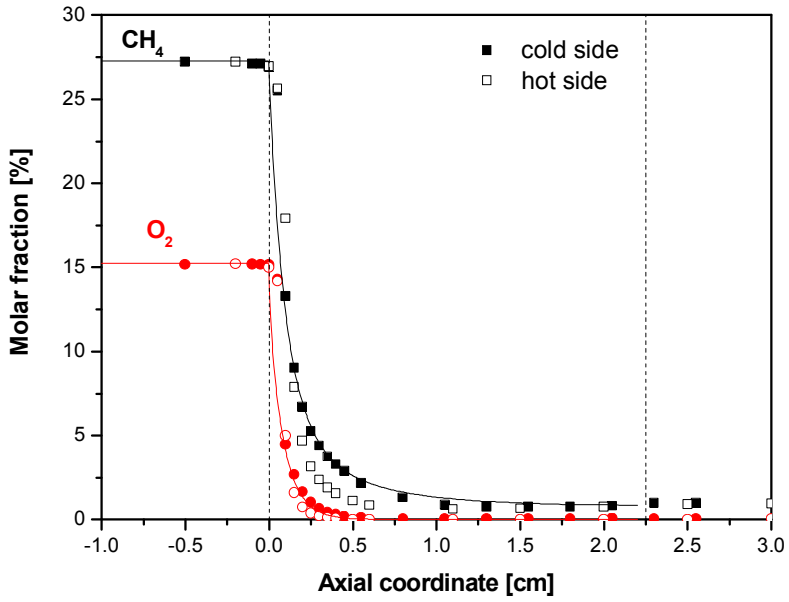

Figure 4.14: Spatially resolved profiles of composition for the reactants using the capillary with the outer diameter of 340 µm, sampling from the hot and the cold side of reactor. Sample 1.Operating conditions: preheating, CH_4/Air mixture, 0.56 O_2/CH_4 ratio, 10 Nl min^{-1} flow rate, atmospheric pressure. Symbols: experimental data. Solid lines: model predictions.

Finally, the composition profiles acquired with the capillary with a outer diameter of 600 µm are reported. In this case the fluid dynamics was so disturbed that there was not difference between the sampling from the hot and cold side of reactor (Figure 4.15).

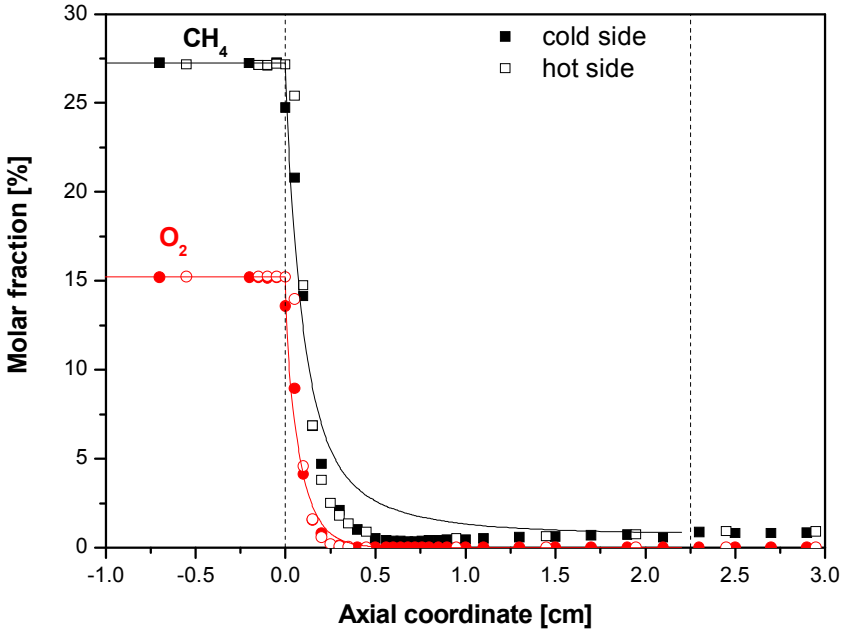

Figure 4.15: Spatially resolved profiles of composition for the reactants using the capillary with the outer diameter of 600 μm, sampling for hot and cold side of reactor. Sample 1.Operating conditions: preheating, CH_4/Air mixture, 0.56 O_2/CH_4 ratio, 10 Nl min^{-1} flow rate ,atmospheric pressure. Symbols: experimental data. Solid lines: model predictions.

Therefore the configurations with sampling from the cold side and with the capillary with an outer diameter of 340 μm is been adopted.

4.5 REACTOR RADIAL PROFILES: APPLICATION OF THE SPATIALLY RESOLVED SAMPLING TECNIQUE

In this section we report the result of the application of the sampling technique for the of radial profiles inside the monolith reactor. In principle we would expect that all channel behave similarly because a homogeneous distribution of the flow and of the temperature is guarantee at the entrance, besides the reactor has an adiabatic behaviour. However, we could not exclude that peripherical channels suffer from some heat dispersions towards the external reactor wall. We thus compare the effective behaviour of peripherical channel with that of a central channel (Figure 4.16).

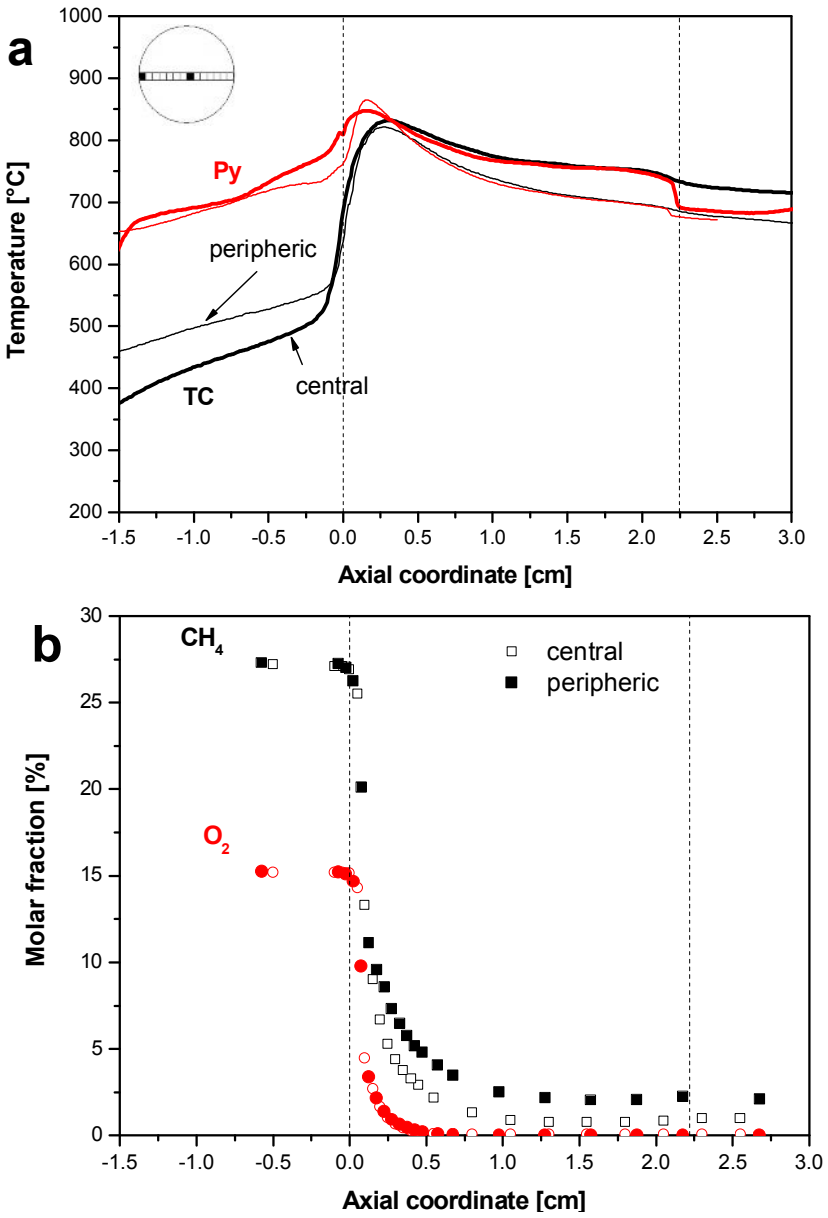

Figure 4.16: Spatially resolved profiles of temperature and composition in peripheric and central channel for Sample. Operating condition: preheating, mixture CH_4/Air at O_2/C ratio of 0.56 , flow rate 10 Nl min^{-1},atmospheric pressure.

Figure 4.16 shows that in inlet zone the temperature of hot spot were similar in both channels, in fact in this zone the exothermic oxidation reactions were important and caused a rapid rate of oxygen consumption in both channels, in fact the oxygen was completely consumed within 5 mm. The reforming reactions became more important when the oxygen was completely consumed. These reactions were controlled by thermodynamic, so the highest dispersion of heat in the peripheric channels reduced their temperature. Therefore the reforming reactions were less favoured and so the conversion of methane was lower than that in the central channel. Besides, in peripheric channel the condition of equilibrium was not reached because there was not a plateau in the temperature profiles for the gas and the solid phase.

In Table 4.1 are reported the conversion of reactants, the selectivity at H_2 and CO, the outer temperature.

Channel	χCH_4 [%]	χO_2 [%]	σH_2 [%]	σCO [%]	T_{out} [°C]
central	95.97	99.46	96.38	93.66	723
peripheric	89.09	99.85	93.26	89.18	675

Table 4.1: Steady-state performance of the tests at the outlet of the central and peripheric channel. Sample 1, CH_4/Air 10 Nl min^{-1}.

The lower conversion of methane in the peripheric channel explains the data obtained at the outlet of the reactor, after the mixing of outgoing flow from the channel of the catalyst. These data are reported in table 4.2. In fact the conversion of methane at the outlet of reactor is lower than that at outlet of the central channel. This difference is due to the mixing downstream of the catalytic honeycomb.

		χCH_4 [%]	χO_2 [%]	σH_2 [%]	σCO [%]	T_{out} [°C]
reactor	Exp	92.32	99.95	93.88	91.61	723
	Eq	93.77	100	94.35	92.19	731

Table 4.2: Steady-state performance of the tests at the outlet of the reactor. Sample 1, CH_4/Air 10 Nl min^{-1}.

Therefore to evaluate the mixing downstream the catalytic monolith, the species profiles has been sampling in the zone of mixing (Figure 4.19).

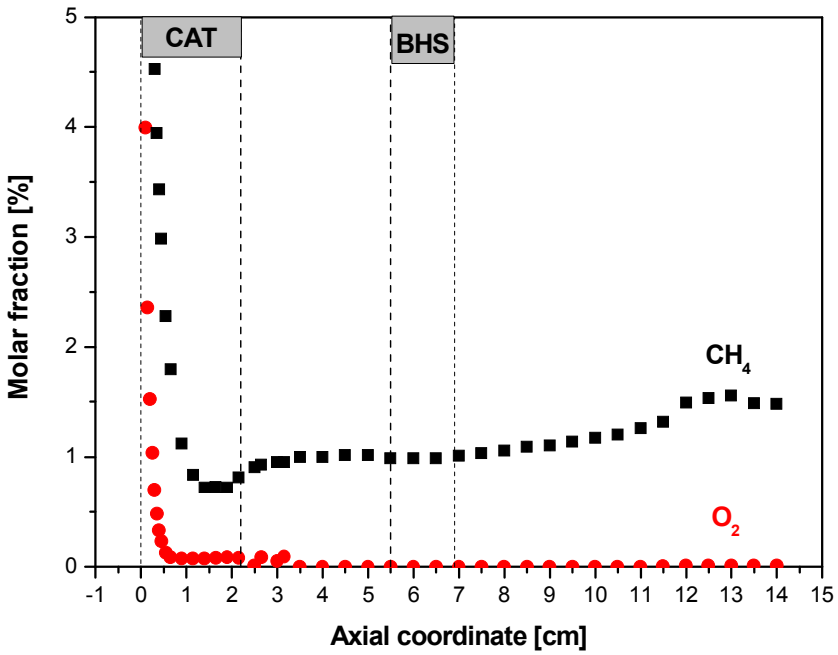

Figure 4.17: Spatially resolved profiles of composition to evaluated the mixing effect. Sample 1, preheated conditions, mixture CH_4/Air, flow rate 10 Nl min^{-1}, O_2/CH_4 0.56.

Figure 4.17 shows as the first mixing occurs in the void between the catalytic monolith and the back heat shield that corresponds in the graph to the range 2.2-5 cm. While there is another mixing after the back heat shield (at 6.9 cm).

CHAPTER 5

OPTIMAL REACTOR DESIGN: CATALYST DESIGN

5.1 INTRODUCTION

This chapter reports the results of a set of tests that aimed at identifying and demonstrating optimization strategies for CH_4-CPO reformers. The idea behind this investigation is that the hot-spot can be minimized operating on the catalyst design, in particular on the channel opening and on the catalyst load. Firstly, tests were carried out to study the effect of these parameters on the thermal behaviour of the CPO reactor and in particular on the hot-spot at the inlet section under standard conditions:

- total flow rate of 10 Nl min^{-1};
- mixture 27.4 % of methane and 72.6% of air;
- overstoichiometric O_2/CH_4 ratio of 0.56;
- preheating of the reactant mixture;
- "separated-FHS-configuration" (§ par. 2.3).

After the analysis under standard conditions, the effect of the parameters was evaluated at high flow rate (15, 20 Nl min^{-1}).

In all the tests, the steady-state conditions were analyzed with spatially resolved profiles of temperature and composition obtained with the sampling technique described in chapter 4. The experimental methane conversion and the yields to synthesis gas were compared with the values obtained by the adiabatic equilibrium. The algorithm used to calculate the equilibrium is based on STANJAN [62] bank data and it minimizes the free Gibbs energy at constant pressure and enthalpy. Besides, in each experiment the thermal efficiency was calculated to verify that the adiabatic conditions were effectively realized. The thermal efficiency is the ratio between the experimental temperature rise and the theoretical adiabatic temperature rise of the gas phase:

$$\alpha = \frac{T_{EXP}^{OUT} - T_{EXP}^{IN}}{T_{ADIABATIC}^{OUT} - T_{EXP}^{IN}} \tag{5.1}$$

where T_{EXP}^{IN} is the inlet gas temperature, T_{EXP}^{OUT} is the outlet gas temperature and $T_{ADIABATIC}^{OUT}$ is the adiabatic temperature, calculated at the composition of the outlet gas mixture.

5.2 REFERENCE HONEYCOMB MONOLITH

We herein characterize the performance of a "standard" honeycomb monolith, Sample 1 (§ par. 2.6.4) with 400 CPSI cell density and a catalyst load of 250 mg corresponding to a washcoat layer of 6 μm. Initially, the study of the thermal behaviour of the reference honeycomb monolith was carried out under "standard conditions". The measured profiles of temperature and composition, obtained by applying the spatial sampling technique are reported in Figure 5.1.

The measured profiles of temperature indicated the presence of a hot-spot along the first cm of the inlet section. The optical pyrometer showed a maximum temperature of about 848 °C, while the sliding thermocouple measured a maximum temperature of about 831 °C located at some distance from the hot-spot of the surface. Beside, the temperature profiles showed that in the inlet section the surface temperature was much higher than the gas temperature as the heat generation at the catalyst surface is much faster than the heat transport to the incoming gas. Then, both the temperature profiles became relatively flat downstream of the hot-spot, thus suggesting that the thermodynamic equilibrium was reached.

Concerning the measured concentration profiles, it was found that O_2 conversion was complete within 5 mm from the catalyst entrance. Also methane was consumed at a great extent within the same short length; in fact at 5 mm, the conversion of methane was 89%, but it further increased up to 95% a few millimetres downstream. The measurement of the product distribution showed that hydrogen and CO were produced from the very entrance and synthesis gas production grew rapidly along the axial coordinate (mostly within the first 5 mm); also water was rapidly formed at the very entrance but its concentration passed through a narrow peak (with a maximum located at about 1 mm from the inlet section) and then also rapidly decreased to a low outlet concentration. CO_2 was also formed in small amount.

Figure 5.1 also reports the model predictions (solid lines). The temperature of the catalyst and of the gas phase were predicted in close agreement in the reforming zone where the thermodynamic equilibrium was reached, while, for both the phases, the model predicted higher temperature at the inlet section than the temperatures experimentally measured. This was due to the heat dispersion by radiation from the frontal section: indeed, in the configuration considered (separated-FHS-configuration) a void of 2 cm was left between the entrance of the catalyst and the front-heat-shield (§ par. 2.3), so this was not the case of the best insulated reactor. Therefore, the heat dispersion reduced the hot-spot measured in the inlet section. Furthermore the model accounted for the presence of an inert portion (20% of the active length) of support prior to the catalytic bed. Thus it is not surprising that the model predicted higher temperatures for both phases at the entrance of the catalyst. Notwithstanding this difference, the composition profiles were in close agreement with the experimental evidence. In fact the calculated O_2 conversion was complete within 5 mm and

CH_4 conversion was predicted to reach the equilibrium within a longer monolith portion. The distribution of the product was also nicely described.

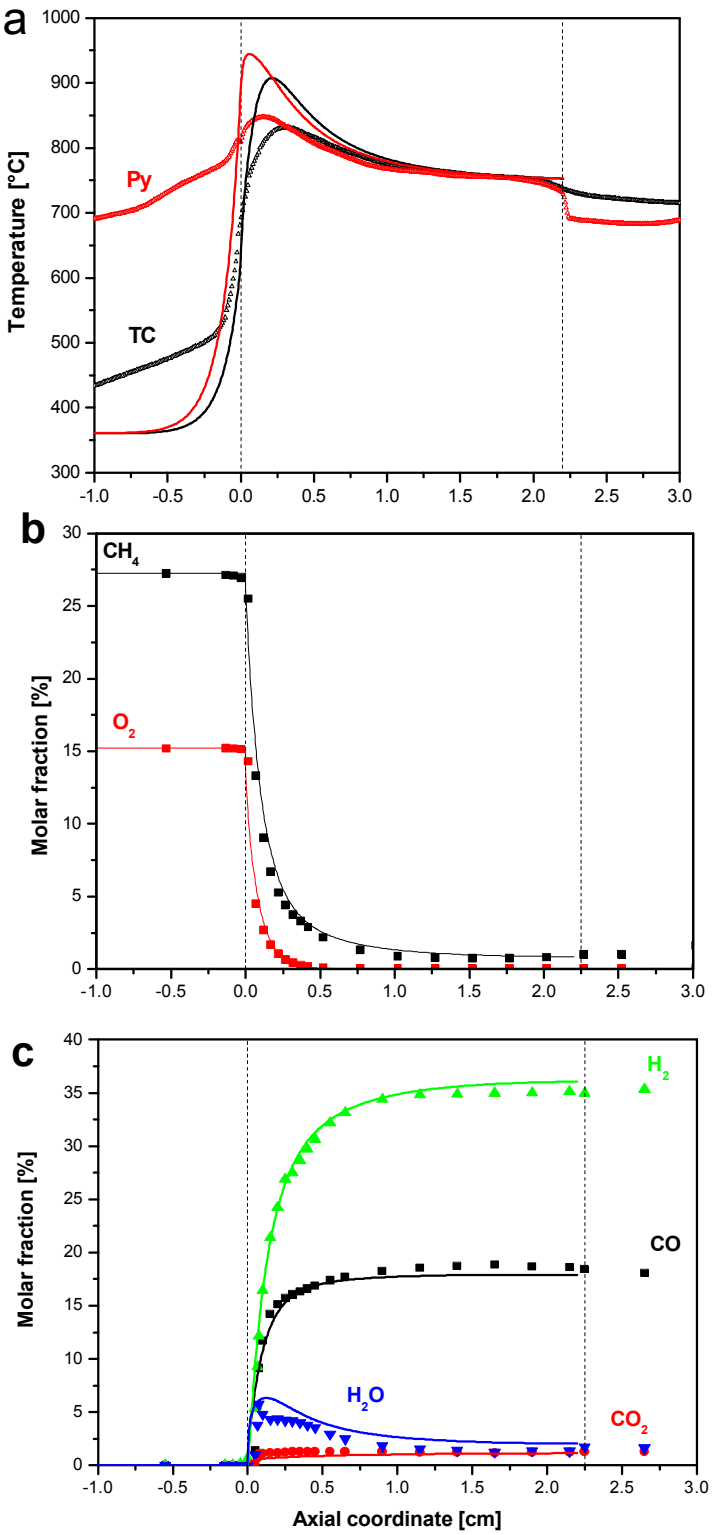

Figure 5.1: Axial temperature profiles measured by thermocouple, TC, and by pyrometer,Py (a); concentration profiles of the reactants (b); concentration profiles of the products (c). Reference honeycomb monolith, Sample 1. Operating conditions: preheating, CH_4/Air mixture, 0.56 O_2/CH_4 , 10 Nl min^{-1} flow rate, atmospheric pressure. Symbols: experimental measurements. Solid lines: model predictions.

The predictions of the model allowed to know the axial profiles of the species at the catalyst wall. The oxygen and methane profiles, which are reported in Figure 5.2, are particularly interesting.

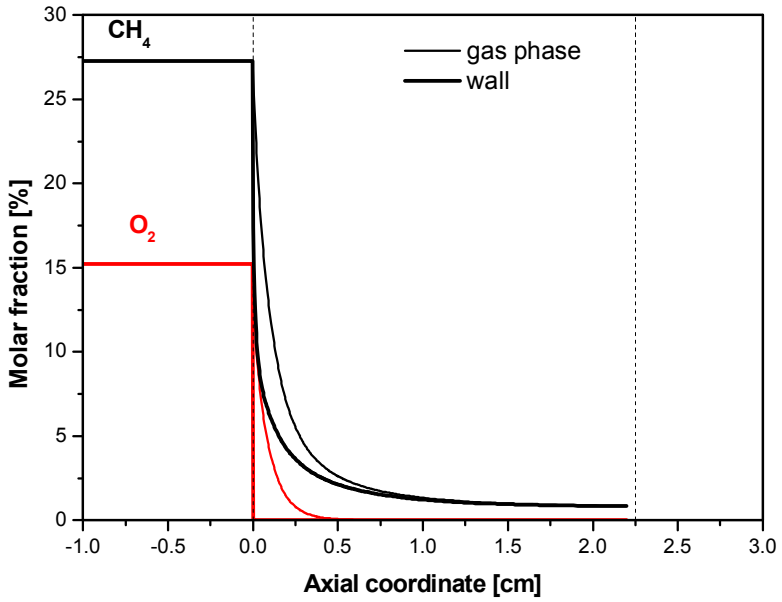

Figure 5.2: Model predictions for the concentration of the reactants in gas phase and at the catalyst wall. Reference honeycomb monolith, Sample 1. Operating conditions: preheating, CH_4/Air mixture, 0.56 O_2/CH_4 , 10 Nl min^{-1} flow rate, atmospheric pressure.

Figure 5.2 showed that the calculated concentration of O_2 at the wall dropped to zero at the very inlet of the catalytic monolith. This is an evidence that the O_2 consumption was fully controlled by external mass transfer because of the extremely high rate of the reaction steps consuming O* species. The most important consequence of the diffusion controlled conversion of O_2 is that the surface coverage is practically zero, and the activation and the consumption of methane occurs through a pyrolitic route (the abstraction of the H* from CH_x is not oxygen assisted). The methane concentration at the surface was noticeably also lower than in the bulk gas phase, but the effect was much less than for oxygen. This suggests the consumption of the methane is kinetically controlled by surface chemistry.

The thermal efficiency (α) calculated is 0.93, therefore nearly adiabatic conditions were realized.

5.3 OPTIMIZATION STRATEGIES

The model and the spatial sampling technique are highly informative tools that allow to characterize the behaviour of the system not only with the outlet temperature and composition, but also with axial profiles, which are very important because the system is characterized by very sharp gradients. In fact, the heat released due to the rapid O_2 conversion in the oxidation reactions, is concentrated in the inlet section causing the

occurrence of a hot spot in the temperature profiles, whereas the heat consumption for the reforming reactions, which form the syngas, involves the whole catalyst bed. Various studies have shown that it is important to minimize the hot-spot: the experimental evidence suggests that surface temperatures below 1000 °C are needed for preventing catalyst deactivation and extremely dangerous autocatalytic overheating. Since O_2 conversion is kinetically controlled by gas-solid diffusion, while methane conversion is more kinetically controlled by the surface chemistry, the channel opening and the catalyst load are expected to be sensitive design parameters which can in principle modify the thermal behaviour of the reactor. In the fallowing sections, the effect of these parameters will be investigated, first under standard conditions.

5.3.1 EFFECT OF CATALYST LOAD

The standard monolith was compared with the behaviour of two other monoliths: Sample 2 and Sample 3. Sample 2 is a honeycomb monolith with 400 CPSI density cell and a catalyst load of 720 mg corresponding to a washcoat layer thickness of 29 μm (§ par. 2.6.4). While Sample 3 is a honeycomb monolith with 400 CPSI density cell and a catalyst load of 935 mg corresponding to a washcoat layer thickness of 43 μm (§ par. 2.6.4). The axial temperature profiles obtained by application of the spatial sampling technique are reported in Figure 5.3.

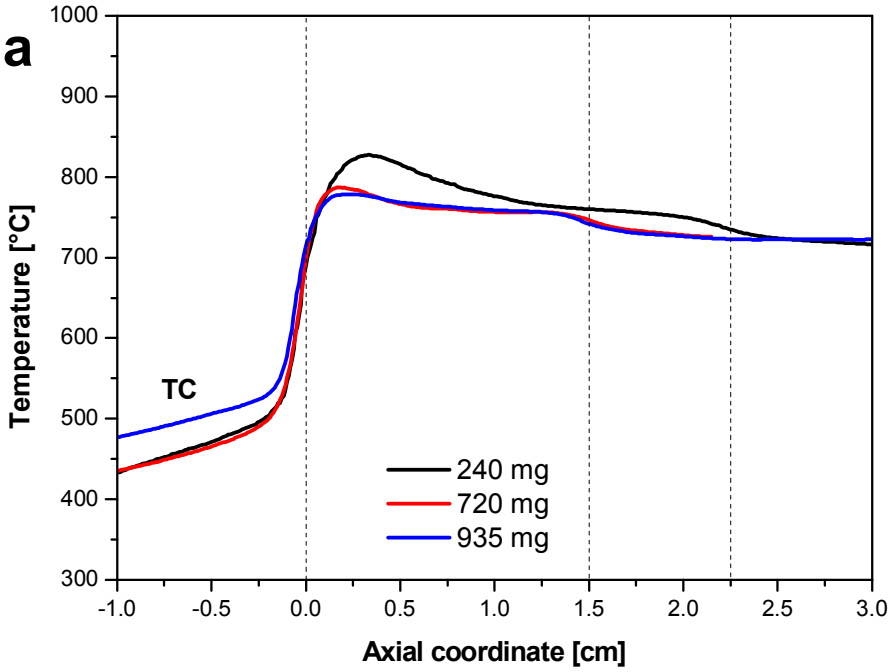

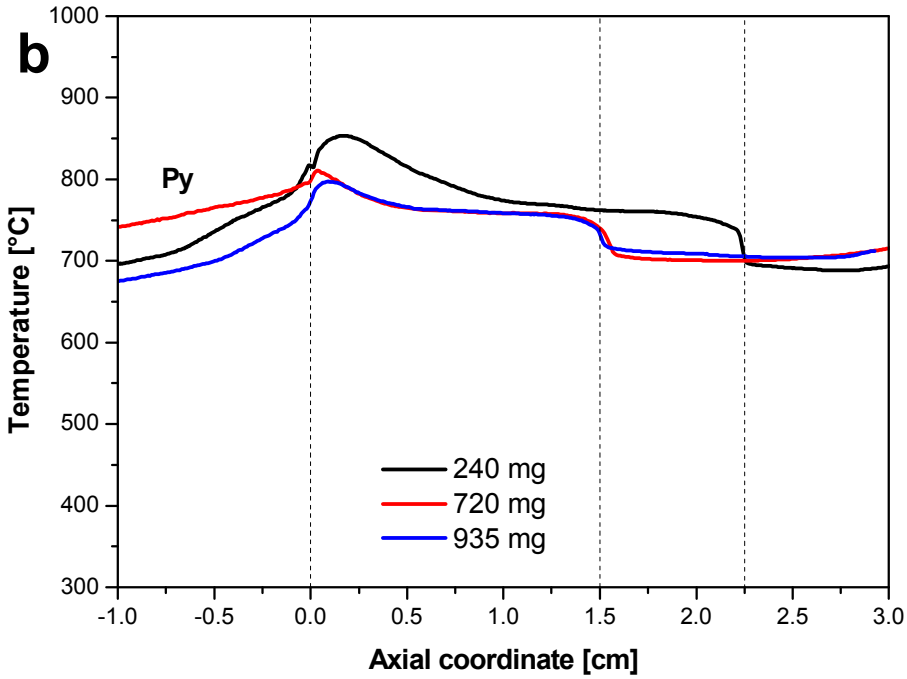

Figure 5.3: Temperature profiles for gas phase (a) and for the solid phase (b) at different catalyst load. Reference honeycomb monolith, Sample 1. Operating conditions: preheating, CH_4/Air mixture, 0.56 O_2/CH_4 , 10 Nl min^{-1} flow rate, atmospheric pressure.

The temperature profiles of solid and gas phase show that at increasing catalyst load the hot-spot at the inlet section reduced. As shown, there was a great effect passing from the standard monolith to the monolith with a load of 720 mg (Sample 2) by the fact that the maximum temperature measured was lower of about 50 °C. The effect on the hot-spot was more limited between the catalyst with load of 720 mg and that of 935 mg. In fact, this further increase reduced the maximum temperature of only 10°C for both the phases. The temperature profiles downstream of the hot-spot were flat and with the same value, suggesting that the thermodynamic equilibrium was reached. The values of the maximum temperatures measured by thermocouple and pyrometer at different catalyst load are reported in Table 5.1.

Catalyst load [mg]	T_{gas} [°C]	T_{solid} [°C]
240	827	854
720	786	811
935	779	797

Table 5.1: Values of maximum temperatures measured by thermocouple and pyrometer for the gas and solid phase, respectively, for catalysts with load of 240, 720, 935 mg.

The concentration profiles were also measured and are reported in Figure 5.4 and 5.5.

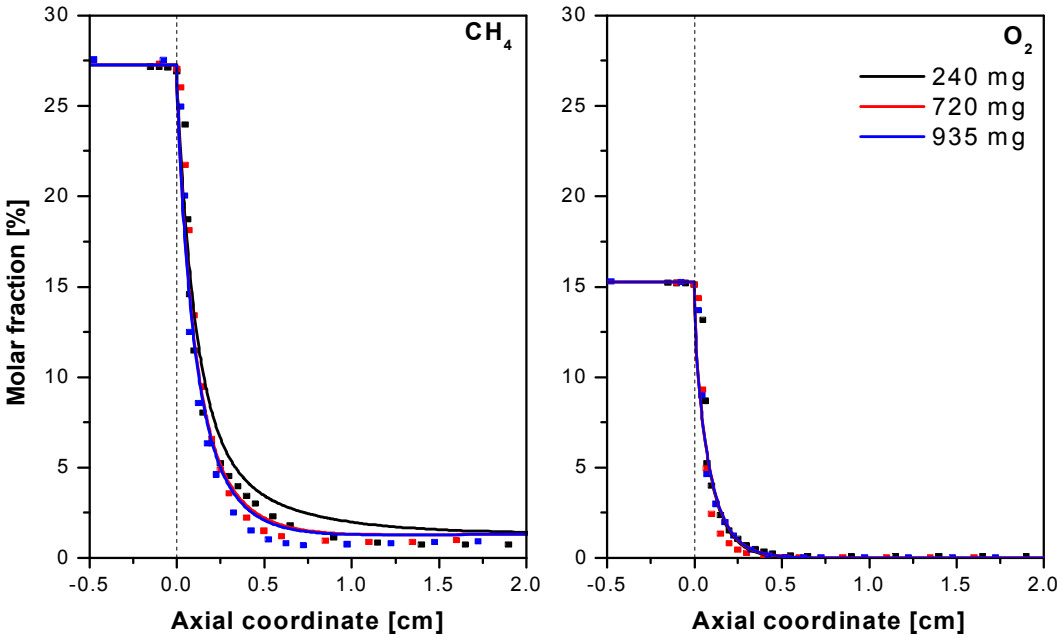

Figure 5.4: Composition profiles of the reactants at varying the catalyst load. Operating conditions: preheating, CH_4/Air mixture, 0.56 O_2/CH_4 , 10 Nl min^{-1} flow rate, atmospheric pressure. Symbols: experimental measurements. Solid lines: model predictions.

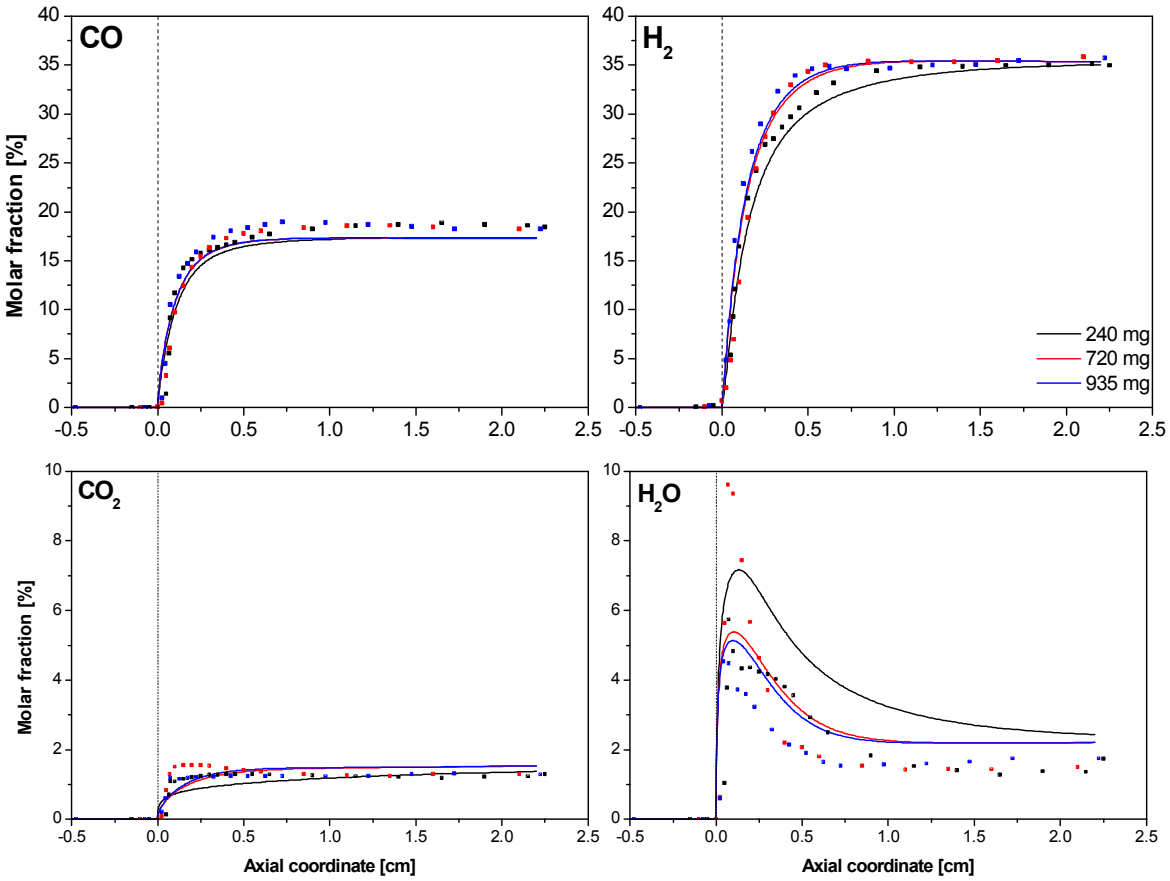

Figure 5.5: Composition profiles of the products at varying the catalyst load. Operating conditions: preheating, CH_4/Air mixture, 0.56 O_2/CH_4 , 10 Nl min^{-1} flow rate, atmospheric pressure. Symbols: experimental measurements. Solid lines: model predictions.

Figure 5.4 shows that at increasing the catalyst load there was only a minimal variation of the rate of oxygen consumption, while there was an appreciable increase of the rate of methane consumption, especially passing from the standard monolith to that with a load of 720 mg. At the end of the catalyst the same conversion of methane was measured in all cases and corresponded to the equilibrium. The increase of the methane conversion in the zone of oxidation caused also an increase of the production of synthesis gas (Figure 5.5). Therefore the greater consumption of methane in the inlet oxidation zone of the catalyst at high load was due to the reaction of steam reforming, which produced synthesis gas.

Figure 5.4 and 5.5 show also the model predictions. The calculated consumption of oxygen was not influenced by the catalyst load and this further evidenced that the consumption of oxygen is controlled by external mass transfer. Instead, the rate of methane consumption increased with high load, because the reforming reactions are favoured and this underlines that the methane is controlled by surface chemistry, which is associated to the reactivity of the catalyst and therefore to the load. In fact at 0.5 mm the conversion of methane for the reference honeycomb was about 89%, while for the catalyst with the highest load (Sample 3) it was about 95%. It is also interesting to observe the profile of water: upon increasing the load, the maximum shifted towards the entrance of the catalyst and its value decreased. This is due to the fact that water is a reactant in the reaction of steam reforming. So if steam reforming is favoured at the inlet of reactor by using a catalyst with high load, the consumption of the water increases. Besides, since the steam reforming is an endothermic reaction, there is a balance between the heat released by oxidation reaction and that consumed by steam reforming, so that a reduction of the hot spot occurs, as shown in Figure 5.6.

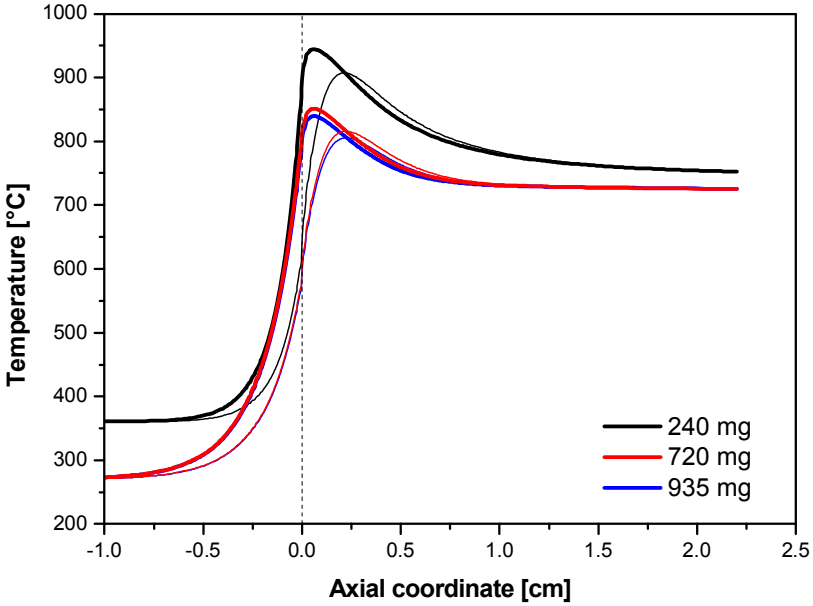

Figure 5.6: Temperature profiles of the solid and of the gas phase with catalyst load of 240, 720, 935 mg. Operating conditions: preheating, CH_4/Air mixture, 0.56 O_2/CH_4 , 10 Nl min^{-1} flow rate, atmospheric pressure. Thin solid lines: gas temperature. Solid lines: surface temperature.

Figure 5.6 shows that the model was able to predict the great effect described when passing from the standard monolith to the catalyst with a load of 720 mg; instead, when passing from 720 mg to 935 mg catalyst load, the effect was minimal. This was due to the fact that the kinetic effect of the increase of the load is compensated and possibly it is also due to a saturation effect of the heat which must be consumed. Therefore, under this conditions the optimal catalyst was Sample 2 because a further increase of the load did not produce significant benefits.

Overall, the principal effect of increasing of the load was to favour the steam reforming reaction in the inlet zone of the reactor so that a higher consumption of the heat released by oxidation reaction, thus reducing the hot-spot. In fact, by increasing almost three times the load of Rh in the reactor, the inlet rate of methane consumption by steam reforming was increased and there was a reduction of ~ 50°C of the hot-spot for both phases. In contrast, the catalyst load had no effect on the rate of O_2 consumption because it was controlled by external mass transfer. Therefore, the increase of load could not influence the oxygen profile.

Finally, the performance of the three different catalyst are reported in Table 5.2 in terms of methane and oxygen conversion, yield to syngas and thermal efficiency.

Catalyst load [mg]	χCH_4 [%]	χO_2 [%]	σH_2 [%]	σCO [%]	T_{out} [°C]	α
240	92.32	99.95	93.88	91.61	723	0.94
720	93.09	99.78	94.36	92.15	730	0.97
935	92.42	99.91	94.19	92.01	726	0.93
Equilibrium	93.77	100	94.35	92.19	731	-

Table 5.2: Performance of catalysts at different loads.

The Table 5.2 shows that upon increasing the catalyst load there is a moderate increase of methane conversion and of yield to synthesis gas, but the principal effect involves the methane conversion inside the reactor, which can be evaluated through the model predictions and by applying the spatial sampling technique. The thermal efficiency showed that the system was not perfectly adiabatic.

5.3.2 EFFECT OF CHANNEL OPENING AND CATALYST LOAD

Previously, it has been observed that the rate of O_2 consumption is not influenced by the catalyst load, so if we want to decrease the rate of the oxidation reactions it is necessary to modify other parameters of the catalyst. Previous model simulations showed that the enlargement of the channel opening can reduce the local rate of O_2 consumption, while it affects to a lesser extent the rate of CH_4 consumption. For this reason, a catalyst with higher channel opening was tested under standard conditions. We characterize the

performance of a honeycomb monolith Sample 5 (§ par. 2.6.4) with 115 CPSI cell density and a catalyst load of 750 mg corresponding to a washcoat layer thickness of 30 µm (§ par. 2.6.4). The load is about three times the catalyst load of the standard monolith described in previous paragraph. The measured profiles of temperature and composition obtained with spatial sampling technique are reported in Figure 5.7.

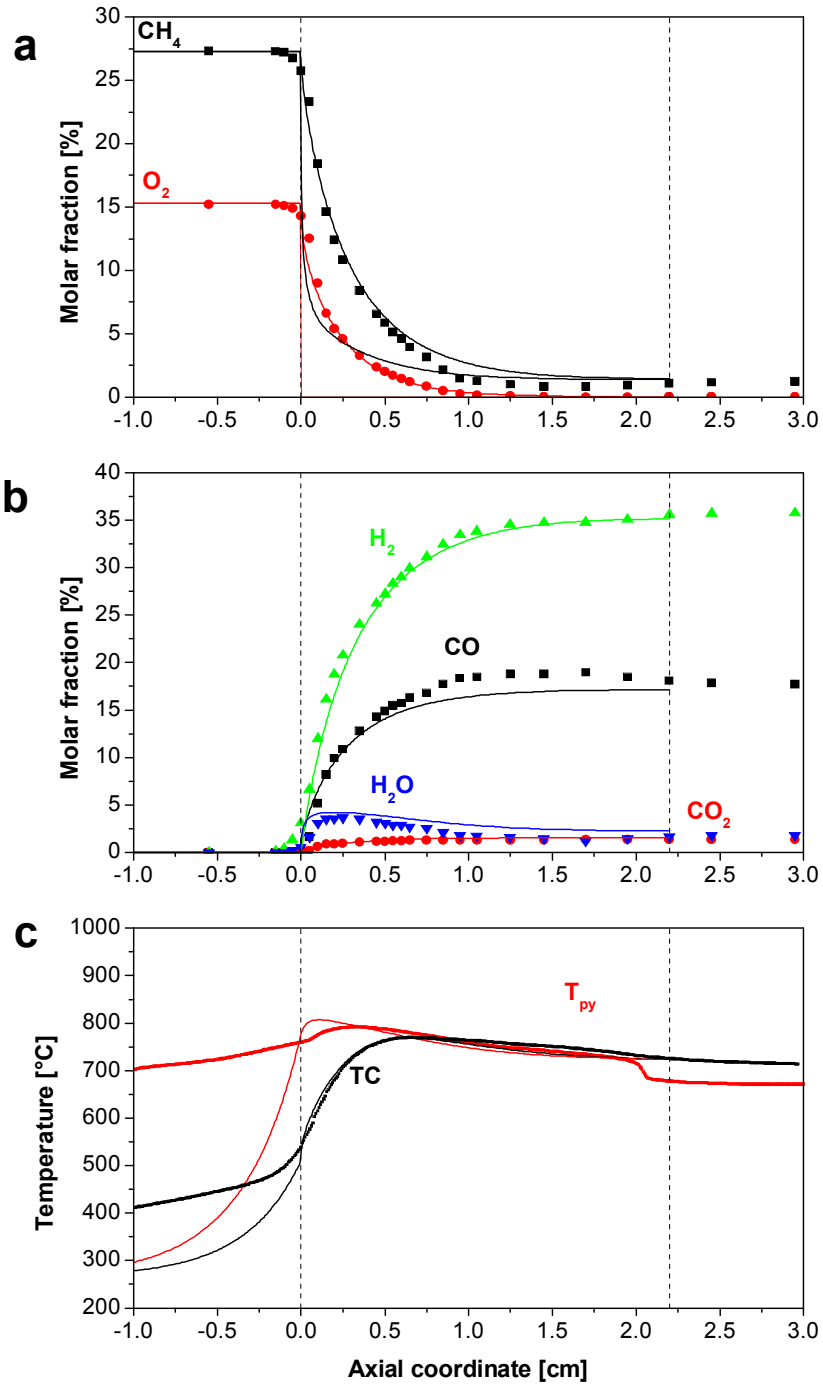

Figure 5.7: Concentration profiles of the reactants (a); concentration profiles of the products (b); axial temperature profiles measured by pyrometer,Py, and by thermocouple, TC (c). Sample 5. Operating conditions: preheating, CH_4/Air mixture, 0.56 O_2/CH_4, 10 Nl min^{-1} flow rate, atmospheric pressure. Symbols: experimental measurements. Solid lines: model predictions.

The measured composition profiles (Figure 5.6) indicated that in the sample the O_2-consumption length increased significantly, passing from 5 mm to 10 mm. Model predictions, also reported in Figure 5.6 as solid lines, described very nicely the experimental data and showed that the more sluggish trend of O_2 concentration profile was completely explained by the reduced rate of gas-phase mass transfer in the wider honeycomb channels. At the same time, the increased amount of catalyst load in the reactor kept high the conversion rate of CH_4, the syngas yield and the heat consumption rate. As a final result, the measured and predicted temperature profiles on the catalysis surface and in the bulk phase were dramatically smoother. In fact the hot-spots were 792°C and 767°C for solid and gas respectively.

5.4 PERFORMANCE AT HIGH FLOW RATE

After the study of catalyst design under "standard" conditions, the effects of the catalyst load and of the opening channel were evaluated at higher flow rate. So we tested the same catalysts, previously described, under more and more severe conditions, which are reported in Table 5.3.

Flow rate [Nl min^{-1}]	T_{IN} [°C]
15	350
20	400

Table 5.3: Flow rate investigated.

5.4.1 EFFECT OF THE FLOW RATE FOR THE REFERENCE MONOLITH

We first studied the thermal behaviour of the reference monolith (Sample 1) with standard catalyst load at different flow rate. The measured temperature profiles obtained with the spatial sampling technique are reported in Figure 5.8.

Figure 5.8 shows that at increasing the flow rate, the solid and the gas phase reached higher temperatures. The measured maximum temperature shifted downstream, especially for the gas phase. This shift was due to a decrease in Damkohler numbers of the exothermic and endothermic reactions. The increase in the temperature peak could be attributed to the rise of power density of the reactor because higher quantity of oxygen was processed, while the effect of linear velocity on Sh and Nu numbers was negligible for the honeycomb. At the same time, the increase of the flow rate decreased the contact time, causing the local rate of CH_4 consumption to decrease respect to the rate of O_2 consumption. Therefore the rate of endothermic reforming reactions was reduced and, thus the temperature rise due to the

exothermic reaction was not moderated by the endothermic reaction. In fact at 20 Nl min^{-1} the surface temperature reached 1074 °C.

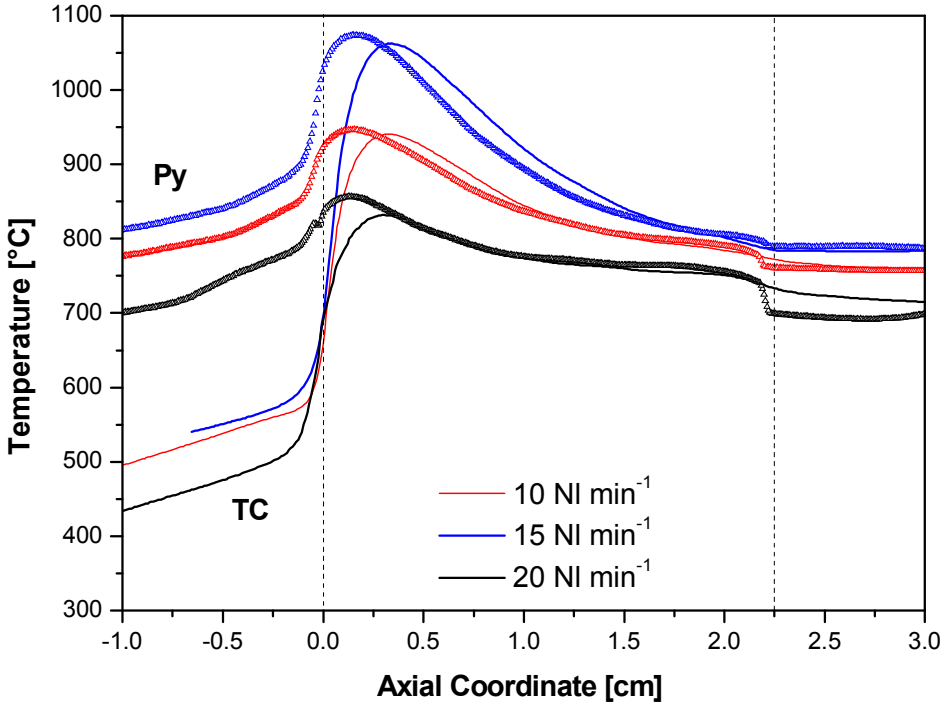

Figure 5.8: Steady-state spatially resolved temperature profiles of the gas and of the solid phase at varying the total flow rate. Reference honeycomb monolith, Sample 1. Operating conditions: preheating, CH_4/Air mixture, 0.56 O_2/CH_4, atmospheric pressure.

The flow rate had also an effect on the temperature profiles downstream of the catalyst. In fact, while for a total flow rate of 10 Nl min^{-1} the temperature profiles became relatively flat downstream of the hot-spot, in case of a total flow rate of 15 and 20 Nl min^{-1} the plateau was absent. This suggests that the thermodynamic equilibrium was not reached. This behaviour was due to the reduction of the contact time which especially influenced the steam reforming reactions, which are controlled by thermodynamic.

Table 5.4 reports the performance of the Sample 1 at different flow rate. Despite the reduction of the contact time, which would lead to a lower methane conversion, there was a moderate increase of CH_4 conversion of methane and selectivity to synthesis gas at high flow rate. This is due to the increased efficiency of the heating cartridges at increasing flow rate. Therefore, the inlet gas temperature also increased from 273°C to 350 for a flow rate of 15 Nl min^{-1} and from 273 °C to 400 °C for a flow rate of 20 Nl min^{-1}. Besides, the thermal efficiency decreased at high flow rate.

Flow rate [Nl min^{-1}]		χCH_4 [%]	χO_2 [%]	σH_2 [%]	σCO [%]	T_{out} [°C]	α
10	Exp	92.32	99.95	93.88	91.61	723	0.94
	Eq	93.77	100	94.35	92.19	731	-
15	Exp	93.15	99.94	94.07	92.71	759	0.91
	Eq	95.65	100	95.23	93.97	756	-
20	Exp	92.88	99.96	93.75	93.08	795	0.9
	Eq	97.04	100	95.36	94.58	776	-

Table 5.4: Experimental steady-state performance for the reference monolith, Sample 1, at varying the total flow rate.

The composition profiles were also collected at 10 and 15 Nl min^{-1} and they are reported in Figure 5.9.

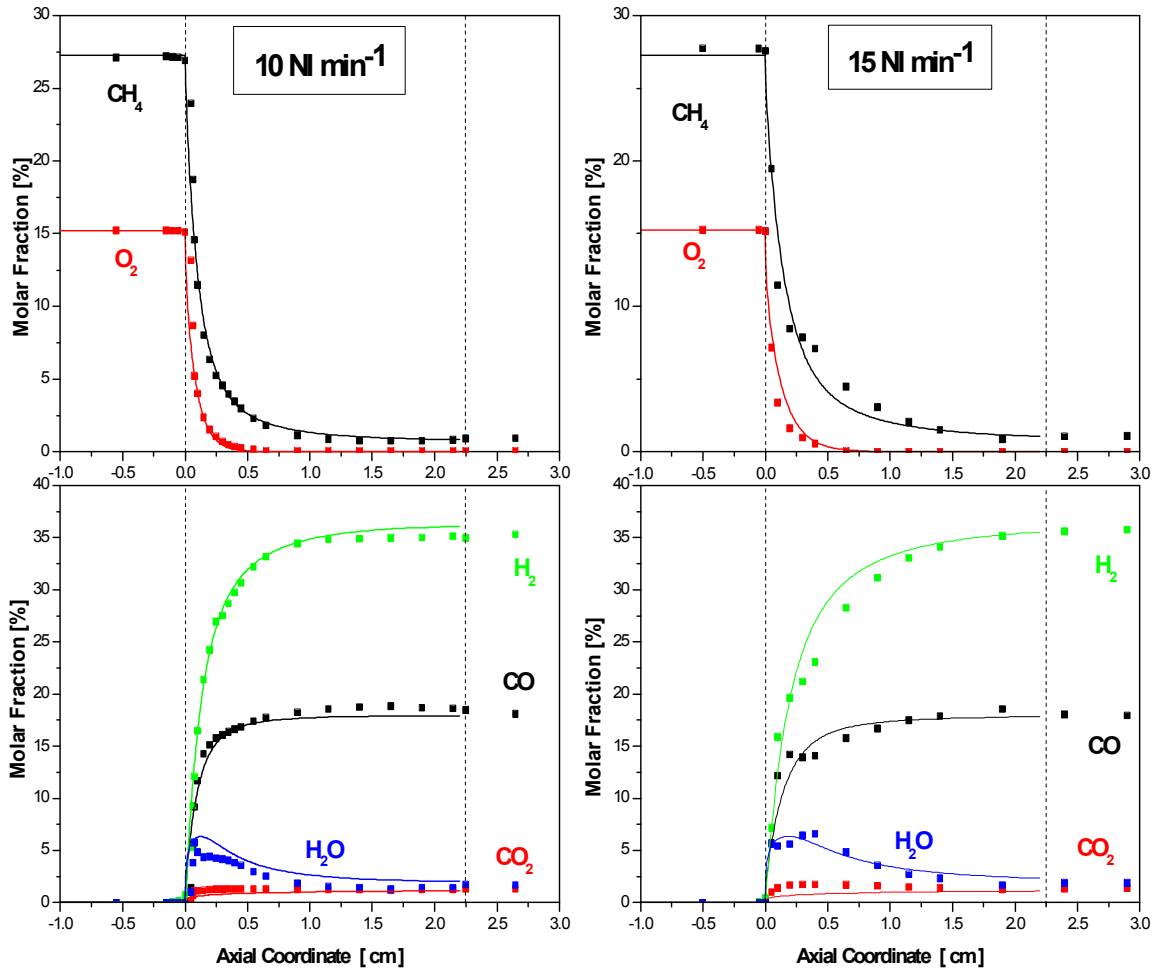

Figure 5.9: Composition profiles of the reactants and the products at 10 Nl min^{-1} (left) and at 15 Nl min^{-1} (right). Reference honeycomb monolith, Sample 1. Operating conditions: preheating, CH_4/Air mixture, 0.56 O_2/CH_4, atmospheric pressure. Symbols: experimental measurements. Solid lines: model predictions.

Figure 5.9 shows that the increase in the flow rate slightly modified the composition profiles. In fact, at increasing the flow rate, the profiles shifted downstream and the oxidation zone became longer. At 15 Nl min^{-1} the oxygen was completely consumed within 7 mm, instead of 5 mm. Besides, the rate of CH_4 consumption is reduced in the inlet zone.

The investigation of the behaviour of the reference monolith at different flow rate underlines that under severe conditions (high flow rate and presence of pre-heating) an optimized catalyst design becomes important. In fact, the surface temperature overcame 1000°C at 20 Nl min^{-1}.Therefore, the single effect of the catalyst load and the combined effect of channel opening and load were investigated also at high flow rate.

5.4.2 EFFECT OF FLOW RATE AT INCREASED CATALYST LOAD

The samples with catalyst loads of 720 (Sample 2) and 935 mg (Sample 3), previously studied under standard conditions, were tested also under severe conditions. The tests were carried out with a methane/air mixture at 0.56 O_2/CH_4 ratio, preheating the reactants and with a total flow rate of 15 and 20 Nl min^{-1}. The axial temperature measured by thermocouple and pyrometer for the catalyst with different loads are reported in Figure 5.10.

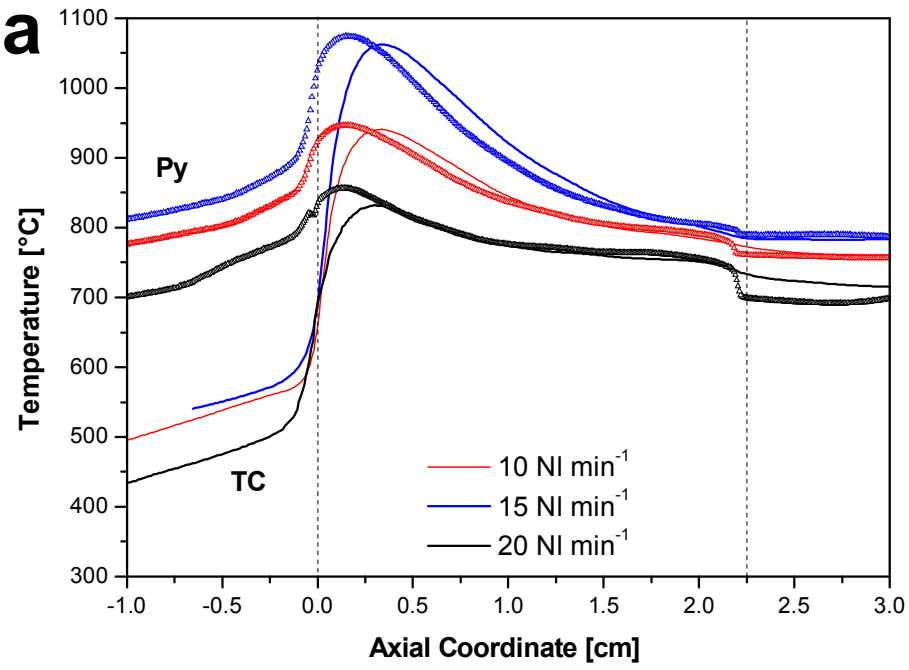

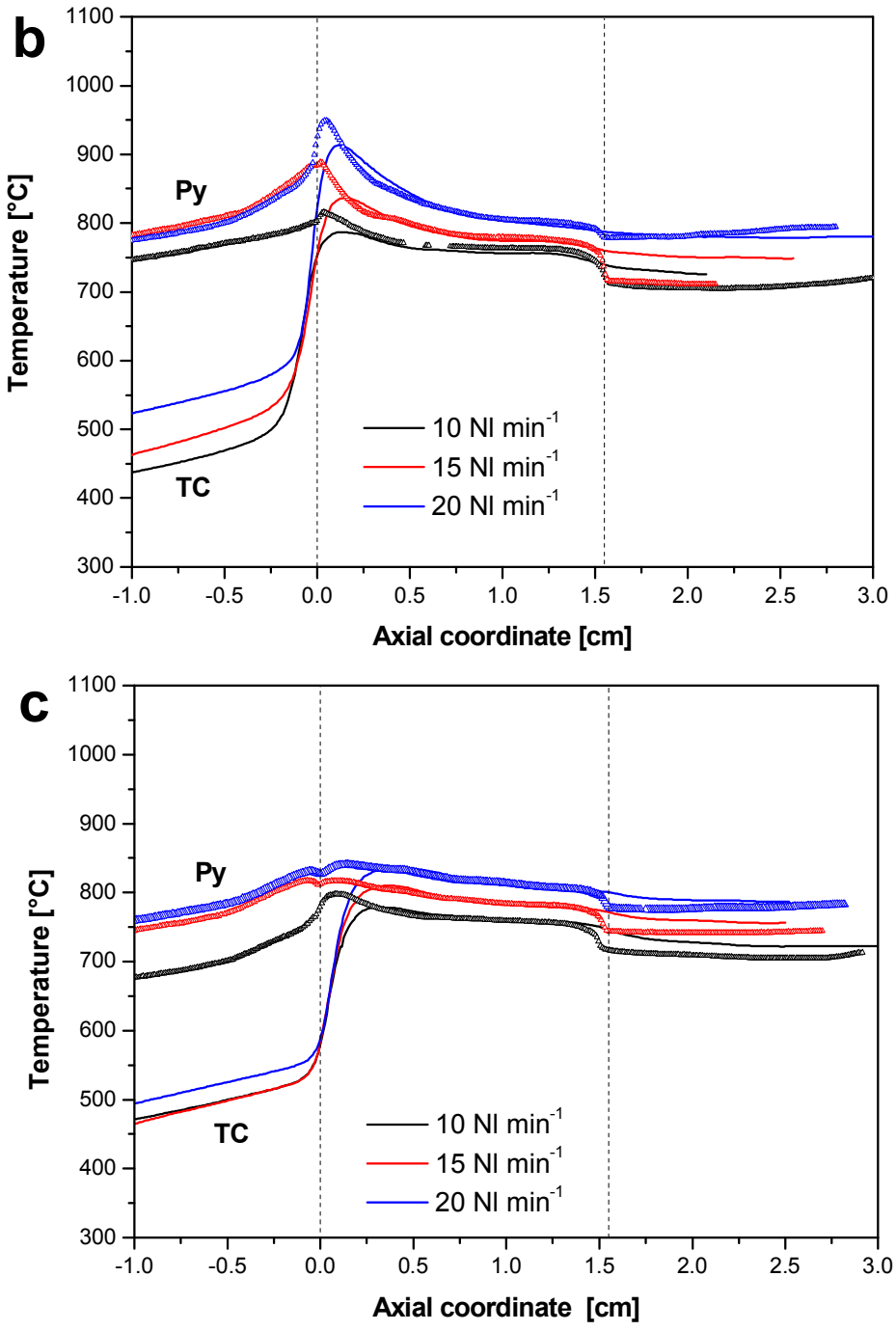

Figure 5.10: Steady-state spatially resolved temperature profiles of the gas and the solid phase at varying the total flow rate for Sample 1 (a), Sample 2 (b), Sample 3 (c). Operating conditions: preheating, CH_4/Air mixture, 0.56 O_2/CH_4, 10 Nl min^{-1}, atmospheric pressure.

In Figure 5.10 the temperature profiles show that, also at high flow rate, increasing the catalyst load caused a reduction of the hot-spot in the inlet section. Differently from the standard conditions, at high flow rates the behaviour of the Sample 2 and Sample 3 was not the same. In fact, the measured temperature profiles for Sample 3 were dramatically smooth (almost gradientless), while for Sample 2 such a considerable hot-spots were still present, even if they were lower than those for the reference monolith (Sample 1). Such a

different behaviour between Sample 2 and Sample 3 at high flow rate was due to the increase of power density of the reactor. The further increase of the catalyst load passing from Sample 2 to Sample 3 favoured the endothermic reforming reactions, which consumed the heat. The temperature profiles showed that only with Sample 3 a balance between the heat released and the heat consumed could be maintained even if at the highest flow rates.

The maximum surface temperature of Sample 3 measured at 20 Nl min^{-1} was 840 °C remarkably lower than that of the "standard" honeycomb (1074 °C). Table 5.5 reports the maximum temperature measured for the solid phase and gas at different conditions of flow rate.

Catalyst load [mg]	Flow rate [Nl min^{-1}]	T_{gas} [°C]	T_{solid} [°C]
240	10	827	854
	15	941	947
	20	1062	1073
720	10	786	811
	15	837	888
	20	913	949
935	10	779	797
	15	810	817
	20	836	840

Table 5.5: Value of the maximum temperature measured of solid and gas phase for catalysts with different load and flow rate.

In light of these results, the catalyst load becomes a very important parameter for the minimization of the hot-spot, especially under severe conditions. In fact, an optimized load allowed to prevent the reaching of the critical surface temperature, which could deactivate the catalyst. In the cases herein studied, we identified the catalyst load which allowed to operate under severe conditions (preheating and high flow rate) without deactivating the catalyst, leading to smooth temperature profiles, lower than the critical conditions.

5.4.3 EFFECT OF FLOW RATE FOR THE OPTIMIZED MONOLITH

Finally, the combined effect of channel opening and catalyst load were evaluated at high flow rate. The operating conditions of these test were: methane/air mixture, O_2/CH_4 ratio of 0.56, preheating and total flow rate of 15 and 20 Nl min^{-1}. The temperature and composition profiles measured whit the spatial sampling technique are reported in Figure 5.11 and 5.12.

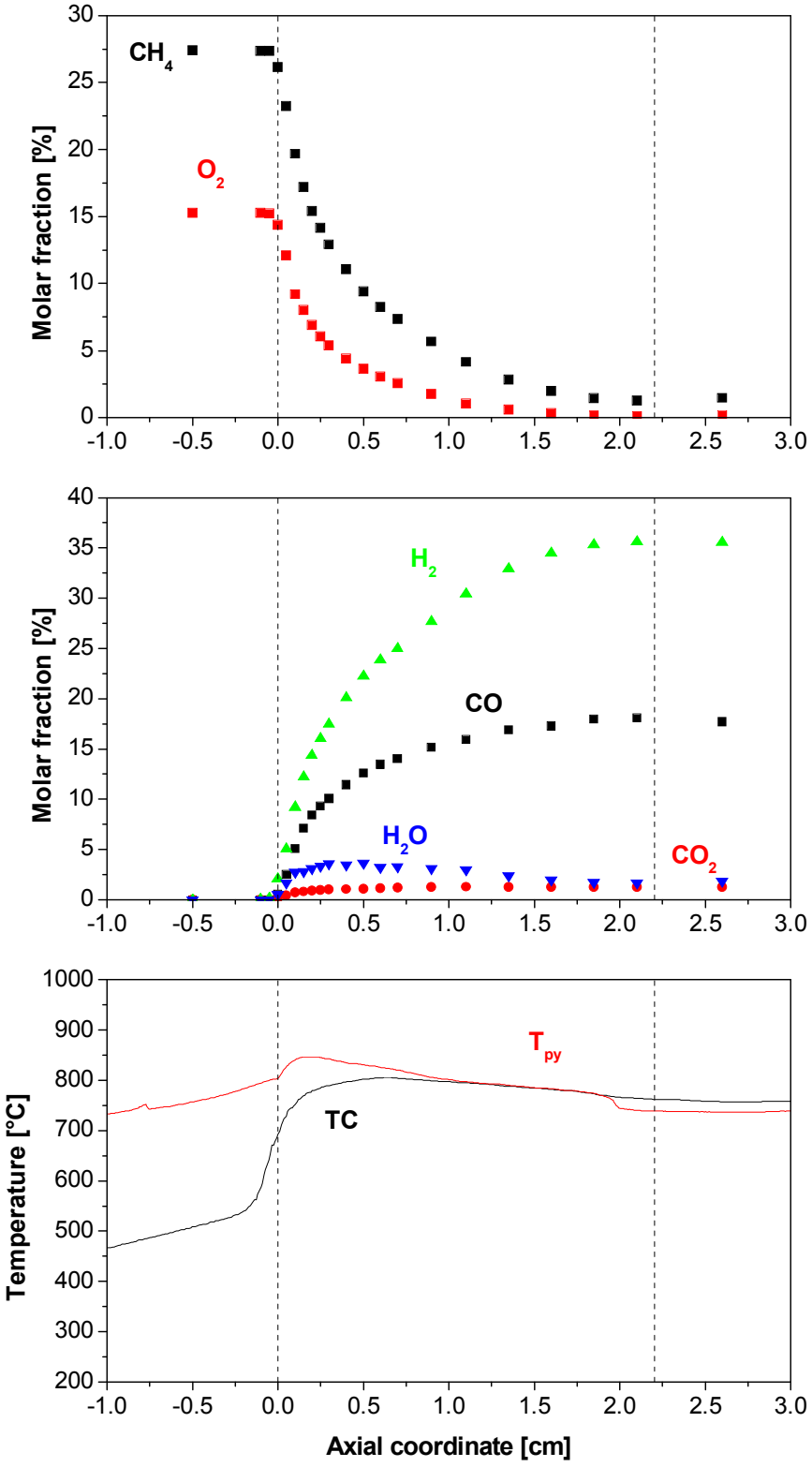

Figure 5.11: Concentration profiles of the reactants (a); concentration profiles of the products (b); axial temperature profiles (c). Sample 5. Operating conditions: preheating, CH_4/Air mixture, 0.56 O_2/CH_4, 15 Nl min^{-1} flow rate, atmospheric pressure. Symbols: experimental measurements. Solid lines: model predictions.

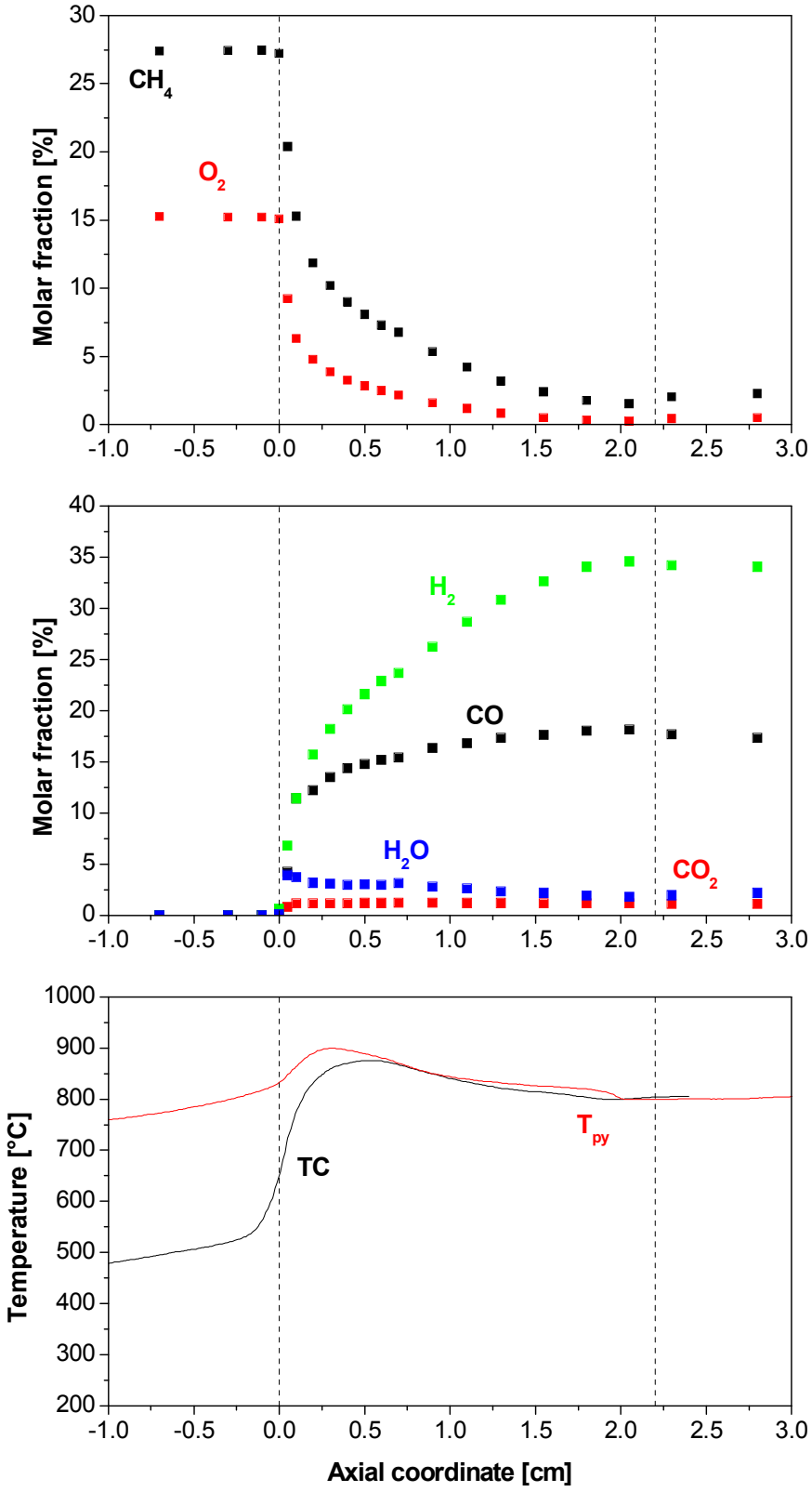

Figure 5.12: Concentration profiles of the reactants (a); concentration profiles of the products (b); Axial temperature profiles (c). Sample 5. Operating conditions: preheating, CH_4/Air mixture, 0.56 O_2/CH_4, 20 Nl min^{-1} flow rate, atmospheric pressure. Symbols: experimental measurements. Solid lines: model predictions.

Also at high flow rate the temperature profiles were smooth and the increase of the maximum temperature was moderate (Table 5.6).

Total flow rate [Nl min^{-1}]	T_{gas} [°C]	T_{solid} [°C]
10	770	792
15	805	847
20	875	797

Table 5.6: Value of maximum temperature measured by thermocouple and pyrometer for the gas and solid phase.

Also in this case, the increase of the flow rate caused an enlargement of the oxidation zone: indeed, at 15 Nl min the oxygen was completely consumed within 1.3 cm from the entrance of the catalyst, while at 20 Nl min^{-1} the oxygen was completely consumed in 1.7 cm.

In Table 5.5 the performances of the catalyst Sample 5 at different flow rate (10, 15, 20 Nl min^{-1}) are reported.

Flow rate [Nl min^{-1}]		χCH_4 [%]	χO_2 [%]	σH_2 [%]	σCO [%]	T_{out} [°C]	α
10	Exp	91.4	99.83	93.89	91.43	723	0.94
	Eq	93.77	100	94.35	92.19	731	-
15	Exp	90.85	99.97	92.72	92.48	754	0.93
	Eq	95.65	100	95.23	93.97	756	-
20	Exp	88.27	100	91.75	92.04	806	0.86
	Eq	97.04	100	95.36	94.58	776	-

Table 5.6: Experimental steady state performance of the tests in CH_4 preheating varying the flow rate. Sample 5.

Increasing the flow rate caused a reduction of the methane conversion and of the yield to synthesis gas.

5.5 CONCLUSIONS

The suppression of surface hot-spots is a prerequisite for the durable and stable operation of short contact time CH_4-CPO reformers. Once recognized the key role of mass transfer limitations on the thermal behaviour of the autothermal reformer, modelling work clearly shows the potential offered by the reactor design. Herein we give the experimental

demonstration that the support geometry and the catalyst activity are sensitive parameters for achieving an optimal thermal behaviour (in principle a gradientless temperature profile). By increasing the channel opening of the honeycomb support and the catalyst load, the inlet rate of the oxidation reactions is decreased and the O_2 consumption length (typically as short as few mm) penetrates well within the monolith while the yield to syngas is preserved. In this way the hot-spot are minimized even if under severe condition.

CHAPTER 6

OPTIMAL REACTOR DESIGN: EFFECT OF FRONTAL HEAT DISPERSIONS

6.1 INTRODUCTION

In the previous chapter the effect of the catalysis design (channel opening and load) on the thermal behaviour of the reactor was studied and an optimized monolith was proposed to minimize the hot-spot in the inlet section. Also other strategies can be adopted to minimize the hot-spot without affecting the global performance in terms of fuel conversion and syngas yields. In this chapter we explored the effect of the reactor configuration and especially the effect of the location of the front-heat shield, which is used in the literature to limit the axial heat losses of the catalyst radiation. The study of the inner configuration was carried out for methane CPO, but also for propane CPO, wherein the extent of temperature gradients and the issue of the catalyst stability where expected to become even more important due to the higher reaction enthalpy compared with CH_4 (-228 vs. -36 kJ mol^{-1}).

Also for this set of tests, as for the tests described in chapter 5, the steady-state behaviour of the reactor was characterized by the measurement of the spatially resolved profiles of temperature and composition and the experimental methane/propane conversion and the yields to synthesis gas were compared with the values obtained by the adiabatic equilibrium. Finally the thermal efficiency of the reactor was experimentally determined and expressed in terms of α which is the ratio between the experimental temperature rise and the theoretical adiabatic temperature rise of the gas phase (see definition § par. 5.1).

6.2 THERMAL BEHAVIOUR OF CH_4 CPO

The CPO tests were performed over 2 wt% Rh/α-Al_2O_3 catalyst deposited onto 400 CPSI cordierite honeycomb with a standard catalyst load. The internal layout of the reactor (§ par. 2.3) consists of a catalytic monolith kept between two uncoated monoliths acting as thermal shields and flow mixer. In order to investigate the role of heat dissipations by radiation at the front face of the catalytic monolith, three different reactor configurations were tested. The thermal behaviour of the reactor and the effect of the front heat shield position was studied under reference operating conditions:
- CH_4/Air mixture at O_2/CH_4 of 0.56 (lightly overstoichiometric);
- total flow rate of 10 Nl min^{-1};

-preheating of the inlet gas stream.

6.2.1 "SEPARATED FHS" CONFIGURATION

In the "separated FHS" configuration (§ par. 2.3), shown in Figure 6.1, the front heat shield and the catalytic honeycomb were kept at a distance of ~ 1.5 cm. The tests were performed with the catalytic honeycomb, Sample 1, whose characteristic are reported in Table 2.3 (§ par. 2.6.4).

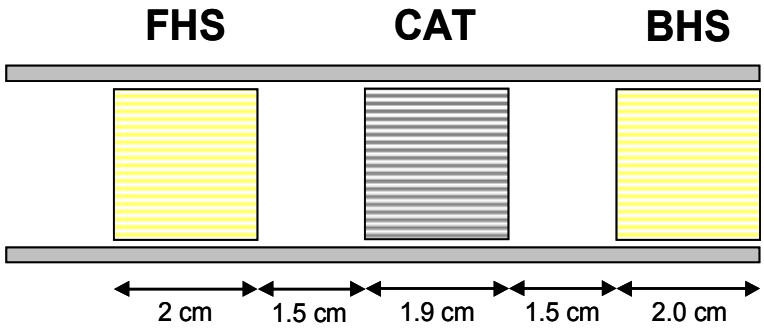

Figure 6.1: "Separated FHS" configuration.

The performances of this configuration under standard operating conditions were described in the previous chapter (§ par. 5.2).

6.2.2 "CONTINUOUS FHS" CONFIGURATION

The "continuous FHS" configuration (§ par. 2.3), shown in Figure 6.2, is such that a perfect continuum between the catalyst and the heat front shield was realized allowing a good insulation of the reactor. This continuity was obtained by adopting a coating procedure wherewith only a portion of the honeycomb support was coated with the catalytic slurry. This monolith, Sample 6, was prepared with the technique described in chapter 2 and its proprieties are reported in Table 2.4 (§ par. 2.6.4).

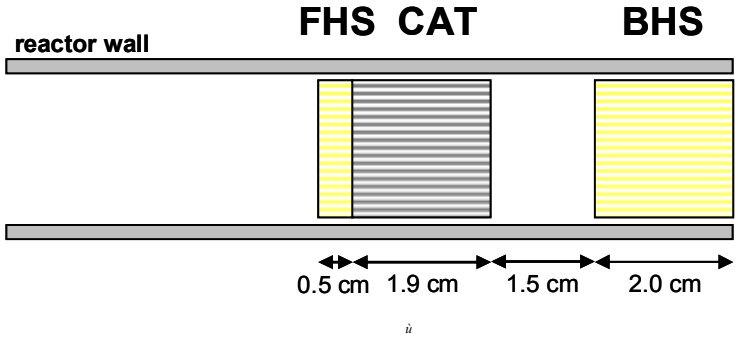

Figure 6.2: "Continuous FHS" configuration.

The measured temperature and composition profiles obtained with the spatially sampling technique are reported in Figure 6.3.

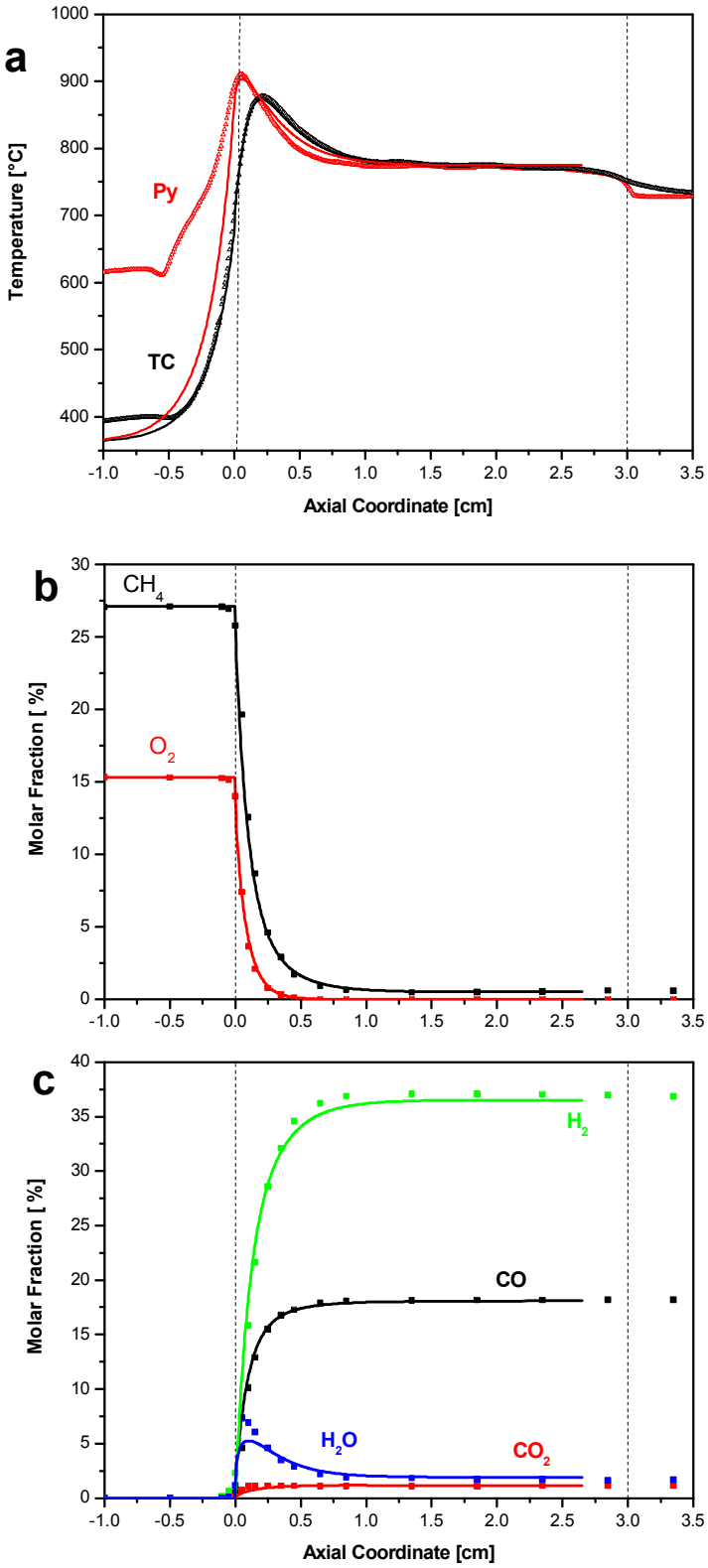

Figure 6.3: Axial temperature profiles (a); concentration profiles of the reactants (b); concentration profiles of the products (c). Sample 6. Operating conditions: preheating, CH_4/Air mixture, 0.56 O_2/CH_4, 10 Nl min^{-1} flow rate, atmospheric pressure. Symbols: experimental measurements. Solid lines: model predictions.

Figure 6.3 a shows the temperature profiles measured by pyrometer (Py) and by the thermocouple (TC), comparing these temperature profiles with those reported in Figure 5.1 it is easily observed that the monolith with continuous FHS exhibited a much sharper hot-spot with a maximum temperature of 910 °C measured by the pyrometer and 870 °C measured by the thermocouple. Cleary, the presence of the continuous FHS better insulated the inner reactor portion and favoured an increased of the local surface and gas-phase temperature. The temperature profiles became flat downstream the hot-spot, suggesting that the thermal equilibrium was reached. Concerning the measured concentration profiles of reactants (panel b), it was found that O_2 conversion was complete within 5 mm from the catalyst entrance. This is a strict analogy with the case of the separated FSH, in Figure 5.1. Also methane was consumed at a great extent within the same short length, at 5 mm the measured methane conversion was about 93%, but it further increased up to 97% a few millimetres downstream. The measurement of the product composition show that hydrogen and CO were produced from the very entrance and syngas production grew rapidly along the axial coordinate. The activity of the catalyst was certainly high, as shown by the approach to equilibrium at the reactor exit and by the flattening temperature profiles in the second half of the monolith length.

The solid lines in the Figure 6.3 represent the model predictions. The gas and the solid phases were predicted in close agreement with the experimental data. This indicated that the thermal dispersions were minimized through the presence of the inert zone in the monolith which ensures a perfect continuum between the catalyst and the front heat shield and a good insulation of the reactor. These results confirmed that in the "separated FSH" configuration the difference between the measurement temperature and the model prediction of hot-spot was due to the dispersion for radiation from of the front face of the catalytic monolith. Also the distributions of the reactants and products were nicely described.

This configuration was also tested at different flow rates with preheating of the reactant mixture and with autothermal conditions where the reactants were fed at room temperature (§ par. 2.5.2.).

6.2.2.1 TESTS WITH PREHEATING

The thermal behaviour of this configuration was performed with temperature and composition profiles obtained through the spatial sampling technique. The honeycomb monoliths Sample 6 was tested at increasing flow rates (10, 15, 20 Nl min^{-1}).

Figure 6.4 reports temperature profiles of surface and gas-phase. The data show that at increasing load the hot-spot temperatures in the inlet section grew both on the surface and in the gas phase because of the rise of the power density of the reactor.
Besides, there was also a rise of the inlet temperature because of the increasing efficiency of the pre-heating cartridges; and this factor also contributed to increase the temperature at the exit of the reactor at increasing flow rate.

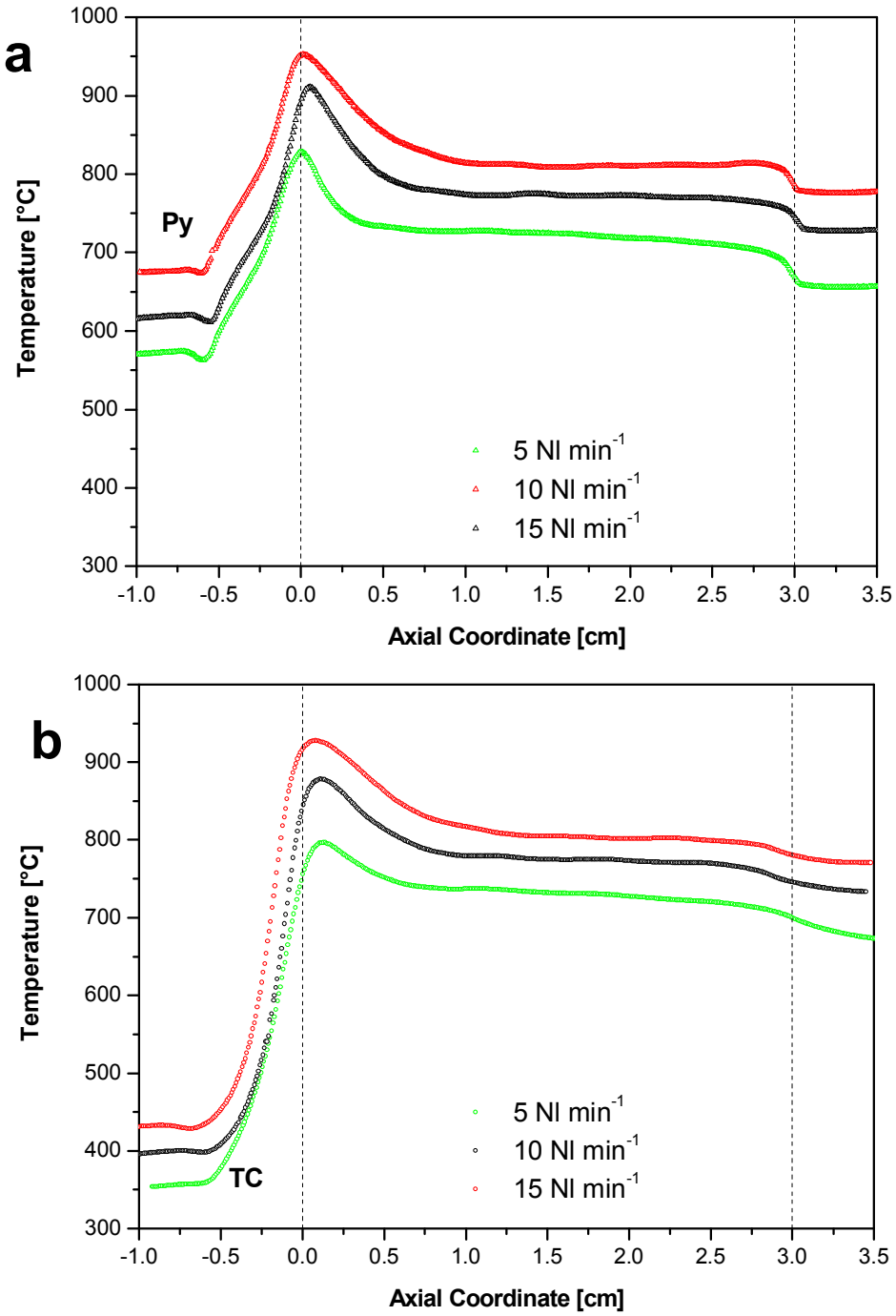

Figure 6.4: Spatially resolved temperature profiles of the gas phase and of the solid phase at different flow rates (5, 10, 15 Nl min^{-1}) for Sample 6. Preheating, mixture CH_4/Air, O_2/CH_4 0.56, atmospheric pressure.

Figure 6.5 shows the predicted temperatures profiles in the gas phase and on the surface. The calculated calculated profiles compare well with the experimental data both on a qualitative and quantitative basis.

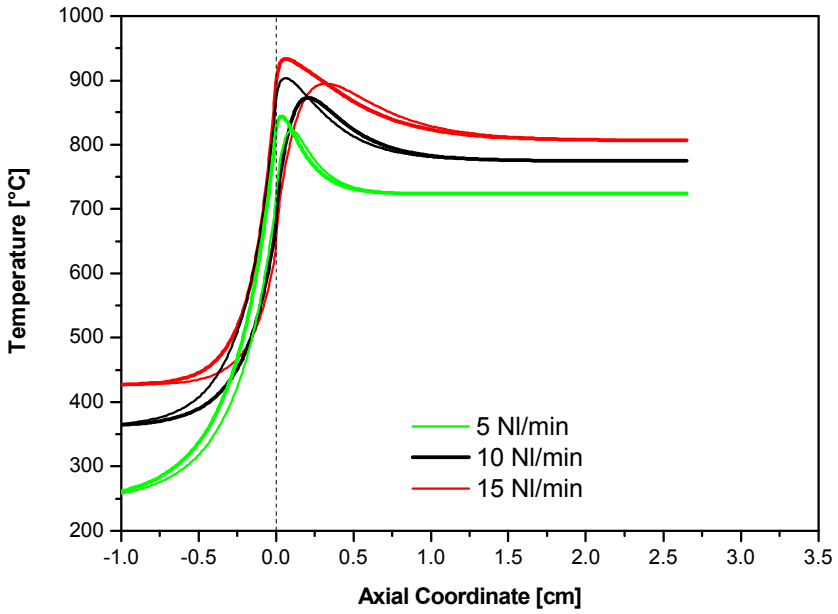

Figure 6.5:Model predictions of temperature profiles of the gas phase and solid phase at different flow rates (5, 10, 15 Nl min^{-1}) for Sample 6.

The experimental profiles and the model predictions indicated that at increasing the flow rates the thermodynamic equilibrium was approached at a greater distance from the entrance of the reactor. Even if at 15 Nl min^{-1} this condition were reached because the catalyst had a length of 3 cm.

6.2.2.2 TESTS UNDER AUTOTHERMAL CONDITIONS

The "continuous FHS" configuration was also tested under autothermal conditions (§ par. 2.5.1) where the reactant mixture was fed at room temperature through the by-pass of the heating system, as it was described at chapter 2. This configuration was tested at different flow rates: the experimental measured temperature obtained through the spatial sampling technique are reported in Figure 6.6.

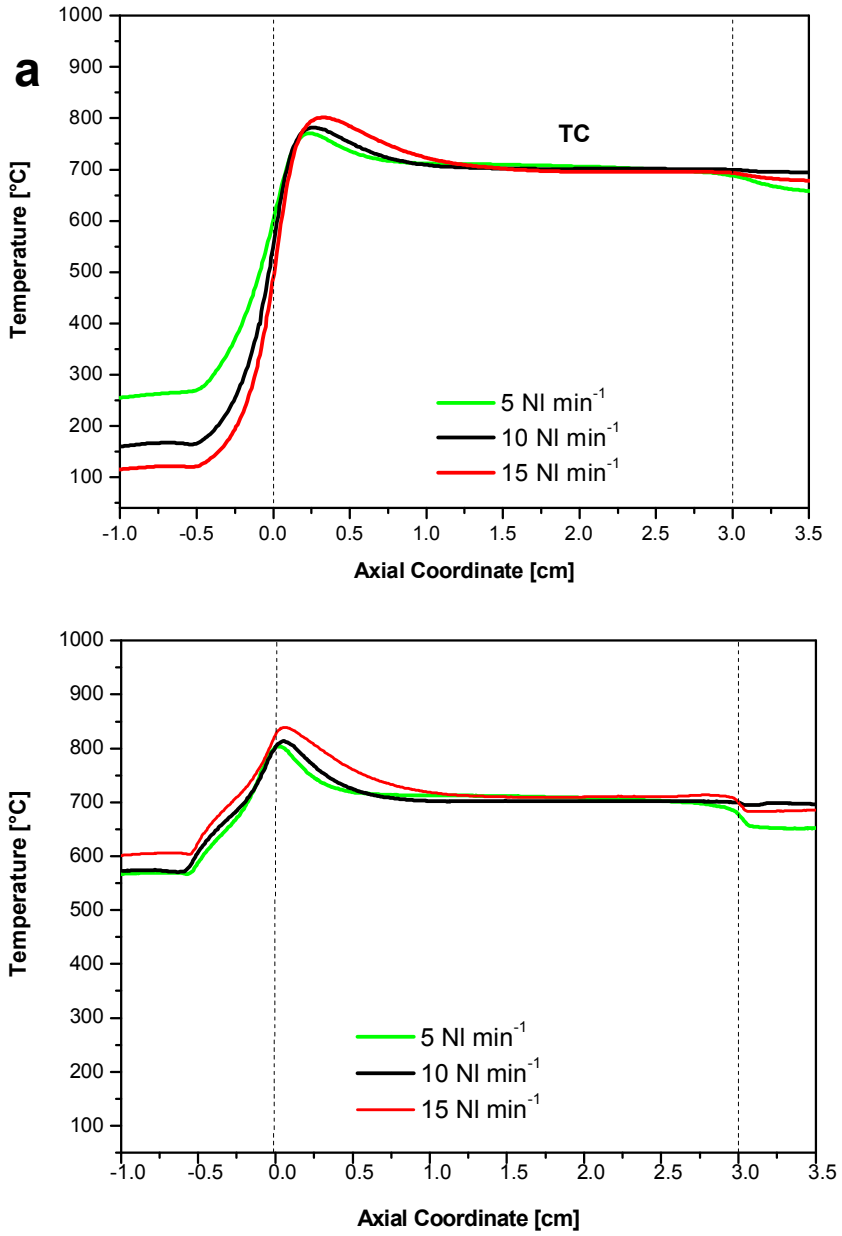

Figure 6.6: Spatially resolved temperature profiles of the gas phase(a) and of the solid phase (b) at different flow rates (5, 10, 15 Nl min^{-1}) for Sample 6. Preheating, CH_4/Air mixture, O_2/CH_4 0.56, atmospheric pressure.

The effect of the flow rate is less emphasized under autothermal condition than in the conditions with preheating, even if qualitatively the effect is the same.

6.2.3 "WITHOUT FHS" CONFIGURATION

In the configuration "without FHS" (§ par. 2.3), shown in Figure 6.7 , the thermal heat shield was reduced in length and located several centimetres upstream of the catalyst. The tests were performed with the standard catalytic honeycomb, Sample 4, whose characteristics are reported in Table 2.3 (§ par. 2.6.4).

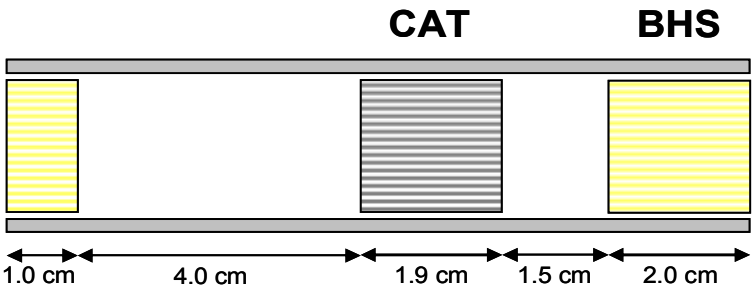

Figure 6.7: "Without FHS" configuration.

This configuration was tested only for the test under standard operating conditions and the temperatures profiles obtained are reported in Figure 6.8.

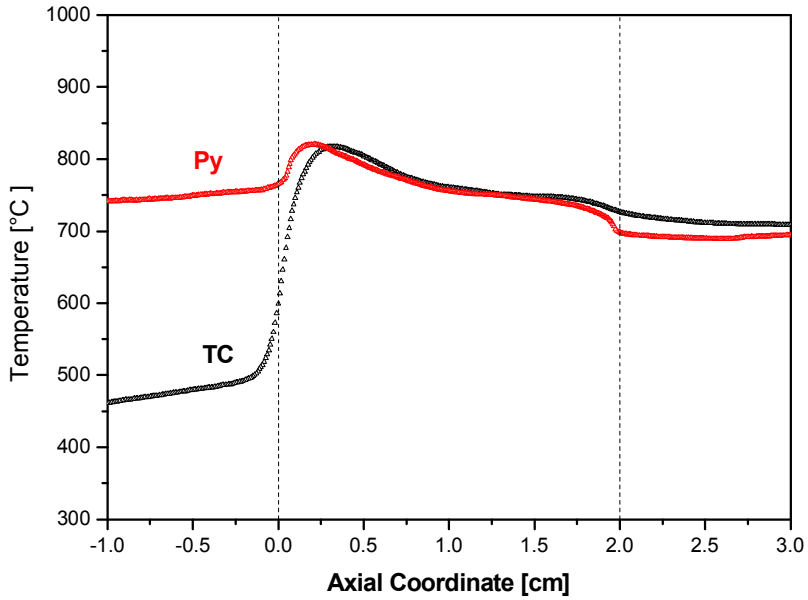

Figure 6.8: Spatially resolved temperature profiles for Sample 4. Operating conditions: preheating, CH_4/Air mixture,0.56, O_2/CH_4, 10 Nl min^{-1} flow rate, atmospheric pressure.

The temperature profile indicates the presence of the hot-spot in the inlet section for gas and solid phase, even if the they were not marked. The optical pyrometer showed a maximum temperature of about 821 °C while the sliding thermocouple measured a maximum temperature of about 817 °C. The temperature profiles reached downstream of the hot-zone an asymptotic trend, clearly showing the approach to the thermodynamic equilibrium.

6.2.4 COMPARISONS

In the series of configurations analyzed, the "continuous FHS" configuration represents the reference case of the best insulated reactor. It was however expected that passing to the configurations with "separated FHS" and then "without FHS", that is passing to configurations with increased extension of the walls that surround and receive the radiation

from the glowing front face of the catalytic module, heat dispersions from the reactor would have been enhanced. Figure 6.9 reports the axial temperature profiles measured by pyrometer and the thermocouple (symbols) for the three reactor configurations above described. Model calculations of the solid and gas phase temperature (solid line) for the configuration with the continuous FHS configuration are also plotted. The measured and calculated conversion and selectivity were reported for the three configurations in Table 6.1.

	χ CH_4 [%]	χ O_2 [%]	σ H_2 [%]	σ CO [%]	T_{OUT} [°C]	α
Continuous FHS	97.1	100.0	95.0	94.1	770	0.99
Separated FHS	95.4	99.2	95.3	93.3	758	0.95
Without FHS	95.4	100.0	95.0	93.2	747	0.90
Model	97.2	100.0	95.0	94.0	770	1.00
Equilibrium	97.2	100.0	95.0	94.0	772	1.00

Table 6.1: CH_4 CPO, O_2/C = 0.56, 10 Nl min^{-1}, preheated conditions. Comparison between experimental, calculated and thermodynamic outlet performances.

The "continuous FHS" had an extremely high thermal efficiency (α = 0.99). This indicated that the system was completely adiabatic; in fact because of the presence of a continuous inert zone, the heat dispersion was minimized. Also, as shown in Table 6.1, the measured and calculated conversion and selectivity were practically coincident with the expected equilibrium values which support the evidence of a high catalytic activity of the Rh-coated monolith.

In the case of the "separated FHS" configuration the thermal efficiency of the reactor lowered to 95%; a loss of 12°C in the outlet temperature and a very moderate decrease of conversion and selectivity was observed, as shown in Table 1. However, the hot spot temperatures measured by the pyrometer and the thermocouple decreased of ~70°C and ~60°C respectively, indicating that the increased heat dispersions from the front face acted more intensively on the temperatures of the entrance zone of the monolith.

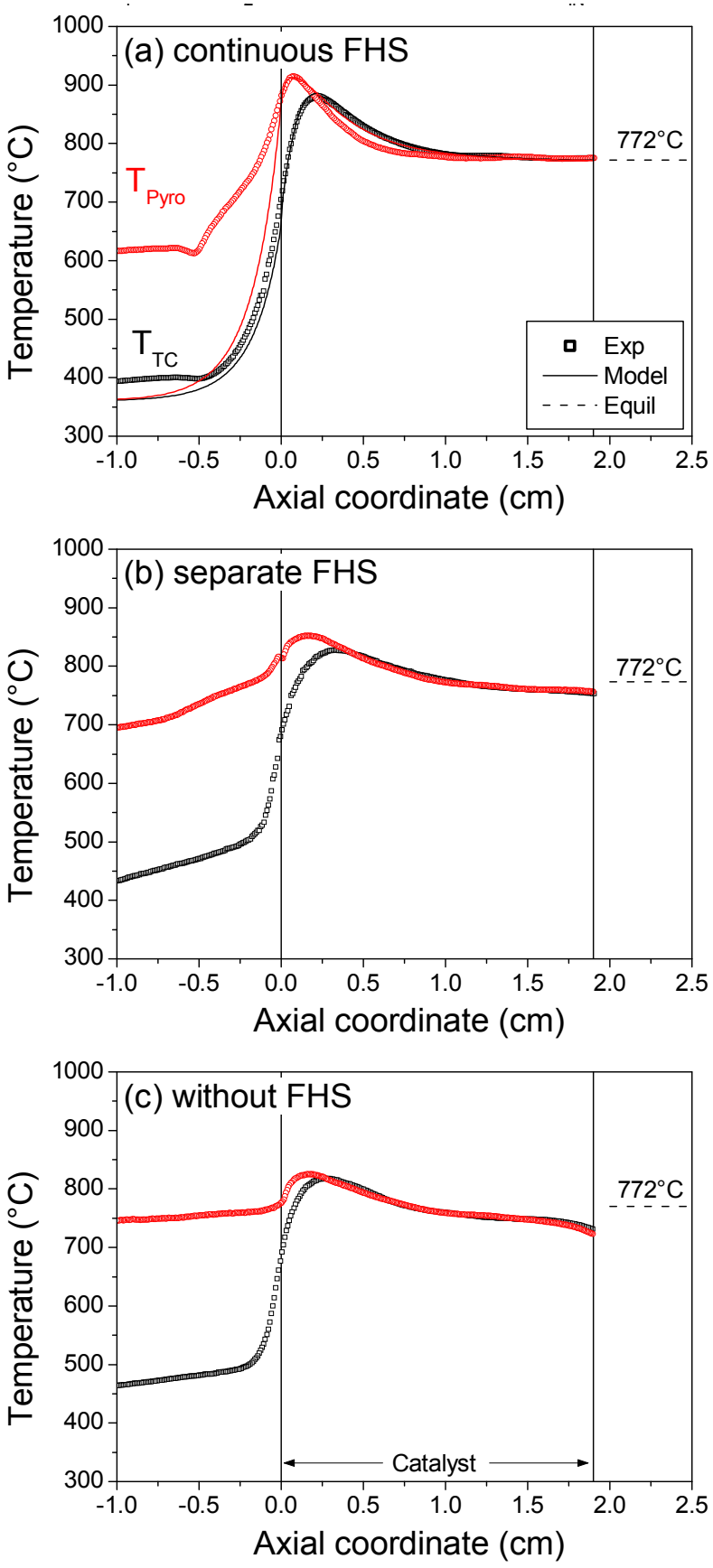

Figure 6.9: Temperature profiles for the three studied configurations. Operating conditions: preheating, CH_4/Air mixture,0.56 O_2/CH_4 , 10 Nl min^{-1} flow rate, atmospheric pressure.

In the limiting case of the configuration "without FHS", the thermal efficiency of the reactor decreased down to 90%, the outlet temperature of the reactor was 23°C below the reference adiabatic exit temperature, while methane conversion kept very high. Still, the measured temperature profiles showed a further reduction of ~25°C and ~10°C of the solid-phase and gas-phase hot spot temperatures, respectively.

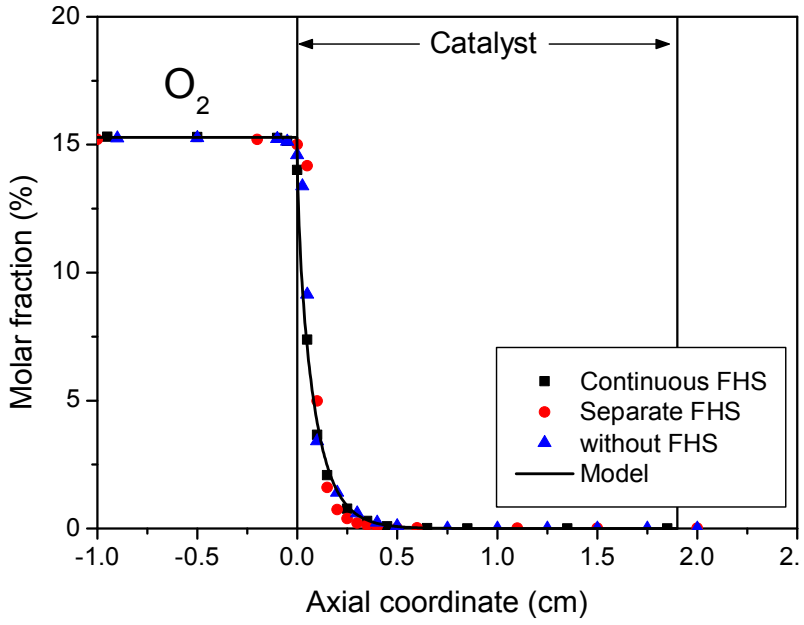

Figure 6.10: Profiles of oxygen for the three studied configurations. Operating conditions: preheating, CH_4/Air mixture, 0.56 O_2/CH_4 , 10 Nl min^{-1} flow rate, atmospheric pressure.

Figure 6.10 reports the measured axial concentration profiles of O_2 in the three experiments, compared with the predicted gas-phase concentration of O_2 for the reference adiabatic reactor. In the three experiments, O_2 consumption showed a similar trend (well explained by the inter-phase mass transfer in the honeycomb channel) and was complete within ~5 mm. This indicates that the enthalpy flow due to the oxidation reactions was released with the same distribution in three configurations. Thus the differences of the thermal behaviour of the reactor were mainly due to the localized heat dissipations associated with the progressive separation of the FHS from the catalyst front face.

Thus, an overall view of the reactor response suggests that the thermal efficiency of FHS has an important impact on the shape of the surface temperature profile inside the catalytic monolith; by reducing such efficiency, we observed a moderate loss of thermal efficiency of the whole reactor, a slight decrease of the syngas yield, but a remarkable moderation of the hot spot temperature.

6.3 PROPANE CPO

The benefits of a configuration without the front heat shield were tested under more critical conditions by considering the case of C_3H_8 CPO, wherein the extent of temperature gradients and the issue of catalyst stability are expected to become even more important due to the higher reaction enthalpy with respect to CH_4 (-228 vs. -36 kJ mol^{-1}). The severity of this reacting system was verified by preliminary C_3H_8 CPO experiments with N_2 diluted feed mixtures; in the case of pre-heated feed streams, extremely high hot spot temperatures (well above 1000°C) and rapid deactivation of the catalyst (evidenced by a progressive increase of the measured temperatures) were observed.

Since the propane CPO is characterized by high surface temperature, the "continuous FHS" configuration was not studied. In fact, even if this configuration ensured the best insulation of the reactor and therefore the best performance, it was also characterized by higher hot-spot in the inlet section. Therefore only the effect of "separated FHS" configuration and "without FHS" configuration were studied.

6.3.1 EFFECT OF THE CONFIGURATION

Initially, the effect of the two configurations was studied at different concentrations of propane, with preheating and under autothermal condition. The system was tested with these operating conditions:

- total flow rate of 10 Nl min^{-1};
- mixture propane/air at O_2/C ratio of 0.56;
- propane concentration 3.33-11.11% for the tests in autothermal, while 3.33-9.09% in the case of preheating.

The gas temperature profiles in the case of preheating were measured with a sliding thermocouple and they are reported in Figure 6.11.

With both configurations, upon increasing the concentration of propane, the temperature profiles shifted at higher values because the increase of the moles of propane caused a larger heat release by the reaction. Besides, while at low concentration of propane (3.33%) there was no difference between the behaviour of the two configurations, when increasing the propane concentration, the "without FHS" configuration was characterized by a lower temperature profile. This effect became more important at higher propane concentration. In fact, in the case of a propane concentration of 6.66%, the difference of temperature between the two profiles was about of 40 °C, while at a propane concentration of 9.09% the difference was about of 90 °C. This behaviour was due to the heat dissipated by radiation, which became more important when the temperatures were higher.

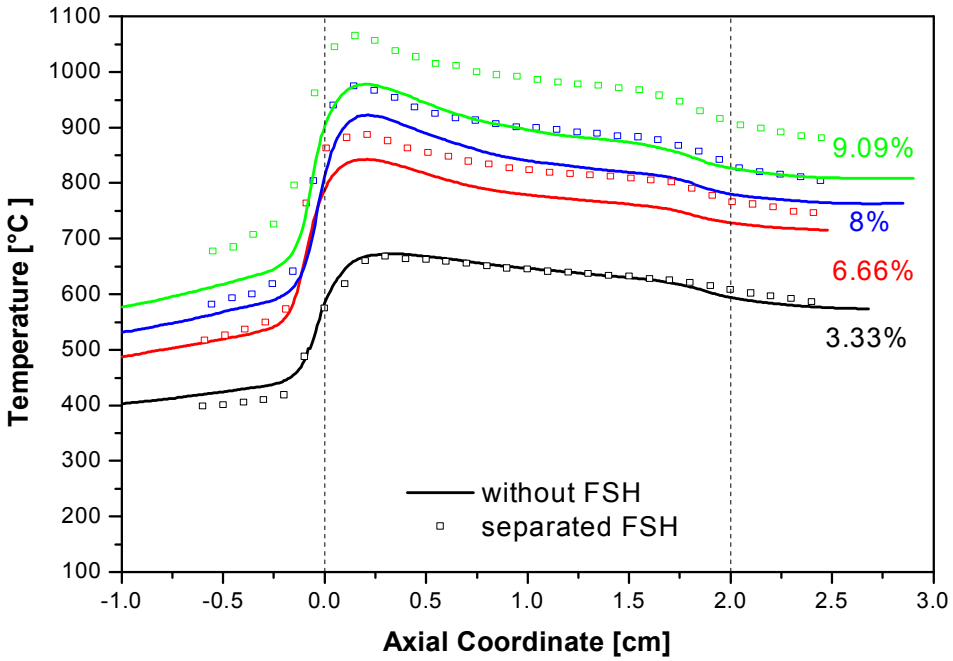

Figure 6.11: Temperature profiles measured with thermocouple at different propane concentrations (3.33, 6.06, 8 and 9.09%). Operating conditions: preheating, C_3H8/Air mixture, O_2/C 0.56, 10 Nl min^{-1} flow rate, atmospheric pressure.

The same tests were also carried out under autothermal conditions. The temperature profiles measured with the sliding thermocouples are showed in Figure 6.12.

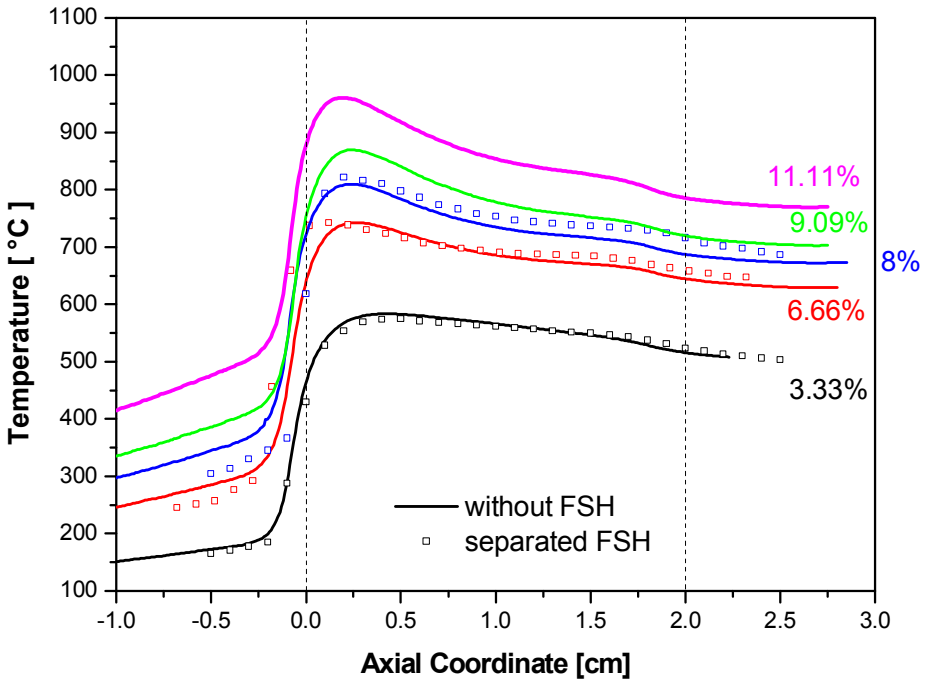

Figure 6.12: Temperature profiles measured with thermocouple at different propane concentrations (3.33, 6.06, 8 and 9.09%). Operating conditions: C_3H8/Air mixture, O_2/C 0.56, autothermal conditions, 10 Nl min^{-1} flow rate, atmospheric pressure.

Under autothermal conditions the two configurations had the same thermal behaviour for propane concentrations of 3.33 and 6.66%, while the temperature difference between the two profiles was minimal in the case of a propane concentration of 8%, where the "without FHS" had a temperature lower of about 10 °C.

Overall, under autothermal conditions the profiles were always characterized by lower temperatures than the profiles with preheating, as the reactants were fed at room temperature. Therefore, under these conditions, it was possible to investigate the thermal behaviour of a non dilute propane/air feed mixture without deactivating the catalyst. Under stoichiometric conditions (11.11%) the temperatures were indeed below 1000 °C.

6.3.2 UNDILUTED TESTS

In order to investigate the thermal behaviour of a undiluted propane/air feed mixture, the autothermal operation turned out to be the experimental methodology of practical interest. In fact, the tests under authermal conditions show lower temperatures than the tests with preheating at the same operating conditions. As shown in Figure 6.13, which plots the calculated surface and gas-phase temperature profiles for an ideal adiabatic reactor with continuous FHS, the shape of the simulated curves (a sharp hot spot, followed by a flattening of the profiles) was the same as in the case of methane, but shifted towards much higher temperatures. The adiabatic simulation indicated that a surface temperature peak of about 1100°C should be expected on the catalyst surface at the monolith entrance. Such high level of temperature certainly leads the catalyst to deactivation and the reactor to unstable operation.

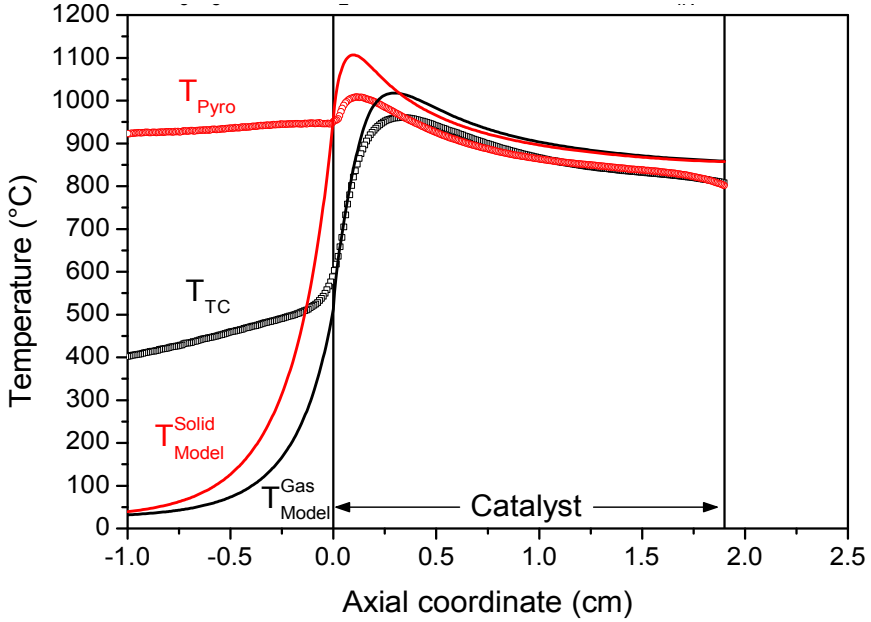

Figure 6.15: Temperature profiles for propane CPO. Comparison between model simulation for the configuration with continuous FHS (solid line) and experimental data for the configuration without FHS (symbols). Operating conditions: mixture C_3H8/Air, O_2/C 0.56, autothermal conditions, flow rate 10 Nl min^{-1}, atmospheric pressure.

Concerning the expected reactor performances (Table 6.2), C_3H_8 conversion and syngas selectivity were estimated to be slightly below to thermodynamic equilibrium values.

	χ C_3H_8 [%]	χ O_2 [%]	σ H_2 [%]	σ CO [%]	σ CH_4 [%]	T_{OUT} [°C]	α
Model - Continuous FHS	98.8	100	91.9	89.1	0.77	858	1.00
Experimental - Without FHS	95.4	99.4	92	91.6	1.28	810	0.90
Equilibrium	100	100	93.7	93.9	0.45	823	1.00

Table 6.2: C_3H_8 CPO, O_2/C = 0.56, 10 Nl min^{-1}, autothermal conditions. Comparison between experimental, calculated and thermodynamic outlet performances.

Notably, a small amount of CH_4 (higher than the equilibrium value) was observed. As previously reported [], this is in line with a combined formation via gas-phase craking reactions and heterogeneous methanation. In general, this experiment was extremely instructive about the possible exploitation of a dissipative reactor configuration to control the inlet temperature rise even with heavier fuels than methane.

6.4 CONCLUSIONS

Rh-coated catalysts for the CPO of hydrocarbons suffer severely from the high reaction temperatures which typically establish at the entrance of short contact time reactors. Sintering of the metal particles in the “oxidation zone” has been clearly documented by means of TEM analysis by Ding et al [63]. The experimental investigation herein presented, based on the detailed measurement of in-situ surface and gas-phase temperature profiles by state of the art tools, shows that the adoption of reactor configurations wherein the radiation from the glowing front face of the monolith is partially lost can greatly help to moderate the temperatures of the hot entry region; this occurs at the expense of a small loss of fuel conversion and selectivity to syngas.

The identification of design strategies able to minimize the hot-spot temperatures is of crucial importance for treating heavier fuels than methane. In this case, in fact, optimization strategies based on the enlargement of the honeycomb channels (which proved to be very successful in the case of methane) could be less efficient in the case of C_{2+} fuels, that is in the case wherein not only the oxygen consumption via oxidation but also the fuel consumption via steam reforming are sensitive to mass transfer limitations.

In the present work, we demonstrated that the coupling between catalyst monolith and FHS represents a degree of freedom, available for the reactor engineering. Very promising results were obtained both with methane and with propane by locating the FHS at the same distance off the catalytic monolith. A decrease of over 100°C for the hot spot temperature was obtained, which can in principle greatly enhance the catalyst lifetime and support the stable operation of the reactor.

CONCLUSIONS

The aim of this thesis work was the study of the thermal behaviour of the CH_4-CPO pilot-scale reformer in order to minimize the hot-spot in the inlet section of the reactor, under steady-state conditions. The study was carried out with the application of the spatially sampling technique and by analysing the results with a monodimensional, dynamic and by analysing the result with a the result heterogeneous model of the reactor. The adoption of the in situ sampling technique has been crucial to completely characterize the performance of the catalytic honeycomb monoliths with enhanced thermal behaviour. Before the effects of the outer capillary diameter and of the location of the sampling probe were investigated for spatially resolved sampling technique. This experimental analysis confirmed that:

- the capillary with lower outer diameter has to be used, so that the fluid dynamics is minimally perturbed;
- sampling from the cold side of the reactor is need to prevent homogeneous reactions in the capillary .

Besides, this technique allowed to verify that the reactor is almost radially isothermal. Indeed, it was observed that only the peripheric channels were characterized by lower temperature, due to the dispersion of heat toward the reactor wall.

After this preliminary study, the technique was applied for the measurement of the axial temperature and composition profiles in the case of a standard honeycomb catalytic monolith. The following observation can be done with respect to the profiles:

- a high hot-spot is present in the inlet section, while downstream the temperature profiles are flat in line with the reaching of the thermodynamic equilibrium was reached;
- in the inlet zone, the surface temperature is much higher than gas phase;
- the consumption of oxygen is completely consumed in few millimeters;
- the oxygen is kinetically controlled by external-mass transfer. Its concentration on the surface of the catalyst is zero;
- the consumption of methane is kinetically controlled by surface chemistry;
- syngas is produced also in presence of oxygen;
- at high flow rate the hot-spot can overcome reach temperature of 1000°C causing the deactivation of the catalyst.

From the analysis of the temperature and of the composition profiles two strategies to minimize the hot-spot were proposed. The first strategy is based on catalyst design, channel opening and catalyst load. First, the single effect of the load was investigated through the spatially resolved sampling technique: results showed that at high catalyst load the rate of methane consumption is high, favouring also, at the entrance of the catalyst, the reforming reaction. In this way there is a balance between the heat released by exothermic oxidation reaction and the heat consumed by reforming reaction. The benefits of high load

catalyst are evident especially at high flow rate. In fact increasing about fours time the catalyst load the hot spot can be reduce of about 200°C and the profiles are smooth. The catalyst load has not effect on the oxygen profile, whose rate of consumption is unvaried. This is coherent, because oxygen is controlled by external mass transfer. In order to modify the rate of oxygen consumption, the channel opening was enlarged. By increasing two times the channel opening of the honeycomb support and three times the load of rhodium, the length of O_2 consumption penetrates within the monolith and so the heat is released over a greater length, thus reducing the hot-spot. By combining two effects, a reduction of oxygen consumption rate and an increase of the rate of consumption of methane occur. These effects cause respectively a lower heat released and favoure the steam reforming reactions.

The second strategy does not modify the rate of reactant consumption, but it acts on the dispersion of the heat in the front section where the hot-spot occurs. Three different configuration are investigated, showing that by favouring the radiative dispersion there is a considerable reduction of the hot-spot with a moderate loss of the performance. Instead, by insulating the system by perturbing the dispersion of the frontal section with a continuous front heat shield, the performance improves as the reactor is perfectly adiabatic and the exit composition reaches the thermodynamic equilibrium. In this case, because of the better insulation, the temperature of the hot-spot increases. Since our aim is to preserve the catalyst from losing activity and becoming thermally instable, the best configuration is that which allows to dissipate the heat of reaction. This study of the optimal reactor configuration becomes even more important in the case of propane where, due to its higher activity, the temperature in the hot-spot can reach 1000 °C even at low flow rate and under diluted conditions.

BIBLIOGRAPHY

[1] Sergio Carrà -*Energia* - Storia della scienza, Encliclopedia Treccani.

[2] http://www.iea.org

[3] A.P.E York, T. Xiao, and M.L.H. Green - *Brief overview of partial oxidation of methane to synthesis gas.* - Topics in Catalysis, 22 (2003).

[4] S.S. Bharadwaj L.D. Schmidt - *Catalytic partial oxidation of natural gas to syngas.* - Fuel Proc. Techn. 42, 109-127 (1995).

[5] *Enciclopedia degli idrocarburi*

[6] K. Aasberg-Petersen, I. Dybkiaer, C.V. Ovensen, NC. Schodt, J. Sehested, S.G. Thomsen - *Natural gas to synthesis gas-catalyst and catalytic process.* - Journal of Natural Gas Science and Engineering, 3 (2011), 423-459.

[7] Jacob A. Mounlijn, Michiel Makkee, Annelies Van Diepen - *Chemical Process Technology.* - Wiley.

[8] A. Beretta, I. Tavazzi, T. Bruno, G. Groppi, V. Dal Santo, L. Sordelli, C. Mondelli - *La produzione di idrogeno di piccola scala.* - La Chimica e l'Industria (2006).

[9] L. Maiocchi - *Ossidazione parziale di metano per la produzione del gas di sintesi su catalizzatori supportati a base di Rh*. - PhD thesis, Politecnico di Milano, 1999.

[10] H. Liander - Trans. Faraday Soc. 25, 462, 1929.

[11] C. Padovani, P. Facchinetti - Giorn. Chem. Ind. Appl. Catal. 15, 429, (1933).

[12] M. Prettre, Ch. Eichner and M. Perrin - Trans Faraday Soc. 42, 335, 1946.

[13] K. Huszar, G. Racz, G. Szekely. *Investigation of the partial catalytic oxidation of methane, conversion rates in a single-grain reactor*. - Acta Chim. Acad. Sci. Hungar, 70: 287-299, 1971.

[14] D.A Hickman, L.D. Schimdt – *Synthesis gas formation by direct oxidation of methane over Pt monoliths* - J. Catal*.,* 138, 267, 1992.

[15] D. A. Hickman, E. A. Haupfear, and L. D. Schmidt - *Synthesis gas formation by direct oxidation of methane over Rh monoliths*. - Catalysis letters 17, 223-237, 1993.
[16] Biorn Christian Enger, Rune Lodeng, Anders Dolmen - *A review of catalytic partial oxidation of methane to synthesis gas with emphasis on reaction mechanism over transition metal catalysts.* - Applied Catalyst A: General, 346, 2008.

[17] D.A. Hickman, L.D. Schmidt - AlChE J. 39 (1993), 1164.

[18] M. Hartmann, T. Kaltschmitt, O. Deutshmann - *Catalytic partial oxidation of higher hydrocarbon fuel components on Rh/Al_2O_3 coated honeycomb monolith* - Catalyst Today, 147S, 2009.

[19] I. Tavazzi, A. Beretta, G. Groppi, A. Donazzi, M. Maestri, E. Tronconi, and P. Forzatti - *Catalytic partial oxidation of CH_4 and C_3H_8: experimental and modelling study of the dynamic and steady-state behaviuor of a pilot-scale reformer* - Studies in Surface Science and Catalysis (167), 2007.

[20] D.A. Hickmann, L.D. Schmidt - Science 259, 1993, 343.

[21] P.D:F: Vernon, M.L.H. Green, A.K. Cheetham, A.T. Ashcroft - Catal. Lett. 6 (1990)181.

[22] Raimund Horn, Nick J. Degenstein, Kenneth A. Williams and Lanny Schmidt - *Spatial and temporal profiles in millisecond partial oxidation process*. - Catalysis letters, 110, 2006.

[23] R. Horn, K.A. William, N.J. Degenstein, L.D. Schmidt.- *Syngas by catalytic partial oxidation of methane: mechanism conclusion from spatially resolved measurement and numerical simulations* - Journal of Catalysis 242(2006), 92-102.

[24] R. Horn, K.A. William, N.J. Degenstein, L.D. Schmidt - *Mechanism of H_2 and CO formation in the catalytic partial oxidation on Rh probed by steady-state spatial profiles and spatially resolved transients* - Chemical Engineering Science 62, 2007, 1298-1307.

[25] R. Horn, K.A. William, N.J. Degenstein, A. Bitsch-Larsen, D. Dalla Nogare, S.A. Tupy, L.D. Schmidt - *Methane catalytic partial oxidation on autothermal Rh and Pt foam catalyst: oxidation and reforming zones, transport effects, and approach to thermodynamic equilibrium.*- Journal of Catalysis 249 (2007), 380-393.

[26] Ivan Tavazzi, Alessandra Beretta, Gianpiero Groppi, Pio Forzatti - *Development of a molecular kinetic scheme for methane partial oxidation over a Rh/α-Al_2O_3 catalyst* - Journal of Catalysis, 241, 2006, 1-13.

[27] J. Rostrup-Nielsen, K. Aaserberg- Handbook of fuel cells. Foundamentals, technologies and applications. – Volume 3: Fuel cell technology and applications: Part 1. Chapter 14 (John Willey & Sons, Ltd)

[28] Konrad Herbst , Gurli Mogensen, Florian Huber, Martin Østberg, Martin Skov Skjøth-Rasmussen – *Challenges in applied oxidation catalysis* – Catalysis Today 157 (2010), 297-302.

[29] K. Heitnes Hofstad, J. H. B. J. Hoebink, A. Holmen, and G. B. Marin - *Partial oxidation of methane to synthesis gas over rhodium catalysts* - Catalysis Today, 40:157–170, 1998.

[30] E. P. J. Mallens, J. H. B. Hoebink, and G. B. Marin - *An investigation on the reaction mechanism for the partial oxidation of methane to synthesis gas over platinum* - Catalysis Letters, 3:291–304, 1995.

[31] K. Heitnes Hofstad, O. A. Rokstad, and A. Holmen - *Partial oxidation of methane over platinum metal gauze*- Catalysis letters, 36:25–30, 1996.

[32] K. Heitnes Hofstad, T. Sperle, O. A. Rokstad, and A. Holmen - *Partial oxidation of methane to synthesis gas over a Pt/10% Rh gauze* - Catalysis letters, 45:97–105, 1997.

[33] L. D. Schmidt and M. Huff. - *Partial oxidation of CH_4 and C_2H_6 over metalcoated monoliths* - Catalysis Today, 21:443–454, 1994.

[34] J. C. Slaa, R. J. Berger, and G. B. Marin. - *Partial oxidation of methane to synthesis gas over Rh/α- Al_2O_3 at high temperatures* - Catalysis Letters, 43:63–70, 1997.

[35] K. Heitnes Hofstad, S. Lindberg, O. A. Rokstad, and A. Holmen - *Catalytic partial oxidation of methane to synthesis gas using monolithic reactors* - Catalysis Today, 21:471–480, 1994.

[36] Ingrid Aartun, Bozena Silberova, Hilde Venvik, Peter Ptfeir, Oliver Gorke, Klaus Schurbert, Anders Holmen – *Hydrogen production from propane in Rh-impregnated metallic microchannel reactors and alumina foams* – Catalysis Today 105 (2005) 469-478.

[37] R. Mark Ormerod – *Solid fuel cells* – Chem. Soc. Rev., 2003, 32, 17-28.

[38] J. Ogrzewalla C. Severin, S. Pischinger - *Compact gasoline fuel processor for passanger vehicle APU.* - Journal of Power Sources, 145:675–682, 2005.

[39] Walter Ray Laster – *Catalytic combustion in large frame industrial gas turbines*

[40] M. Lualdi - *High temperature catalytic processes for energy applications*- Master's thesis, Politecnico di Milano, 2007.

[41] M. Valentini - *Deposizione di strati catalitici a base di γ-Al_2O_3 e ZrO_2 su sopporti ceramici e metallici per applicazioni industriali* - Tesi di Dottorato presso il Politecnico di Milano, 2001.

[42] I.M. Axelsson, L. Lonwedndahl, J. E. Otterstedt – Appl. Cat. 44 (1988), 251.

[43] M. Maestri.- *Modellazione matematica di reattori autotermici a letto fisso perl'ossidazione parziale di metano* - PhD thesis, Politecnico di Milano, 2004.

[44] K. B. Bischoff and G. F. Froment - *Chemical Reactors Analysis and Desig* - Wiley and Sons, 1979.

[45] M. Bizzi, L. Basini, G. Saracco, and V. Specchia - *Modeling a transport phenomena limited reactivity in short contact time catalytic partial oxidation reactors* - Industrial & Engineering Chemistry Research, 42:62 –71, 2002.

[46] A. Frassoldati, T. Faravelli, E. Ranzi - International Journal of Hydrogen Energy 31 (2006) 2310-2328.

[47] O. Deutscmann, LD Schmidt - AlCHE Journal 44 (1998) 2465-2477

[48] R. J. Kee, F. M. Rupley, and J. A. Miller. *The CHEMKIN thermodynamic data base*. Technical report, Sandia National Laboratories, 1987.

[49] D. Manca, G. Buzzi-Ferraris, T. Faravelli, and E. Ranzi - *Numerical problems in the solution of oxidation and combustion problems* - Combustion Theory and Modelling, 5:185–199, 2001.

[50] http://www.chem.polimi.it/homes/gbuzzi.

[51] A. Donazzi, A. Beretta, G. Groppi, and P. Forzatti - *Catalytic partial oxidation of methane over a 4% Rh/α - Al_2O_3 catalyst: Part I: Kinetic study in annular reactor* - Journal of Catalysis, 255:241–258, 2008.

[52] A. Donazzi, A. Beretta, G. Groppi, and P. Forzatti - *Catalytic partial oxidation of methane over a 4% Rh/α- Al_2O_3 catalyst: Part II role of CO_2 reforming* – Journal of Catalysis 255 (2008), 259-268.

[53] M.Maestri, D.G. Vlachos, A. Beretta, G. Groppi, E. Tronconi – AlChE Journal 55 (2009) 993-1008.

[54] A.B. D.G. Vlachos – Journal of Physical Chemistry B 109 (2005), 16819-16835.

[55] Salvatore Belcastro, Davide Pagani – *Ossidazione parziale e steam reforming di propane su catalizzatori Rh/α-Al_2O_3* –Tesi di Laurea specialistica, Politecnico di Milano 2010

[56] S. T. Lee and R. Aris - *On the effects of radiative heat transfer in monoliths* - Chemical Engineering Science, 32:827–837, 1977.

[57] A. Urakawa. A. Baiker – Top Catal. 52 (2009) 1312-1322.

[58] Alessandro Donazzi, Dario Livio, Alessandra Beretta, Gianpiero Groppi, Pio Forzatti - *Surface temperature profiles in CH4 CPO over honeycomb supported Rh catalyst probed with in situ optical pyrometer.* - Applied Catalysis A: General.

[59] Instalments of the course "Misure e strumentazione Industriale".

[60] Susanne Dalley – *Pyrometer handbook*- Mikron Infrared.

[61] D. Dalla Nogare, N.J. Degenstein, R. Horn, P. Canu, L.D. Schmidt – *Modelling spatially resolved profiles of methane partial oxidation on a Rh foam catalyst with detailed chemistry*. – Journal of Catalyst 258 (2008), 131-142.

[62] http://navier.engr.colostate.edu/tools/equil.htm.

[63] S. Ding, Y. Yang, Y, Jin and Y. Cheng - Ind Eng. Chem. Res. 48 (2009) 2878.